FZD-486

CFD models for polydispersed bubbly flows

D. Lucas, E. Krepper

September 2007

Wissenschaftlich-Technische Berichte
FZD-486 2007 · ISSN 1437-322X

WISSENSCHAFTLICH-TECHNISCHE BERICHTE

Forschungszentrum
Dresden Rossendorf

Wissenschaftlich-Technische Berichte
FZD-486
September 2007

D. Lucas, E. Krepper

CFD models for polydispersed bubbly flows

Technical Report

Forschungszentrum Dresden Rossendorf

Technischer Fachbericht

CFD Modelle für polydisperse Blasenströmungen

Technical Report

CFD models for polydispersed bubbly flows

Reaktorsicherheitsforschung-Vorhaben-Nr./
Reactor Safety Research-project No.: 150 1265

Vorhabenstitel: **Aufbau und Durchführung von Experimenten an der Mehrzweck-Thermohydraulikversuchsanlage TOPFLOW für generische Untersuchungen von Zweiphasenströmungen und die Weiterentwicklung und Validierung von CFD-Codes.**

Project Title: **Construction and execution of experiments at the multi-purpose thermal hydraulic test facility TOPFLOW for generic investigations of two-phase flows and the development and validation of CFD codes.**

Autoren / Author(s): **D. Lucas, E. Krepper**

Dienststelle der Autoren /
Performing Organisation: **Forschungszentrum Dresden-Rossendorf e.V., Institut für Sicherheitsforschung**

Berichtsdatum /
Publication Date: **September 2007**

Berichts-Nr. / Report-No.: **FZD-486**

Das diesem Bericht zugrunde liegende Vorhaben wurde mit Mitteln des Bundesministeriums für Wirtschaft und Technologie unter dem Förderkennzeichen 150 1265 gefördert. Die Verantwortung für den Inhalt dieser Veröffentlichung liegt bei den Autoren.

Berichtsblatt

1. ISBN oder ISSN	2. Berichtsart Technischer Fachbericht
3a. Titel des Berichts CFD Modelle für polydisperse Blasenströmungen	
3b. Titel der Publikation	
4a. Autoren des Berichts (Name, Vorname(n)) D. Lucas, E. Krepper	5. Abschlussdatum des Vorhabens 30.09.2006
	6. Veröffentlichungsdatum September 2007
4b. Autoren der Publikation (Name, Vorname(n))	7. Form der Publikation Broschüre
8. Durchführende Institution(en) (Name, Adresse) Forschungszentrum Dresden-Rossendorf e.V. Institut für Sicherheitsforschung Postfach 510119 01314 Dresden	9. Ber.Nr. Durchführende Institution
	10. Förderkennzeichen *) 150 1265
	11a. Seitenzahl Bericht 115
	11b. Seitenzahl Publikation
13. Fördernde Institution (Name, Adresse) Bundesministeriums für Wirtschaft und Technologie (BMWi) 11019 Berlin	12. Literaturangaben 54
	14. Tabellen 2
	15. Abbildungen 75
16. Zusätzliche Angaben	
17. Vorgelegt bei (Titel, Ort, Datum)	

18. Kurzreferat

In vielen für die Reaktorsicherheitsforschung relevanten Untersuchungen werden Mehrphasenströmungen betrachtet, bei denen eine kontinuierliche Flüssigkeitsphase und eine gasförmige Phase als Dampf der Flüssigkeit vorliegen. Je nach dem Volumenanteil der Gasphase bilden sich z.B. in vertikalen Rohren Strömungsformen heraus, die von Blasenströmungen mit geringem oder hohem Gasanteil über Pfropfenströmungen, aufgewühlt turbulenten Strömungen, Ringströmungen bis hin zu Tropfenströmungen variieren können. In den Bereichen der Blasen- und Pfropfenströmungen gibt es ein breites Spektrum von Blasengrößen. Während Blasenströmungen bei geringem Gasgehalt meist monodispers sind, führt eine Erhöhung des Gasanteils auf Grund von Blasenkoaleszenz und –zerfall zu breiteren Blasengrößenverteilungen. Zusätzlich zur Widerstandskraft, die der Relativbewegung der Blase zur Flüssigkeit entgegenwirkt, müssen laterale Kräfte berücksichtigt werden. Eine dieser Kräfte, die Liftkraft wechselt ihr Vorzeichen mit zunehmender Blasengröße. Das führt zu einer Separation großer und kleiner Blasen, die wiederum starken Einfluss auf die Entwicklung der Strömung hat und z.B. einen Übergang zu einer Pfropfenströmung bewirken kann. Die Modellierung muss all diese Phänomene berücksichtigen. Ein Mehrblasenklassen-Testsolver wurde zur Untersuchung der Effekte und zum Test unterschiedlicher Modellansätze entwickelt. Basierend auf den Ergebnissen dieser Untersuchungen wurde ein Konzept für ein Mehrblasenklassenmodell, das Inhomogene MUSIG Modell vorgeschlagen und schließlich in den CFD Code CFX implementiert. In diesem Modell erfolgt eine Unterteilung der dispersen Phase in N Geschwindigkeitsgruppen (Phasen). Jede dieser Gruppen kann wiederum in Mj Blasenklassen unterteilt werden. Durch geeignete Modelle werden Übergänge zwischen diesen Gruppen durch Blasenkoaleszenz und –zerfall modelliert. Das inhomogene MUSIG-Modell wurde an Hand von TOPFLOW-Daten validiert.

19. Schlagwörter
Blasenströmung, CFD, Blasenkräfte, Koaleszenz, Zerfall, Rohrströmung

20. Verlag	21. Preis

Document Control Sheet

1. ISBN or ISSN	2. Type of Report Technical Report
3a. Report Title CFD models for polydispersed bubbly flows	
3b. Title of Publication	
4a. Author(s) of the Report (Family Name, First Name(s)) D. Lucas, E. Krepper	5. End of Project 30.09.2006
	6. Publication Date September 2007
4b. Author(s) of the Publication (Family Name, First Name(s))	7. Form of Publication Booklet
8. Performing Organisation(s) (Name, Address) Forschungszentrum Dresden-Rossendorf e.V. Institut für Sicherheitsforschung Postfach 510119 01314 Dresden	9. Originator's Report No. 10. Reference No.*) 150 1265 11a. No. of Pages Report 115 11b. No. of Pages Publication
13. Sponsoring Agency (Name, Address) Bundesministeriums für Wirtschaft und Technologie (BMWi) 11019 Berlin	12. No. of References 54 14. No. of Tables 2 15. No. of Figures 15
16. Supplementary Notes	
17. Presented at (Title, Place, Date)	

18. Abstract

Many flow regimes in Nuclear Reactor Safety Research are characterized by multiphase flows, with one phase being a continuous liquid and the other phase consisting of gas or vapour of the liquid phase. In dependence on the void fraction of the gaseous phase the flow regimes e.g. in vertical pipes are varying from bubbly flows with low and higher volume fraction of bubbles to slug flow, churn turbulent flow, annular flow and finally to droplet flow. In the regime of bubbly and slug flow the multiphase flow shows a spectrum of different bubble sizes. While disperse bubbly flows with low gas volume fraction are mostly mono-disperse, an increase of the gas volume fraction leads to a broader bubble size distribution due to breakup and coalescence of bubbles. Bubbles of different sizes are subject to lateral migration due to forces acting in lateral direction different from the main drag force direction. The bubble lift force was found to change the sign dependent on the bubble size. Consequently this lateral migration leads to a de-mixing of small and large bubbles and to further coalescence of large bubbles migrating towards the pipe center into even larger Taylor bubbles or slugs. An adequate modeling has to consider all these phenomena. A Multi Bubble Size Class Test Solver has been developed to investigate these effects and test the influence of different model approaches. Basing on the results of these investigations a generalized inhomogeneous Multiple Size Group (MUSIG) Model based on the Eulerian modeling framework has been proposed and was finally implemented into the CFD code CFX. Within this model the dispersed gaseous phase is divided into N inhomogeneous velocity groups (phases) and each of these groups is subdivided into Mj bubble size classes. Bubble breakup and coalescence processes between all bubble size classes Mj are taken into account by appropriate models. The inhomogeneous MUSIG model has been validated against experimental data from the TOPFLOW test facility.

19. Keywords

Bubbly Flow, CFD, Bubble Forces, Coalescence, Breakup, Pipe Flow

20. Publisher	21. Price

This report is part of a series, which comprise following reports:

- Construction and execution of experiments at the multi-purpose thermal hydraulic test facility TOPFLOW for generic investigations of two-phase flows and the development and validation of CFD codes (Final project report), FZD-481,
- Experiments on upwards gas-liquid flow in vertical pipes, FZD-482,
- Experiments on two-phase flow in a vertical tube with a moveable obstacle, FZD-483,
- Experimental investigation of stratified air/water flows in a horizontal channel, FZD-484,
- Experimental investigation and CFD simulation of slug flow in horizontal channels, FZD-485,
- CFD models for polydispersed bubbly flows, FZD-486,
- Turbulent Dispersion of Bubbles in Poly-dispersed Gas-Liquid Flows in a Vertical Pipe, FZD-487,
- Validation of the Multiple Velocity Multiple Size Group (CFX10.0 N x M MUSIG) Model for Poly-dispersed Multiphase Flows, FZD-487.

All these reports are published as reports of the Forschungszentrum Dresden-Rossendorf.

Dieser Bericht ist Teil einer Serie, die folgende Einzelberichte umfasst:

- Aufbau und Durchführung von Experimenten an der Mehrzweck-Thermohydraulikversuchsanlage TOPFLOW für generische Untersuchungen von Zweiphasenströmungen und die Weiterentwicklung und Validierung von CFD-Codes (Abschlussbericht), FZD-480,
- Experimente zu aufwärtsgerichteten Gas-Flüssig Strömungen in vertikalen Rohren, FZD-482,
- Experimente zur Zweiphasenströmung in einem vertikalen Rohr mit verschiebbarem Hindernis, FZD-483,
- Experimentelle Untersuchung von geschichteten Luft/Wasser Strömungen in einem horizontalen Kanal, FZD-484,
- Experimentelle Untersuchung und CFD-Simulation von Schwallströmung in horizontalen Kanälen, FZD-485,
- CFD Modelle für polydisperse Blasenströmungen, FZD-486,
- Turbulente Blasendispersion in einer polydispersen Rohrströmung, FZD-487,
- Validierung des N x M MUSIG Modells für polydisperse Mehrphasen-strömungen, FZD-487.

Alle Berichte sind als Berichte des Forschungszentrums Dresden-Rossendorf veröffentlicht.

Contents

1. Introduction

CFD codes are frequently used for technical applications in case of single phase flow in complicated three-dimensional geometries. The increasing computer power now in principle allows the use of CFD codes for two-phase flows, but there are still some efforts needed to develop suitable constitutive models reflecting the interaction between the gaseous and the liquid phases. In case of adiabatic flows this especially concerns the momentum transfer. For the special case of bubbly flow momentum transfer is usually expressed as forces acting on the bubbles. The situation is very complex because these forces not only depend on the local flow structure (e.g. on the local liquid mean velocity, its gradient and local turbulence parameter), but also may strongly depend on the structure of the interface, e.g. on bubble sizes. Numerical (Ervin and Tryggvason, 1997) and experimental (Tomiyama et al., 1995) investigations showed, that even the sign of the net lateral lift force changes with the bubble size. That means, a more detailed modelling is necessary, than this is done by the wide-spread assumption of mono-disperse bubble flow. The introduction of an additional equation for the bubble density or similar parameter like equivalent bubble diameter or interfacial area is not sufficient to simulate flows with an average gas volume fraction of more than 2-3 %, when in general a broad spectrum of bubble size occur. Instead a number of bubble classes has to be considered. The transition between these bubble classes is determined by bubble coalescence and breakup. While some models for the bubble forces seem to be applicable to a wide range of flow parameter, the transferability of available models for bubble coalescence and breakup is limited. The effects, which are important for adiabatic bubbly flows are presented in chapter 2 of this report.

Gas-liquid flow in vertical pipes is a very good object for studying the corresponding phenomena. Here, the bubbles move under clear boundary conditions, resulting in a shear field of constant and well-known structure where the bubbles reside for a comparatively long time. This allows studying the lateral motion of the bubbles in a shear flow as well as bubble coalescence and breakup. The radial distribution of bubbles strongly depends on their diameter. Caused by the above mentioned lift force in a vertical co-current upflow smaller bubbles tend to move towards the wall, while large bubbles are preferably found in the centre.

A detailed experimental data base for vertical pipe flow, obtained at the MTLoop (Prasser et al., 2003a) and TOPFLOW (Technical Report, part “Experiments on upwards gas-liquid flow in vertical pipes”) facilities using the advanced wire-mesh sensor technology, allows the validation of such constitutive models, especially models concerning the lateral bubble forces and bubble coalescence and breakup. The measurements were done for pipes with an inner diameter of 51.2 mm and 195 mm. Details can be found in the above mentioned reports.

In a first step the data were used to validate the different models for the so called non-drag forces acting perpendicular to the main flow direction. Several models for lift, wall and turbulent dispersion force are included in the CFX code starting from version 5.7. Since 3D calculations are very time consuming, a one-dimensional test solver, which resolves the parameter in radial direction and which was first introduced by Lucas et al. (2001a) was used for the validation of the models over wide range of combinations of superficial velocities. The application of this so-called

Multi Bubble Size Class Test Solver easily enables the test of the bubble force models and of the model parameters before they are implemented in a calculation time consuming 3D CFD code. The Multi Bubble Size Class Test Solver is able to consider a large number of bubble classes. This allows to check the number of bubble classes required. Furthermore, the equalizing effect of the spatial extension of large bubbles on the gas fraction distribution can be accounted for. The test solver was then extended to simulate the evolution of the flow along the pipe. This also includes some first simulations on bubbly flow with condensation. Details on the Multi Bubble Size Class Test Solver and its application for the analyses of experimental data can be found in chapter 3 of this report.

Basing on the results of the investigations done using the Multi Bubble Size Class Test Solver a concept for the extension of the MUSIG-model implemented in the CFX-code was developed and finally implemented by the code developer into code versions following CFX-10. The concept of the so-called inhomogeneous N * M MUSIG model is presended in chapter 4 of this report, while chapters 5 to 7 discuss the validation of this model, which is strongly connected with the models for bubble forces and bubble coalescence and breakup. Different flow situations are considered starting with flows with lower gas fraction, which allow a mono-dispersed approach (chapter 5), continuing with higher gas fraction flows (chapter 6) and finally also some first simulations on a real 3D flow configuration – the flow around an half-moon shaped obstacle introduced in the DN 200 pipe (chapter 7).

2. Bubbly flows

2.1 Bubble forces

As a result of the averaging process, which done to obtain the two-fluid model, closure laws are needed to reflect the mass, momentum and heat transfers between the phases. In the special case of bubbly flow the momentum transfer between the liquid and the bubbles is usually modelled by so-called bubble forces. Depending on the averaging procedure and the flow situation considered, different models can be found in literature. In real two-phase flows there is always a superposition of these forces, i.e. only the action of the resulting total force can be observed. But of course the relevance of the single forces differs in dependence on the flow situation. That makes it possible to validate the single forces using data e.g. for time and space dependent gas fraction distributions in bubbly flows.

The most important forces acting on a bubble are the drag, virtual mass, lift, wall and turbulent dispersion force. They are discussed in more detail below. The most important parameter, on which these forces depend are Reynolds number, Eötvös number and Morton number (see Bhaga and Weber, 1981):

$$\mathrm{Re} = \frac{\rho_l w_{rel} d_b}{\mu_l} \tag{2.1}$$

$$Eo = \frac{g(\rho_l - \rho_g) d_b^2}{\sigma} \tag{2.2}$$

$$Mo = \frac{g\mu_l^4(\rho_l - \rho_g)}{\rho_l \sigma^3} \tag{2.3}$$

2.1.1 Drag force

The drag force reflects the resistance caused by the bubble relative motion to the surrounding liquid. The density of the drag force, which is used for the two-fluid formualation is usually calculated according to

$$\vec{F}_D = \frac{3}{4 d_b} C_D \rho_l \alpha \left|\vec{w}_g - \vec{w}_l\right| (\vec{w}_g - \vec{w}_l) \,. \tag{2.4}$$

Many correlations can be found in Literature for drag force coefficient. In the investigations present in this report the correlations by Schiller-Naumann, Grace, and Tomiyama are used.

The drag coefficient according to Schiller-Naumann (1933) is calculated by

$$C_D = \max\left(\frac{24}{\mathrm{Re}}\left(1 + 0.15\,\mathrm{Re}^{0.687}\right), 0.44\right) \tag{2.5}$$

Grace (1976) related the drag coefficient to the terminal bubble rising velocity V_{term} in a stagnant fluid:

$$C_D = \frac{4}{3}\left(\frac{\rho_l - \rho_g}{\rho_l}\right)\frac{d_b g}{V_{term}^2} \tag{2.6}$$

Tomiyama (1998) used the Schiller-Naumann correlation combined with an Eötvös number dependent term:

$$C_D = \max\left(\frac{24}{\mathrm{Re}}(1+0.15\,\mathrm{Re}^{0.687}), \frac{8}{3}\frac{Eo}{Eo+4}\right) \tag{2.7}$$

For the special case of vertical pipe flow Tomiyama (1998) introduced a modification for large bubbles comparable to the pipe diameter. If the equivalent bubble diameter is larger than $d_{CD,max}$ = 0.63 * D, C_D is calculated according equations (2.1), (2.2) and (2.7), but using a bubble diameter equal to $d_{CD,max}$ instead of d_b. In addition the influence of the pipe walls is considered by the multiplication of C_D with a function ϕ, which depends on the ratio between the equivalent bubble diameter d_b and the pipe diameter D:

$$\lambda = d_b / D \qquad \phi = \begin{cases} 1 & for \quad \lambda < 0.125 \\ (1.13\exp(-\lambda))^{-2} & for \quad 0.125 \le \lambda \le 0.63 \\ 2.761 & for \quad \lambda > 0.63 \end{cases}. \tag{2.8}$$

In the Multi Bubble Size Class Test Solver these correlations are used for the calculation of the drag force coefficient.

2.1.2 Virtual mass force

To accelerate a gaseous bubble, the replacement of the corresponding amount of fluid is necessary. This force is given in terms of the relative accelerations of the phases:

$$\vec{F}_{VM} = C_{VM}\rho_l\alpha\left(\frac{d\vec{w}_g}{dt} - \frac{d\vec{w}_l}{dt}\right) \tag{2.9}$$

Here C_{VM} is a shape and particle dependent constant, being 0.5 for individual spherical particles.

Unfortunately this formulation of the virtual mass as a force causes numerical difficulties since equation (2.9) contains the difference of two quite large almost equal values. Another much more stable solvable way is the consideration of the virtual mass in an increased gaseous density at the left side of the momentum equation.

2.1.3 Lift force

The lift force considers the interaction of the bubble with the shear field of the liquid. Related on the unit volume it can be calculated as:

$$\vec{F}_L = -C_L\rho_l\alpha(\vec{w}_g - \vec{w}_l)\times rot(\vec{w}_l)\,. \tag{2.10}$$

The classical lift force, which has a positive coefficient C_L, acts in the direction of decreasing liquid velocity, i.e. in case of co-current upwards pipe flow in the direction towards the pipe wall. Numerical (Ervin and Tryggvason, 1997) and experimental (Tomiyama et al., 1995) investigations showed, that the direction of the lift force

changes its sign, if a substantial deformation of the bubble occur. Tomiyama did investigations on single bubbles and derived the following correlation for the coefficient of the lift force from these experiments:

$$C_L = \begin{cases} \min[0.288\tanh(0.121\,\mathrm{Re}), f(Eo_d)] & Eo_d < 4 \\ f(Eo_d) & for \quad 4 < Eo_d < 10 \\ -0.27 & Eo_d > 10 \end{cases} \qquad (2.11)$$

$$with \quad f(Eo_d) = 0.00105Eo_d^3 - 0.0159Eo_d^2 - 0.0204Eo_d + 0.474$$

This coefficient depends on the modified Eötvös number given by:

$$Eo_d = \frac{g(\rho_l - \rho_g)d_h^2}{\sigma}. \qquad (2.12)$$

Here d_h is the maximum horizontal dimension of the bubble. It is calculated using an empirical correlation for the aspect ratio by Wellek et al. (1966) with the following equation:

$$d_h = d_b \sqrt[3]{1 + 0.163Eo^{0.757}} \qquad (2.13)$$

For the water-air system at normal conditions C_L changes its sign at a bubble diameter of d_b = 5.8 mm. Bubble diameter in this paper always means the equivalent bubble diameter regarding the volume of a sphere V_b:

$$d_b = \sqrt[3]{\frac{6V_b}{\pi}} \qquad (2.14)$$

The findings of Tomiyama on the change of the sign of the lift force were confirmed by our MTLoop and TOPFLOW experiments on vertical pipes for poly-disperse flows.

2.1.4 Wall force

The wall lubrication force is in the case of pipe flow strongly connected with the lift force, because wall effects have a strong influence on the flow. Antal et al. (1991) proposed a wall lubrication force according to:

$$\vec{F}_W = -\frac{\rho_l \alpha}{r_b}\left(C_{W1} - C_{W2}(\frac{r_b}{y})\right)w_{rel}^2 \vec{n}_r \qquad (2.15)$$

with $C_{W1} = -0.104 - 0.06w_{rel}$ and $C_{W2} = 0.147$, r_b is the bubble radius. Tomiyama (1998) modified this approach for the special case of pipe flow according:

$$\vec{F}_W = -C_W \frac{d_{bubb}\alpha}{2}\left(\frac{1}{y^2} - \frac{1}{(D-y)^2}\right)\rho_l w_{rel}^2 \vec{n}_r \qquad (2.16)$$

The coefficient was determined by experiments on single air bubbles in a glycerol solution:

$$C_W = \begin{cases} \exp(-0.933Eo + 0.179) & 1 \le Eo \le 5 \\ 0.007Eo + 0.04 & 5 \le Eo \le 33 \end{cases} \quad for \qquad (2.17)$$

Although the measurements were done for a system with high Morton number the results were extrapolated to the air-water system. Hosokawa et al. (2002) investigated the influence of the Morton number and developed a new correlation for the coefficient:

$$C_w = \max\left\{\frac{7}{\mathrm{Re}^{1.9}}, 0.0217\,Eo\right\} \tag{2.18}$$

Hosokawa et al. (2002) state, that this correlation is also applicable to low Morton number systems, provided that a bubble does not collide with the wall. Indeed no measurements of bubble trajectories in clear water are shown.

First tests of using this correlation together with the correlation for the lift force according to eqs. (2.10) and (2.11) for our pipe flow data, showed, that small bubbles (d_b ~ 2 – 4 mm) are pushed very close to the wall, i.e. most of them were found in the last node in case of the simulations discussed below. This is not realistic as only the dimension of the bubble avoids locations of the centre of the bubble directly at the wall.

For this reason a deformation force was derived during the investigations described in the present report. It considers the force resulting from the energy, which is necessary to deform a spherical bubble. This force acts only if the equivalent bubble radius is larger than the distance between the centre of the bubble and the wall. The model assumes, that a spherical bubble, which approaches to the wall, is deformed into a prolate ellipsoid with the (shorter) horizontal axis equal to the distance between the centre of the bubble and the wall y. The energy needed for the enlargement of the surface is given by:

$$W = \sigma\Delta A = \sigma(A(y) - A(y = r_b)) \tag{2.19}$$

and the corresponding force for a single bubble is:

$$F^b_{deform} = -\frac{dW}{dy} = -\sigma\frac{1}{r_b}\frac{dA(x)}{dx} \tag{2.20}$$

with $x = y/r_b$.

Inserting the equation for the surface of a prolate ellipsoid and considering the density of the force yields:

$$F_{deform} = \frac{3\sigma}{d_b^2}\left\{\frac{1}{1-x^6}\left(3x + \frac{\arcsin\sqrt{1-x^6}}{x^2\sqrt{1-x^6}} - 4\frac{x^4\arcsin\sqrt{1-x^6}}{\sqrt{1-x^6}}\right) - 2x\right\}. \tag{2.21}$$

This force prevents, that the centre of the bubble are unrealistic close to wall. Of course the shape of a bubble close to the wall is strongly affected by the local shear stress in real flows.

Because of the above mentioned strong connection of the lateral lift force and the wall lubrication force in vertical pipe flow the validation is always done for a combination of both forces. To separate the effects of both forces experimental data obtained in a liquid shear field in a large tank, i.e. far away from a wall, should be useful.

2.1.5 Turbulent dispersion force

The turbulent dispersion force is the result of the turbulent fluctuations of liquid velocity. Lahey et al. (1993) derived an equation for the force per unit volume as

$$\vec{F}_{TD} = -C_{TD}\rho_l k_l \operatorname{grad}\alpha \tag{2.22}$$

with C_{TD} = 0.1.

A more generalized non-uniform turbulent dispersion coefficient on basis of homogeneous turbulence was proposed by Lopez de Bertodano (1998). It depends on the Stokes number as follows:

$$C_{TD} = C_\mu^{1/4} \frac{1}{St(1+St)}, \tag{2.23}$$

with $St = \frac{\tau_g}{\tau_l}$ and $\tau_g = \frac{8 r_b}{3 C_D w_{rel}}$, $\tau_l = C_\mu^{3/4} \frac{k}{\varepsilon}$

Gosman et al. (1992) derived a turbulent dispersion force as

$$\vec{F}_{TD} = -\frac{3 C_D \nu_{t,l}}{4 d_b \operatorname{Pr}} \rho_l w_{rel} \operatorname{grad}\alpha \tag{2.24}$$

The turbulent Prandtl number (or Schmidt number) has an order of magnitude of 1 and is given by

$$\operatorname{Pr} = \nu_l^{eff} / \nu_g \tag{2.25}$$

Similar expressions were obtained from Drew (2001), Carrica et al. (1999) and Burns et al. (2004). They base on Favre averaged drag models and the model according to eq. (2.24) is referred in the following as FAD model for this reason. In case of a small Stokes number it provides the same results like the model from Bertodano, eq. (2.23). As shown by Moraga et al. (2003) this turbulent dispersion force formulation correspond to a diffusion term in the mass balance equation with

$$D^* = \nu_l^{eff} / \operatorname{Pr} \tag{2.26}$$

The turbulent dispersion force has an important influence on the radial gas fraction profiles in vertical pipe flow. It determines the sharpness of the wall peak. In case of a negative lift force coefficient the turbulent dispersion force is the only force, which disperses the bubbles out of the pipe centre. As discussed by Lucas et al. (2001) the dispersion force from Lahey (eq. (2.22)) is too low to avoid that the large bubbles collect at the centreline of the pipe. For this reason Lucas et al. (2001) introduced an Eötvös number dependent dispersion force to reproduce the measured radial gas fraction profiles. This additional dispersion force, which was not established on a solid physical basis is not necessary if the model according to eq. (2.24) is used for the dispersion force and if the geometrical dimensions of the bubbles are considered.

2.2 Coalescence and breakup

Bubble coalescence and bubble breakup in general depend on the local bubble densities n as well as on the dissipation rate of the turbulent kinetic energy ε:

Coalescence rate: $$\Gamma_{i,j} = f(d_i, d_j, \varepsilon) * n_i * n_j, \tag{2.27}$$

Breakup frequency: $$\Omega_i = f(d_i, d_j, \varepsilon) * n_i ,$$ (2.28)

where i and j indicate the bubble class.

A number of models for bubble coalescence and breakup can be found in Literature. Most of them start from a microscopic modelling of the coalescence of two single bubbles or the decay of one single bubble respectively. Free parameters of the resulting models are tuned to achieve a good agreement with experimental data. The effects of the local distributions of the bubble densities as well as from local turbulence influence these parameters. For this reason they are non-transferable to other conditions. It is supposed, that the attempts for a one-dimensional modelling of bubble coalescence and bubble breakup using such models, suffer in case of pipe flow from neglecting of the radial profiles of the bubble densities, which depend on the bubble size. Another problem is the weak modelling of two-phase flow turbulence most CFD codes. Often the model by Sato et al. (1981) is applied, which adds a term for bubble induced turbulence to the turbulent viscosity. Doing this an improvement of the calculated velocity fields is achieved, but wrong values are calculated for the turbulent kinetic energy and the dissipation rate of the turbulent kinetic energy, which is an input parameter for coalescence and breakup models. To improve the modelling of bubble coalescence and breakup and to evaluate the suitability of the models available in Literature first the calculation of the above mentioned turbulence parameter has to be improved.

In the CFX code the model by Prince and Blanche (1990) is used for coalescence and the model by Luo and Svendsen (1996) for breakup. In the simulations presented in this report and in the Technical Report “The Multiple Velocity Multiple Size Group (CFX10.0 N*M MUSIG) Model for Poly-dispersed Multiphase Flows” these models are used with tuned coefficients. For the investigations done with the Multi Bubble Class Test Solver simplified equations for the coalescence rate, breakup frequency and daughter size distribution as described in Lucas et al. (2001b) and Prasser et al. (2003a) are used. Also in this case coefficients were tuned to obtain acceptable agreement with experimental results. Further investigations are necessary to improve the modelling of bubble coalescence and breakup.

2.3 Development of the flow along a vertical pipe

Gas-liquid flow in vertical pipes is a very good object for studying the phenomena of two-phase flows. In case of bubbly flows the bubbles move under clear boundary conditions, resulting in a shear field of constant and well-known structure where the bubbles rise for a comparatively long time. This allows studying the lateral motion of the bubbles in a shear flow by comparing gas distributions measured at different heights. The radial distribution of bubbles strongly depends on their diameter. Caused by the action of the lift force for a vertical co-current upflow smaller bubbles tend to move towards the wall, while large bubbles are preferably found in the centre. The change of the sign of the lift force coefficient was initially observed for single bubbles by Tomiyama et al. (1995). In an air-water system at ambient conditions the change of the direction of the lift force in the shear field occurred at a bubble

diameter of about 5 - 6 mm. We could confirm this also for multi-dispersed flow (Prasser et al., 2002).

Detailed experimental investigations of gas-liquid flows in vertical tubes were made in frame of the present project. Using the fast wire-mesh sensors, developed by our institute, bubble size distributions as well as radial profiles of the gas volume fraction, represented by bubbles of different size were measured. The experiments are described in detail in the Technical Report “Experiments on upwards gas-liquid flow in vertical pipes”. The experimental data are the basis for the investigations on the simulation of bubbly flows presented in this report.

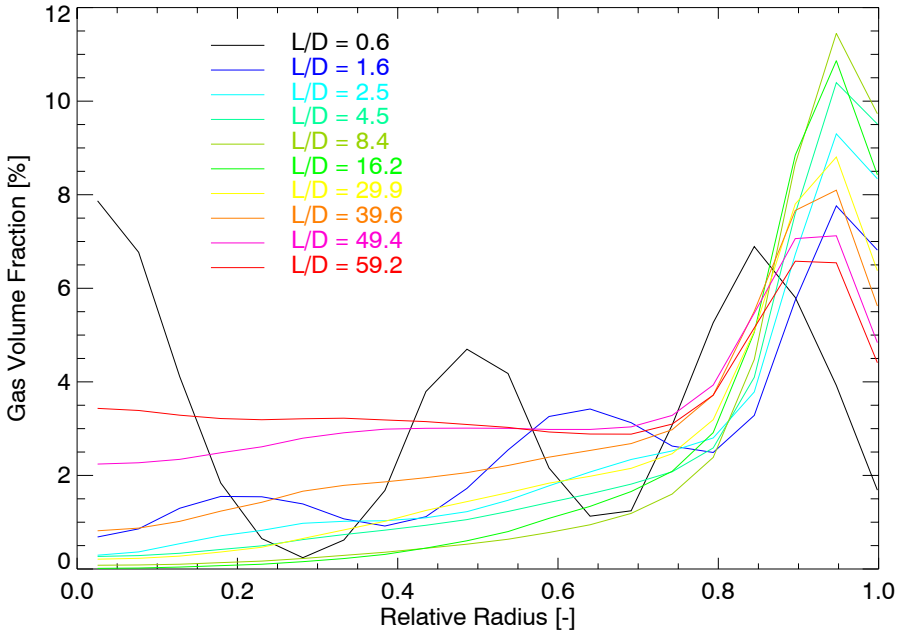

Fig. 2.1 Development of the radial gas fraction profiles along a DN50 pipe (MTLoop experiment), J_l = 1.017 m/s, J_g = 0.0368 m/s.

Fig. 2.1 shows a typical example for the development of the radial gas fraction profiles along a pipe. These experimental data were obtained at the MTLoop facility using a gas injection via 19 capillaries equal distributed over the pipe cross section. There is a fast redistribution of the bubbles in the radial profile. The initial shape of the profile, which is determined by the capillaries of the injection device, vanishes completely at L/D = 2.5. On the other hand there is an increase of bubble sizes because of coalescence. An additional increase of bubble sizes results from the pressure decrease along the pipe. The process of bubble coalescence is much slower compared to the radial redistribution and still continues at the upper end of the pipe. For this reason it is not correct to call the flow at the upper end of the pipe at L/D = 60 “fully developed”, but regarding the radial gas fraction profiles only small changes are observed, caused by the slight changes of the bubble size distribution. This makes possible to assume, that the radial gas fraction profile results from equilibrium of the bubble forces. That means the radial component of the drag force and also the virtual mass force can be neglected. In the analysis presented below for fully developed flow, it is assumed, that radial gas fraction profile at the upper end of the pipe is established for a given bubble size distribution by an equilibrium of the

transversal lift force, the wall lubrication force and the turbulent dispersion force in radial direction, i.e. perpendicular to the flow direction. It has to be considered, that in this case only the relation between the 3 forces mentioned above can be validated. Multiplying all these force with same factor would not change the calculated profiles. To validate the absolute values of these forces the evolution of the flow, i.e. the radial bubble migration has to be considered.

The evolution of the flow along the pipe is determined by a complex interaction between bubble forces, which cause a lateral bubble migration and bubble coalescence and breakup. Also the transition from bubbly to slug flow is influenced by this interaction. As mention above the lift force causes, that small bubbles (diameter < ca. 5.8 mm in case of air-water flow) can be found preferably in the wall region, while larger bubbles are accumulated in the core region. This separation of small and large bubbles clearly influences the development of the flow, since bubble coalescence and breakup depend on the local bubble densities as shown by eqs. (2.27) and (2.28).

On the other hand the dissipation rate of turbulent energy is clearly larger in the near wall region than in the core flow. The consequences for the transition to slug flow can be explained by help of Fig. 2.2. An upward air-water flow is considered. In both considered cases small bubbles (diameter < 5.5 mm) are injected. In the left side of the figure a low superficial gas velocity was assumed. The small bubbles tend to move towards the wall. The local gas fraction in the wall region is larger than the averaged gas fraction, but it is still low. In this case bubble coalescence and breakup are in equilibrium and a stable bubble flow is established.

If the gas superficial velocity is increased (Fig. 2.2, right side), the equilibrium between bubble coalescence and breakup is shifted towards a larger bubble diameter, because the coalescence rate increases with the square of the bubble density, while the breakup rate is only proportional to the bubble density. The bubble breakup rate strongly increases with the bubble diameter.

By a further increase of the gas superficial velocity, more and more large bubbles (diameter > 5.5 mm) are generated. They start to migrate towards the pipe centre. If enough large bubbles are generated by coalescence in the wall region, some of them can reach the core region without breakup. Because of the lower dissipation rate of turbulent energy they can then growth up by further coalescence at much lower breakup rates, typical for the low shear in the centre. This mechanism is the key for the transition from bubble to slug flow. That means, for an appropriate modelling of the transition a number of bubble classes as well as radial gas fraction profiles for each bubble class have to be considered.

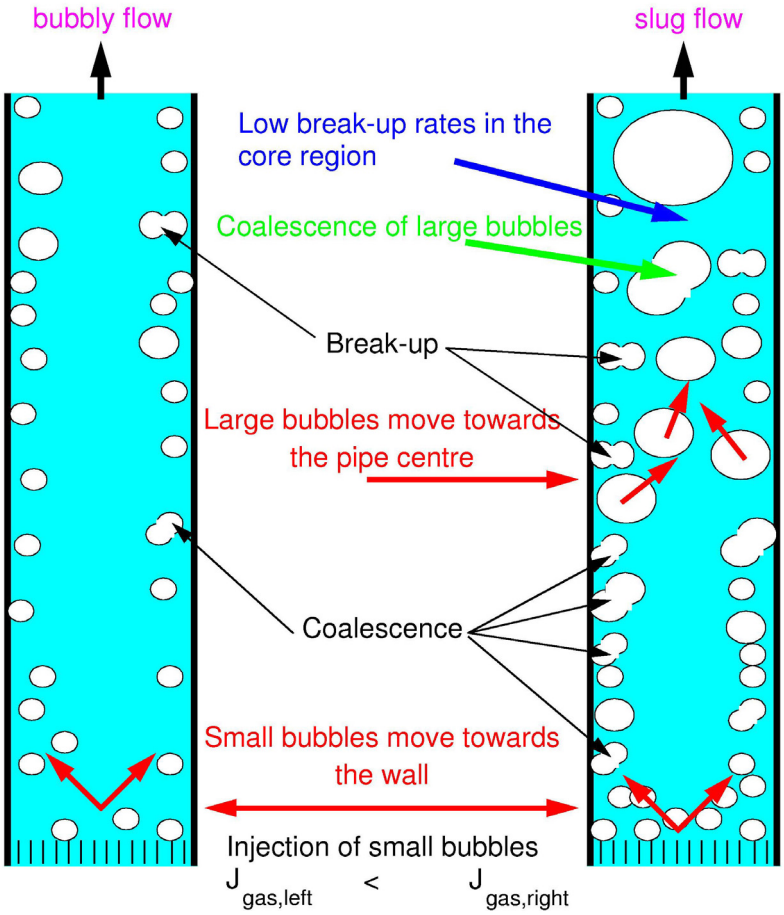

Fig. 2.2 Stable bubble flow (left) and transition to slug flow (right)

3. Multi Bubble Size Class Test Solver

A simplified model for bubbly flow in a vertical pipe was developed during the BMWA project 150 1215 “Strömungskarten und Modelle für transiente Zweiphasen-strömungen” (Prasser et al. 2003a). The aim of this model is to have a efficient tool for testing closure models for bubbly flow, which are suitable for implementation into CFD codes. A description of this first version of the test solver can also be found in Lucas et al. (2001). This model was extended in the reported project to consider all the bubble force models described above, to allow a simulation of the radial bubble migration in case of developing flows. In a special test version of the code also phase transfer according to bubble condensation is included. In the following this models is referred as Multi Bubble Size Class Test Solver. It was extensively used during the reported project for the validation of models for bubble forces by comparison with MTLoop and TOPFLOW data.

3.1 Model description

3.1.1 Basic features of the initial model

The Multi Bubble Size Class Test Solver considers a number of bubble classes (usually ~25-50) and resolves the parameter in radial direction (one-dimensional model). The basic version was introduced by Lucas et al. (2001). This basic version allows calculating the radial gas volume fraction profiles for a given bubble size distribution assuming an equilibrium of the non-drag forces separately for each individual bubble class. To do this the gas volume fraction α is replaced by the volume fraction α_i of the bubble class i. Bubble diameter, Eötvös number, relative velocity and the drag coefficient as well as the lift, wall and turbulent dispersion forces differ for each bubble class. For fully developed flow, the sum of lift, wall and turbulent dispersion force has to be zero:

$$\alpha_i (F_{L,i} + F_{W,i}) + F_{TD,i} + F_{Deform,i} = 0 \,. \tag{3.1}$$

In the result, for a given bubble size distribution from these balance equations radial gas fraction profiles decomposed according to the bubble size, the total radial gas fraction profile (by summing up the afore mentioned profiles) and local bubble size distributions for all radial positions are calculated. The Multi Bubble Size Class Test Solver was extended do consider the different assumptions for the bubble forces discussed above. In general these forces depend on the gradient of the liquid velocity as well as on the turbulent kinetic energy, the dissipation rate of the turbulent kinetic energy and the turbulent viscosity. For this reason models for the calculation of these parameters are required.

The radial profile of the liquid velocity is calculated from a given radial gas distribution using the method described Sato et al. (1981), who introduced an additional term to the turbulent viscosity, which considers bubble induced turbulence. This causes a feedback between the radial gas profile and the radial profile of liquid velocity. The complete model equations as well as a scheme for a numerical solution procedure can be found in Sato et al. (1981). For the calculation of the turbulent kinetic energy the balance equation is used together with the turbulent viscosity hypothesis. A common non-linear differential equation of second order for the steady

state turbulent kinetic energy k of the liquid was derived for the special case of vertical pipe flow (for details see Lucas et al., 2001):

$$\frac{\mu_t}{\sigma_k}\frac{d^2k_l}{dr^2}+\left(\frac{1}{\sigma_k}\frac{d\mu_t}{dr}+\frac{\mu_t}{\sigma_k}\frac{1}{r}\right)\frac{dk_l}{dr}-\frac{C_\mu\rho_l^2}{\mu_t}k_l^2+\mu_t\left(\frac{dw_l}{dr}\right)^2=0 \qquad (3.2)$$

There is a very sensitive feedback between the velocity profile and the gas fraction profile. For this reason they are calculated within an iteration procedure. An under-relaxation is necessary to guarantee the stability of the iteration. Test calculations with an assumed velocity profile according to a 1/m-power law have shown, that this feedback is not negligible.

In case of an air-water flow with bubble sizes below 5.8 mm (i.e. a positive lift force coefficient, eq. (2.11)) the feedback smoothes the radial gas profiles. The bubbles are located preferably at the wall region where they accelerate the liquid. For this reason the liquid velocity near to the wall is increased. This smoothes the velocity profile apart from the wall and reduces the lift force in the core region of the flow, which acts towards the wall. On the contrary, if a considerable fraction of bubbles with a diameter larger than 5.8 mm with negative lift force coefficient is present, a positive feedback between the gas and velocity profiles is established. Those large bubbles accelerate the liquid in the centre. For this reason the velocity gradient in the central region increases. This causes a further increase of the lift force acting towards the pipe centre. Finally, in the calculation the turbulent dispersion is the only force that prevents, that all large bubbles collect at the centreline of the pipe. Some general investigations on the influence of the lift force on the stability of a homogeneous bubbly flow were published by Lucas et al. (2005c) and Lucas et al. (2006).

The balance of balance forces results in volume fraction profiles, valid for the centre of mass of the bubbles, i.e. the entire volume of the bubble is assigned to its central point. A bubble, which is located at the centre of the pipe and which has a dimension in the order of the pipe radius, contributes not only to the gas fraction profile at the location of its centre, but at the entire pipe cross section. For this reason the dimensions of the bubble have to be considered. This is done in the code by assuming an ellipsoidal shape of the bubble according to the deformation given by eq. (2.13). The maximum vertical dimension of the bubble is given by

$$d_v = d_b^3 / d_h^2 \qquad (3.3)$$

and the local vertical dimension of a bubble with the centre located at r_0 is given in cylindrical coordinates by

$$d_{r,\phi} = d_v\sqrt{1-\frac{r^2-2rr_0\cos\phi+r_0^2}{(d_h/2)^2}} \qquad (3.4)$$

According to the radial nodes an integration over the width of the node and over the angle within the limits of a real value of the square root gives the contribution of the bubble to the gas volume fraction of the node. Parts of bubbles that exceed the pipe radius are cut off and the volume of the remaining bubbles is renormalized. By doing this, for each bubble class a matrix is calculated, which assigns the contributions of a

bubble with its centre at the node i to the volume fraction at all the nodes j covered by the dimensions of the bubble.

For bubble classes representing bubbles with a horizontal bubble diameter equal or larger than the diameter of the pipe no radial balance of forces is solved. Instead the bubble centre of mass is always assumed to be located at the centreline of the pipe. According to the procedure presented above the contributions of the bubble to the volume fractions at all radial nodes is given by a fixed matrix. In case of the occurrence of large bubbles and slugs the extension of the bubbles is of crucial importance for the radial profiles, as Fig. 3.1 demonstrates.

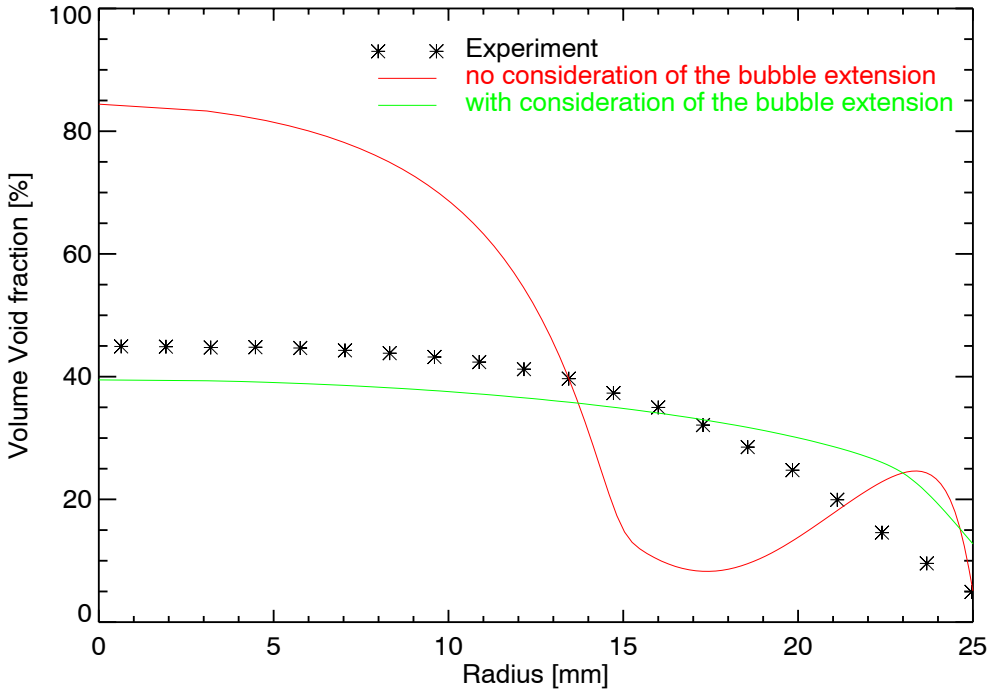

Fig. 3.1 Influence of the extension of the bubbles on the radial gas fraction profile (J_L =1.017 m/s, J_G = 0.534 m/s).

3.1.2 Extension of the Multi Bubble Size Class Test Solver to simulate the evolution of the flow along the pipe

For the simulation of the development of the flow along the pipe besides the radial distributions, in principle the modelled variables have to be resolved also in axial direction. An extension of the Multi Bubble Size Class Test Solver to this second dimension would make the code much more complicate and finally lead to a CFD code giving up the low necessary computational effort of the presented model. To keep the Multi Bubble Size Class Test Solver simple, it does not resolve the variables over the height of the pipe. Instead a vertical bubble velocity, which is equal for all bubble sizes and radial positions is assumed. This allows the approximate evaluation of the flow pattern over the height of the pipe in case of stationary flows by introducing a dependence on time. Because of the assumed uniform bubble velocity, the time corresponds to a height position within the pipe. Starting from an initial bubble size distribution and radial gas volume fraction profile for each time step radial profiles and new bubble size distributions are calculated. The applied uniform vertical bubble velocity was calculated as an average over all bubble classes. The relative

bubble velocities for the single classes result from the equilibrium of the buoyancy force and the drag force. They are added to the averaged liquid velocity. For all the analyses discussed below the liquid superficial velocity was 1 m/s or higher, i.e the liquid velocities are clearly larger compared to the variations of relative velocities for the single bubble classes. Also measurements showed that radial profiles of the gas velocity are flat. For these reasons the variations of vertical bubble velocities are limited and the approximation of an uniform bubble velocity is acceptable for the investigated flow situations.

This concept was introduced by Lucas et al. (2001b). Together with models for bubble coalescence and breakup the development of the flow along a vertical pipe was simulated. It was shown, that this evolution of the flow depends on complex interactions between spatial profiles and bubble size distributions.

The Multi Bubble Size Class Test Solver also considers the pressure drop along the pipe. Gravitation as well as frictional pressure drop is calculated. Starting from a given pressure at the upper end of the pipe the values for pressure and cross section averaged gas volume fraction are calculated in a downwards direction down to the initial height position for the simulation. All gas volume fraction related quantities as gas fraction profiles or bubble size distributions are normalized according to the calculated cross section averaged gas volume fraction for each time step. In addition also the bubble size distributions have to be recalculated to account for the effect of gas expansion along the pipe, which leads to a growth of the bubble diameter. This has to be taken into account by additional transfer terms between bubble size classes, since expanding bubbles may change from one class to another.

The applied assumption of equilibrium of non-drag forces cannot be used to predict the evolution of the gas fraction profiles in axial direction. Therefore, a relaxation procedure was used to simulate the development of the radial profiles as a first approximation. The resulting radial profiles were obtained by a weighted summation of the profile from the previous time step and the new equilibrium profile. This does not reflect the lateral bubble migration in a satisfactory manner. To overcome this deficiency, the Multi Bubble Size Class Test Solver was improved by introducing a complete momentum equation for the lateral bubble migration (Lucas et al., 2007b).

The radial volume fraction profile for the bubble class i is determined by the balance equations for mass and momentum in radial direction. The density of the single phases is assumed to be constant. Within the considered domain the only mass sources S_i for the bubble class results from bubble coalescence and breakup. The mass balance for bubble class i then reads:

$$\frac{\partial \alpha_i}{\partial t} + \frac{1}{r}\frac{\partial}{\partial r}(r u_i \alpha_i) = S_i \tag{3.5}$$

with α_i the volume fraction and u_i the radial bubble velocity of the bubble class i. Under the above mentioned approximations and neglecting the momentum transfer between the bubble classes caused by coalescence and breakup, the momentum balance for the bubble class i in radial direction is obtained as:

$$\alpha_i \left(\rho_g + C_V \rho_l\right)\left(\frac{\partial u_i}{\partial t} + \frac{u_i}{r}\frac{\partial r u_i}{\partial r}\right) = \left(F_{D,i} + F_{L,i} + F_{W,i} + F_{TD,i} + F_{deform,i}\right) \tag{3.6}$$

with the velocity of the bubble class i in radial direction u_i and the coefficient of the virtual mass C_V.

Since these equations are solved separately for each bubble class the index i is omitted for simplicity in the following. The index k marks the radial node. In the numerical scheme used, the values for the volume fraction α are given within the radial nodes, while the gradients of volume fraction and liquid velocity are given at the boundary of the nodes. For a consistent discrete modelling, partial velocities at the boundaries are introduced according to the scheme shown at Fig. 3.2.

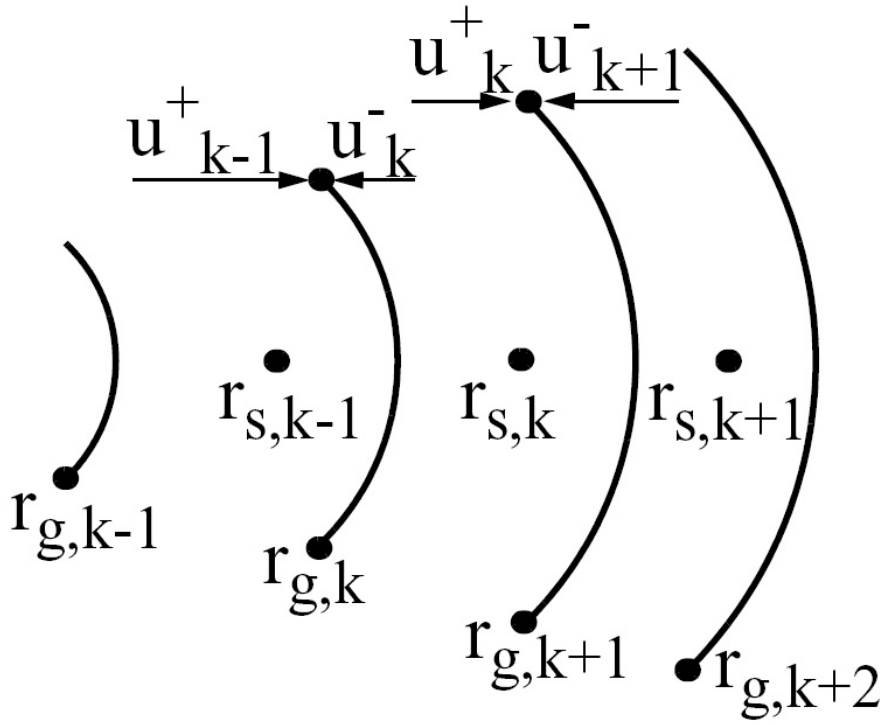

Fig. 3.2 Schema of the applied discretisation method (from Lucas et al., 2007b))

The velocity u^-_k is calculated using the node values of node k and the gradients at the lower node boundary at $r_{g,,k}$, while u^+_k results from the node values of node k and the gradients at the upper node boundary at $r_{g,k+1}$. Furthermore u^-_k is set to zero, if positive values are calculated and u^+_k is set to zero, if negative values are calculated (upwind scheme).

For one time step first the change of the velocities caused by the forces are calculated. Afterwards the gas volumes and the momentum are shifted according to this velocity. It is assumed, that the gas is equally distributed within one node, which forms an annulus in the radial geometry. The shift is done in a way, that the centre of mass of the annulus is shifted according to u * Δt. The centre of mass of an annulus in case of a constant density is calculated by:

$$r_s = \frac{\int_{r0}^{r1} \rho r^2 dr}{\int_{r0}^{r1} \rho r dr} = \frac{2}{3}\frac{r_1^3 - r_0^3}{r_1^2 - r_0^2} \qquad (3.7)$$

with r_0 and r_1 the inner and outer radii of the annulus. A fraction Θ of the gas volume, which has to be shifted from node k to node k+1, is calculated according to:

$$r_s^{new} = r_{s,k} + u_k^+ \Delta t = \frac{2}{3} \frac{(1-\Theta_k^+)(r_{g,k}^3 - r_{g,k-1}^3) + \Theta_k^+ (r_{g,k+1}^3 - r_{g,k}^3)}{(1-\Theta_k^+)(r_{g,k}^2 - r_{g,k-1}^2) + \Theta_k^+ (r_{g,k+1}^2 - r_{g,k}^2)} \tag{3.8}$$

The right hand side of this equation represents the centre of mass, if the shifted fraction is equally distributed within node k+1 and the remaining one equally distributed in node k. In the model all radial nodes have equal volumes, i.e.

$$r_{g,k}^2 - r_{g,k-1}^2 = r_{g,k+1}^2 - r_{g,k}^2 \tag{3.9}$$

for all k.
For this special case applies:

$$\Theta_k^+ = \frac{u_k^+ \Delta t}{r_{s,k+1} - r_{s,k}} \tag{3.10}$$

In analogy for Θ_k^- yields:

$$\Theta_k^- = \frac{u_k^- \Delta t}{r_{s,k} - r_{s,k-1}} \tag{3.11}$$

These fraction of gas volumes are shifted from one node to the other together with their momentum. The source terms in the mass balance resulting from coalescence and breakup are calculated from the corresponding models and added separately to the gas volume fractions for each node and bubble class. Since the momentum transfer caused by bubble coalescence and breakup is neglected, there is no influence on the stored velocity fields.

The transport model was verified for an a-priory given gas peak, which moves with a constant (explicitly assumed) velocity from the pipe wall towards the centre. The velocity was checked against an analytical solution. It was reflected exactly by the numerical model and the numerical diffusion of the peak was not exceeding an acceptable degree.

3.1.3 Extension of the Multi Bubble Size Class Test Solver for condensation

In a next step the Multi Bubble Class Test Solver was extended to consider transient mass and heat transfer between the phases. For large bubbles the dynamics of the phase transfer is determined by the heat fluxes to or from the interface. It is assumed, that the interface itself is on saturation temperature T_s, which is function of the local pressure. Far from the interface the liquid temperature is T_l and the gas temperature T_g.

Neglecting both, the wall heat transfer and pressure changes with time and using the assumption of constant heat capacity (i.e. $(h_l - h_s) \sim c_{p,l} (T_l - T_s)$) the following equation for local changes of the temperature caused by phase transfer can be derived from the energy balances of the liquid phase:

$$\frac{dT_l(r)}{dt} = \frac{d(T_l(r) - T_s)}{dt} = \frac{1}{[1-\alpha(r)]\rho_l} \left[-\frac{\sum_i q_{l,i}^{phases}(r)}{c_{p,l}} + [T_l(r) - T_s] \sum_i \Gamma_i(r) \right] \tag{3.12}$$

$\alpha = \sum_i \alpha_i$ is the gas volume fraction, $q^{phases}_{l,i}$ the volume related heat flux from the liquid phase to interfaces of the bubble class i [W/m^3] and Γ_i the mass transfer rate to the bubble class i [kg/(m^{3}s)]. The last two parameters are calculated according to:

$$q_{l,i}^{phases}(r) = k_{l,i} f_i(r)[T_l(r) - T_s], \qquad \Gamma_i(r) = \frac{q_{l,i}^{phases}(r) + q_{g,i}^{phases}(r)}{h_{gl}} \tag{3.13}$$

with the heat transfer coefficient of the liquid phase $k_{l,i}$, the interfacial area concentration f_i and the evaporation heat h_{gl}. Analogues equations can be obtained for the temperature of each bubble class $T_{g,i}$ and the volume related heat flux from bubble class i to the interface $q^{phase}_{g,i}$. The heat transport along the pipe radius within the liquid is neglected in this first version of the model, i.e. condensation rates that are unequally distributed over the radius cause radial temperature profiles to grow.

For the gas-interfacial heat transfer coefficient from the liquid phase to the bubble class i the correlation given by Hughmark (1967) was applied:

$$k_{l,i} = \begin{cases} \dfrac{\lambda_l}{d_{b,i}}(2 + 0.6\,\mathrm{Re}_i^{0.5}\,\mathrm{Pr}_l^{0.33}) & 0 \le \mathrm{Re}_i \le 776 \\ \dfrac{\lambda_l}{d_{b,i}}(2 + 0.27\,\mathrm{Re}_i^{0.62}\,\mathrm{Pr}_l^{0.33}) & \mathrm{Re}_i > 776 \end{cases} \tag{3.14}$$

Here Pr_l and λ_l are the Prandtl number and the thermal conductivity of the liquid respectively and Re^i is the bubbles Reynolds number of bubble class i:

$$\mathrm{Re}_i = \frac{\rho_l w_{rel,i} d_{b,i}}{\eta_l} \tag{3.15}$$

with the bubble diameter of the bubble class i, $d_{b,i}$, which is defined as volume equivalent diameter of a sphere. The correlation was originally obtained for forced convection around a rigid sphere. It possibly under-predicts the heat transfer for gas liquid flows. For the gaseous phase thermodynamic equilibrium is assumed.

The interfacial area was calculated separately for each bubble class. To do that, an ellipsoidal shape of the bubbles according to the correlation from Wellek (1966) for the relation of horizontal and vertical axis (d_h and d_v) of the ellipsoid was assumed:

$d_{h,i}/d_{v,i} = 1 + 0.163 Eo_i^{0.757}$, with the Eötvös number $Eo_i = \dfrac{g(\rho_l - \rho_g) d_{b,i}^2}{\sigma}$. (3.16)

The interfacial area concentration for the bubble class i (volume fraction α_i) is calculated from the formula for the surface of an oblate ellipsoid:

$$f_i(r) = \frac{3\alpha_i}{d_{b,i}} \left(\frac{d_{h,i}}{d_{v,i}} \right)^{\frac{2}{3}} \left(1 + \frac{1 - e_i}{2e_i} \ln \frac{1 + e_i}{1 - e_i} \right) \quad \text{with} \quad e_i = \sqrt{1 - d_{v,i}/d_{h,i}} \,. \tag{3.17}$$

The extrapolation of the Wellek correlation to very large bubbles is questionable since the bubble shape changes from ellipsoidal to spherical cap, but for the lack of more detailed information on the interfacial area it is used as a first approximation. For illustration: for a bubble with $d_{b,i}$ = 50 mm the interfacial area calculated by the eqs. (3.16) and (3.17) is about 4 times larger compared to the interfacial area of an volume-equivalent sphere.

The mass transfer rate is calculated separately for each bubble class and each radial node using eqs. (3.13) -(3.17). Afterwards the changes of the liquid temperature for each node are calculated according to eq. (3.12). New gas temperatures are obtained separately for each bubble class and node. To realize the mass transfer, the changes of the gas volume fraction are calculated for each bubble class and each radial node:

$$\left.\frac{d\alpha_i(r)}{dt}\right|^{phase\_transfer} = \frac{\Gamma_i(r)}{\rho_g}\rho_{av,rel} \text{, with } \rho_{av,rel} = \frac{(1-\alpha)\rho_l + \alpha\rho_g}{\rho_l}. \tag{3.18}$$

The averaged fluid density related to the liquid density $\rho_{av,rel}$, which occurs as a factor on the right hand side of the equation considers the change of the total volume to which the gas volume is related according to the definition of α.

Beside the decrease of the volume fraction because of the condensation process also the shift in the local bubble size distributions towards small bubble size has to be considered. The change of the bubble volume for bubble class i is given by:

$$\frac{dV_{b,i}(r)}{dt} = \frac{\Gamma_i(r)V_{b,i}(r)}{\rho_g\alpha_i(r)} \tag{3.19}$$

According to these changes in bubble size, source and sink terms are obtained for all the bubble classes in addition to eq. (3.18). There is a shift of the gas volume fraction from group i to group i-1 as demonstrated schematically at Fig. 3.3.

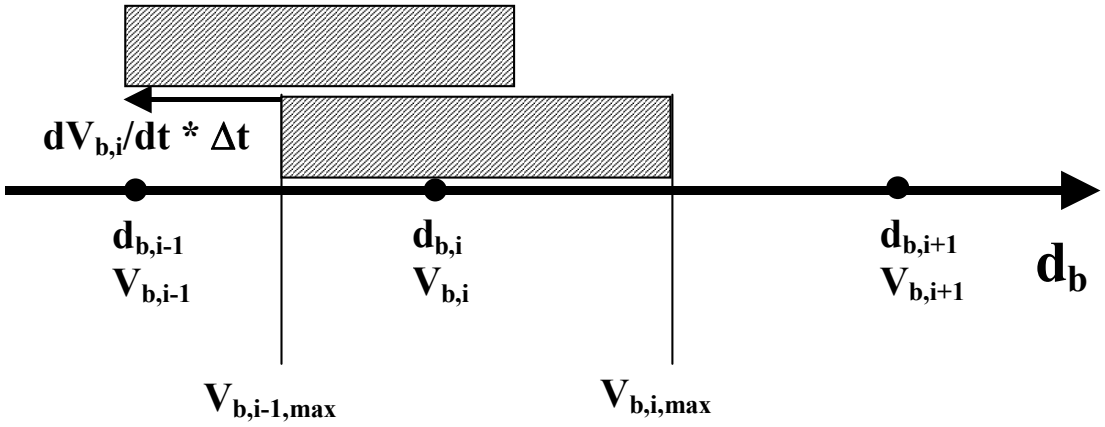

Fig. 3.3 Shift of volume fraction to lower bubble size group caused by the shrinking of the bubbles.

The additional source and sink term are calculated according to

$$\left.\frac{d\alpha_i(r)}{dt}\right|^{bubble\_shrinking} = -S_i(r) + S_{i+1}(r) \quad \text{with}$$
$$S_i = -\frac{dV_{b,i}(r)}{dt}\Big/(V_{b,i,\max} - V_{b,i-1,\max}) = \frac{\Gamma_i(r)V_{b,i}(r)}{\rho_g(V_{b,i,\max} - V_{b,i-1,\max})}. \tag{3.20}$$

Herein $V_{b,i,max}$ is the bubble volume at the upper end of the interval for the bubble size group i. Similar terms for the transfer between the phases were introduced to the model earlier to simulate the change of the bubble sizes due to changes of the local pressure (see Lucas et al. 2005b).

3.2 Comparison with CFX for simplified test cases

Most of the above discussed models for lateral bubble forces were also included in the CFX code (Shi et al., 2004a). This allows a comparison between the results of the radial 1D model with results obtained by CFX for simplified test cases. For the comparisons the code version 5.7 was used. In a first step, presented here, only one bubbles class was considered in CFX and also in the 1D model. To achieve equilibrium of the forces neither bubble coalescence and breakup nor any pressure gradient along the pipe were considered in the CFX calculation. Starting from the inlet, the equilibrium state was obtained after the migration of the bubbles. The criteria, that the equilibrium was reached, is, that no further change of the radial profiles occurred with increasing length of the pipe.

In both calculations the same models for the bubble forces were used (Tomiyama lift and wall eqs. (2.10), (2.11), (2.15) and (2.16) and FAD, eq. (2.24)). The main differences in the modelling are:

- The use of the model from Sato et al. (1981) for the calculation of the profile of the liquid velocity in the 1D model, while this profile results from the conservation equations in CFX.
- The simplified k-ε model as introduced by Lucas et al. (2001a) for the calculation of turbulence parameters in the 1D model, while the SST (shear stress transport) model was used in CFX.

Fig. 3.4 and Fig. 3.5 show, that despite these differences in the modelling the gas volume fraction profiles as well as the profiles of the turbulent kinetic energy are in a good agreement between the two simulations. Also scaling effects are reflected in the same manner, as Fig. 3.6 shows. These comparisons demonstrate, that the 1D model is suitable for the validation of models for the forces acting on the bubbles, which will be used in a CFD code.

3.3 Analyses of the models for bubble forces for fully developed flow

Experimental data obtained at the MTLoop facility (Prasser et al. 2003a) and TOPFLOW facility (see Technical Report “Experiments on upwards gas-liquid flow in vertical pipes”) were used to validate the models for the lift, wall and drag forces, which are discussed in chapter 2. The Multi Bubble Size Class Test Solver (basic version as described in section 3.1.1) was used to calculate radial gas fraction profiles from the measured bubble size distributions. Experimental data for the upper position of the sensor in the pipe were used for the validation of the forces acting perpendicular to the mean flow direction. The calculated radial gas fraction profiles are compared to the experimental results.

Experimental data are available for many combinations of superficial velocity. They base on a general test matrix, which is shown at Fig. 3.7. The tests are referred below according to the numbers given in this matrix.

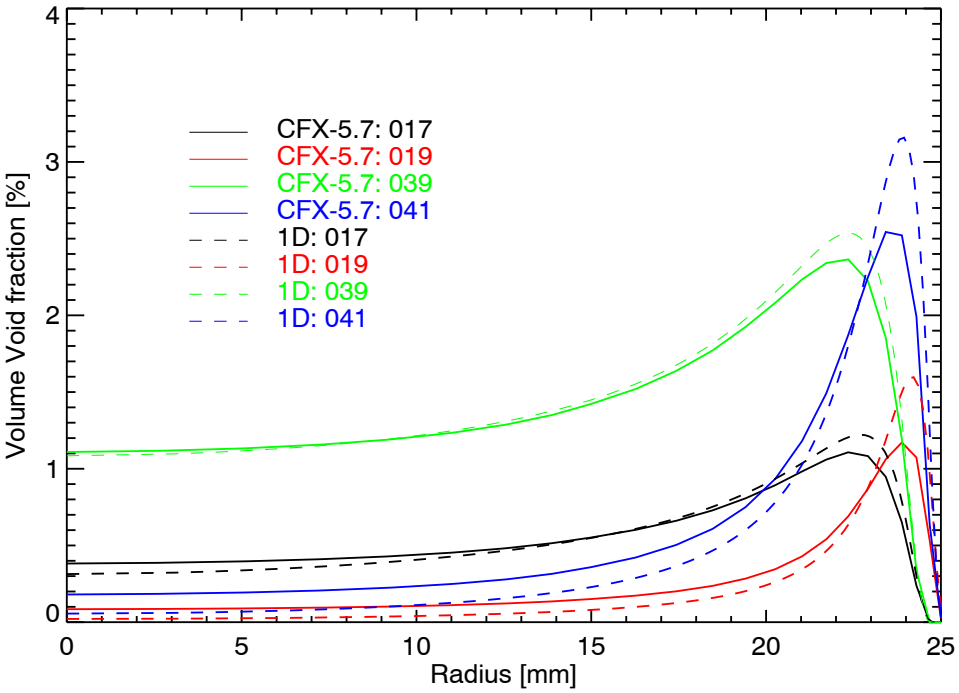

Fig. 3.4 Comparison of radial gas fraction profiles calculated by CFX and the 1D model for 4 different combinations of superficial velocities (017: J_L=0.405 m/s, J_G=0.0040 m/s, 019: J_L=1.017 m/s, J_G=0.0040 m/s, 039: J_L=0.405 m/s, J_G=0.0096 m/s, 041: J_L=1.017 m/s, J_G=0.0096 m/s).

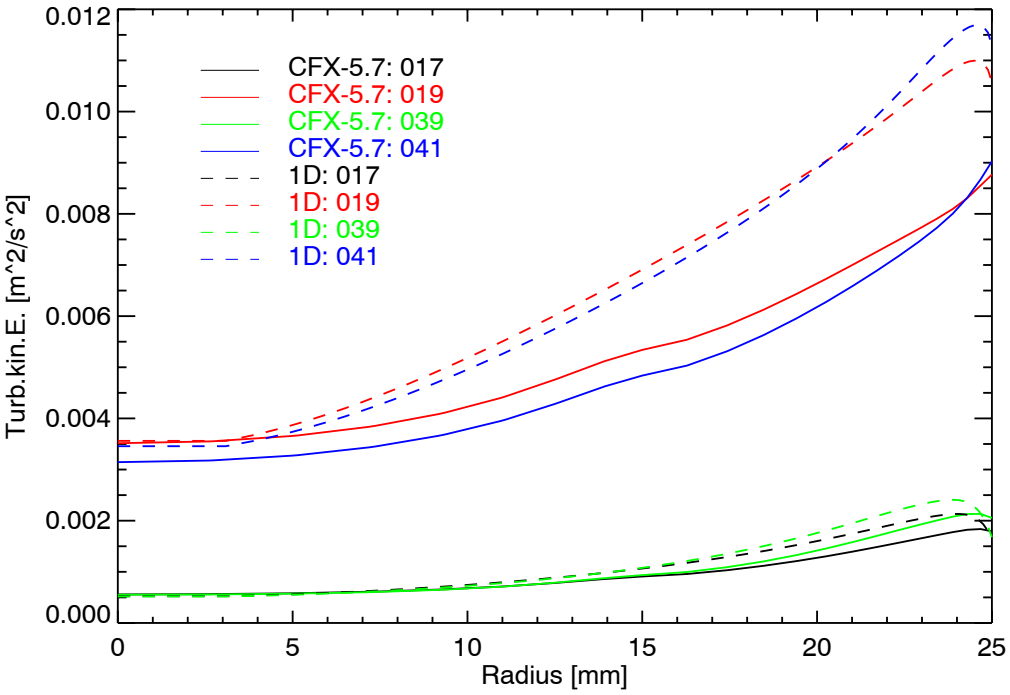

Fig. 3.5 Comparison of the profiles of the turbulent kinetic energy calculated by CFX and the 1D model for 4 different combinations of superficial velocities (values see Fig. 3.4).

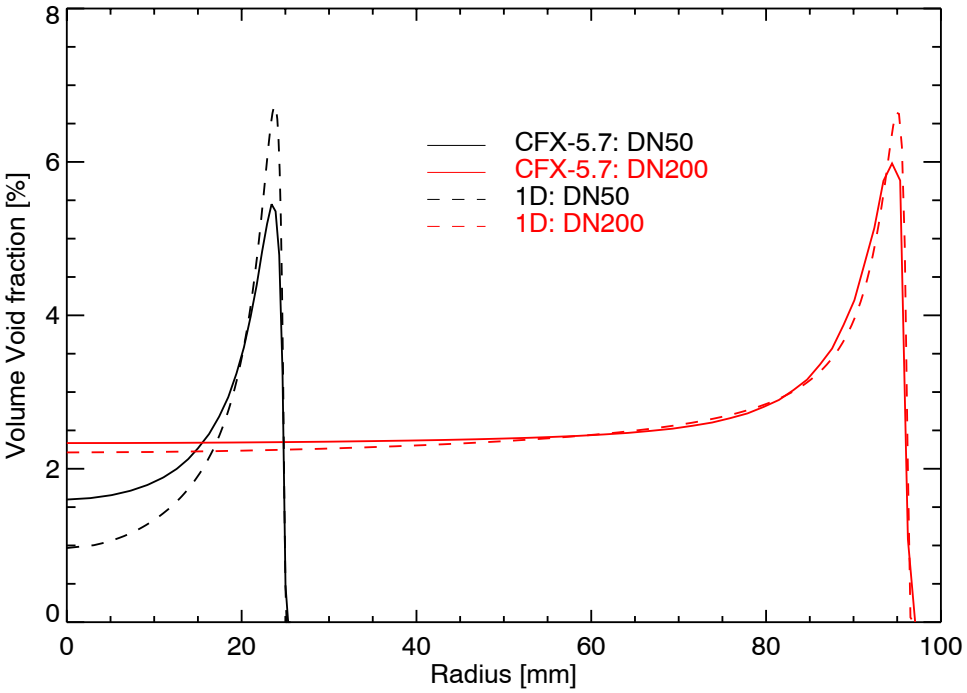

Fig. 3.6 Comparison of radial gas fraction profiles calculated by CFX and the 1D model for the DN50 and the DN200 pipe. J_L=1.017 m/s, J_G=0.0368 m/s.

Liquid Superficial Velocity J_W in m/s	Gas Superficial Velocity J_G in m/s																			
	0,0025	0,0040	0,0062	0,0096	0,0151	0,0235	0,0368	0,0574	0,0898	0,140	0,219	0,342	0,534	0,835	1,305	2,038	3,185	4,975	7,772	12,14
4,047	011	022	033	044	055	066	077	088	099	110	121	132	143	154	165	176	187	198	209	220
2,554	010	021	032	043	054	065	076	087	098	109	120	131	142	153	164	175	186	197	208	219
1,611	009	020	031	042	053	064	075	086	097	108	119	130	141	152	163	174	185	196	207	218
1,017	008	019	030	041	052	063	074	085	096	107	118	129	140	151	162	173	184	195	206	217
0,641	007	018	029	040	051	062	073	084	095	106	117	128	139	150	161	172	183	194	205	216
0,405	006	017	028	039	050	061	072	083	094	105	116	127	138	149	160	171	182	193	204	215
0,255	005	016	027	038	049	060	071	082	093	104	115	126	137	148	159	170	181	192	203	214
0,161	004	015	026	037	048	059	070	081	092	103	114	125	136	147	158	169	180	191	202	213
0,102	003	014	025	036	047	058	069	080	091	102	113	124	135	146	157	168	179	190	201	212
0,0641	002	013	024	035	046	057	068	079	090	101	112	123	134	145	156	167	178	189	200	211
0,0405	001	012	023	034	045	056	067	078	089	100	111	122	133	144	155	166	177	188	199	210

Fig. 3.7 General test matrix for MTLoop and TOPFLOW vertical pipe data

3.3.1 Analyses for the DN50 pipe

In case of the MTLoop facility the inner pipe diameter is equal to 51.2 mm, the position of the wire-mesh sensor is located 3.03 m above the gas injection (L/D = 60). The details of the measurements are presented by Prasser et al. (2003). For the calculations the radius of the pipe was divided into 100 nodes of equal volume. The last node was subdivided in 10 nodes for the calculation of the profile of the radial water velocity according to the recommendations of the Sato-model. The bubble size distribution was represented in the calculations by 35 bubble classes with an increasing width. Variations of the number of nodes and bubble classes showed, that this guarantees the independency of the results on the discretisation.

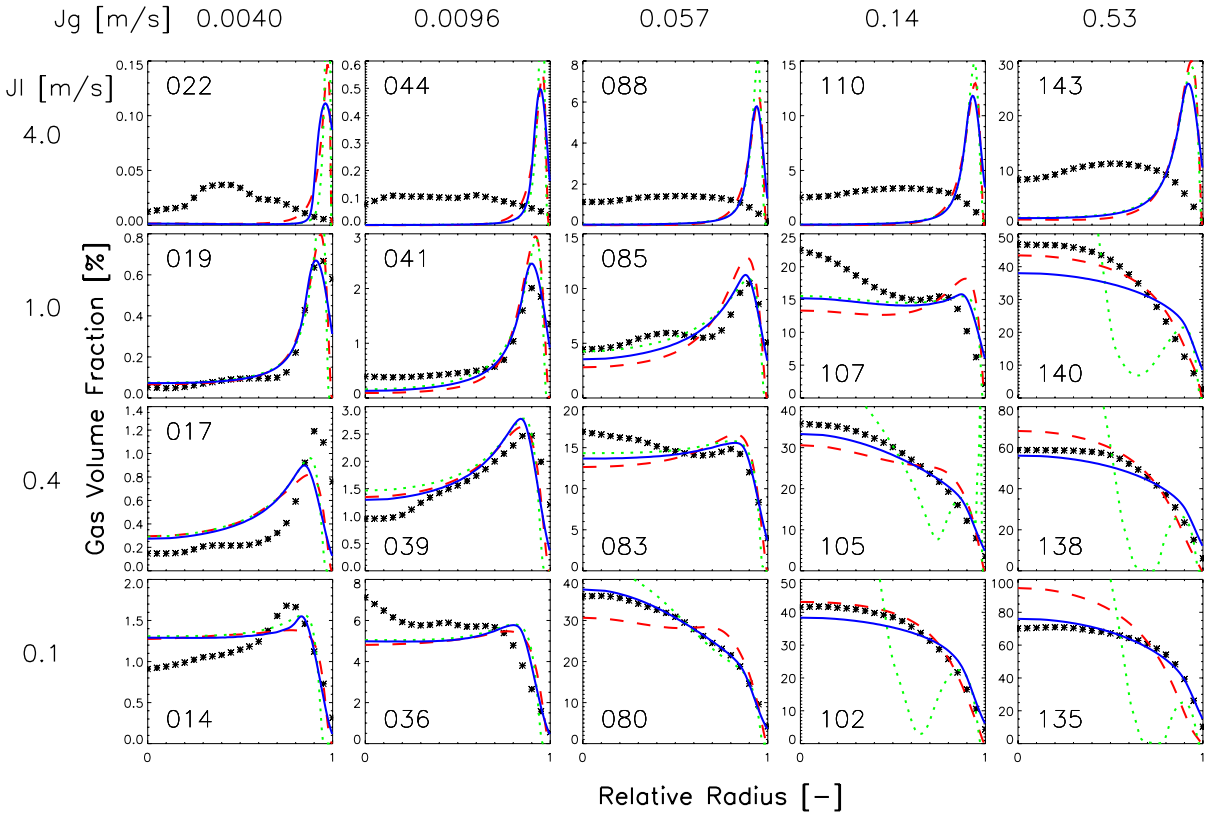

Fig. 3.8 Effect of different dispersion force models: stars - Experiment, red dashed lines - model by Lucas et al. (2001), green dotted lines - FAD model eq. (2.24), blue solid lines - FAD model eq. (2.24) and consideration of bubble dimensions

The comparison was done for all the measured combinations of gas and liquid superficial velocities. Fig. 3.8 shows the comparison of the measured radial gas fraction profiles with those calculated using lift and wall forces from Tomiyama (eqs. (2.10) and (2.11)) and different dispersion forces. The red dahed lines (dispersion force according to eq. (2.22) and Eötvös number dependent dispersion force) accord to the model introduced by Lucas et al. (2001). The additional dispersion force, which increases with the Eötvös number without any limitation provokes the flat profiles for large bubbles and slugs, which occur in the case of low liquid and high gas superficial velocities. Using only the FAD model for the dispersion force, eq. (2.24) for these points radial gas fraction profiles with pronounced peaks in the pipe centre

and at wall occur (green dotted lines). This is due to the non-considered effect of the dimensions of the large bubbles and slugs. By consideration of the bubble dimensions as described in chapter 3.1, these deviations from the measured profiles vanish, i.e. the profiles are mainly determined by the bubble dimensions. In general the agreement between calculated and measured profiles is satisfactory despite for liquid superficial velocity of 4 m/s (finely dispersed bubbly flow). Because of the strong gradient of the liquid velocity the lift force causes a pronounced wall peak in the calculation, while the measurements show an intermediate peak of the radial gas volume fraction.

Fig. 3.9 shows a comparison, which includes a variation of the FAD model for the dispersion force with a constant factor and the dispersion force according to eq. (2.24). There is no improvement of the agreement by decreasing or increasing the dispersion force eq. (2.24) by an additional coefficient. This is also true for the dispersion force proposed by Bertodano, eqs. (2.22) and (2.23). Again it should be considered, that the profiles for cases with high gas volume fractions (right lower corner of the matrix) is mainly determined by the dimensions of large bubbles and slugs.

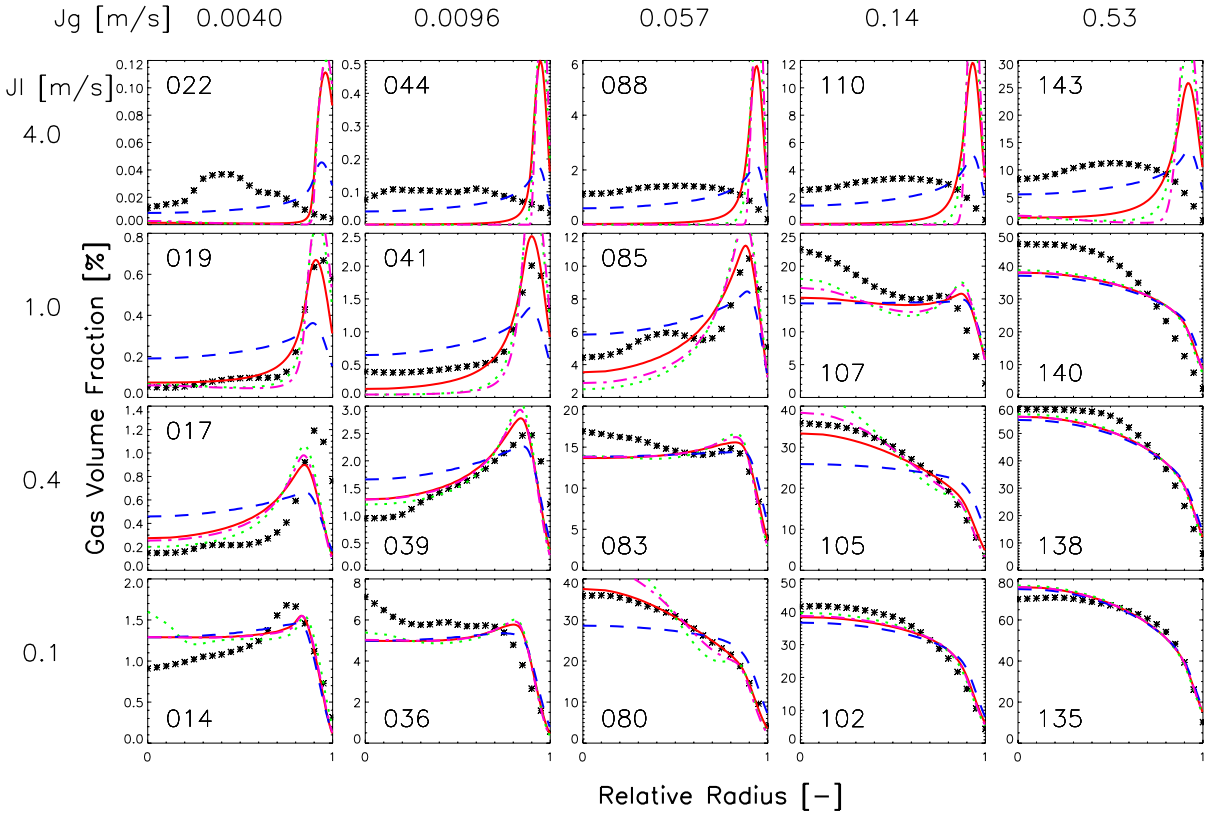

Fig. 3.9 Modifications of dispersion force models: stars: Experiment, red solid lines FAD model eq. (2.24), green dotted lines - FAD model eq. (2.24) divided by 2, blue dashed lines - FAD model eq. (2.24) multiplied by factor 5, magenta dotted-dashed lines - Bertodano model eqs. (2.22) and (2.23). All models are used with an additional consideration of bubble dimensions.

A comparison of the different wall forces, eq. (2.17) and eq. (2.18) combined with the deformation force, eq. (2.21) is given in Fig. 3.10. Here also a lift force according to eq. (2.11) and a dispersion force according to FAD model, eq. (2.24) is applied. The resulting radial gas volume fraction profiles are very similar. There is no clear trend which of the forces is more suitable for the modelling of vertical pipe flow.

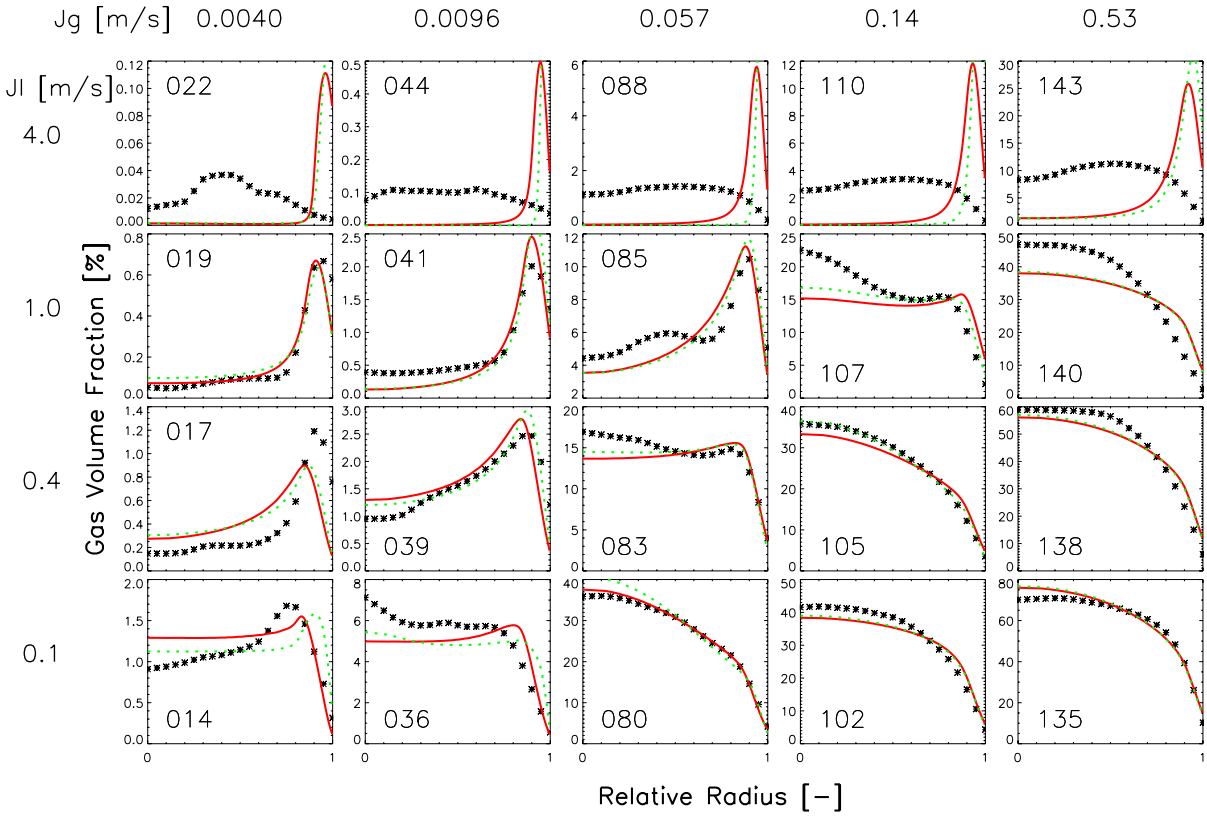

Fig. 3.10 Effect of different wall forces: stars - Experiment, red solid lines - eq. (2.17), green dotted lines - eqs. (2.18) and (2.21)

As mentioned above a clear disagreement occurs for large liquid superficial velocity. The occurrence of an intermediate peak is also known from literature. It is assumed, that it is connected with anisotropic turbulence. An increase of the turbulent dispersion force leads to a more flat profile, but no noteworthy shift of the wall peak as demonstrated in Fig. 3.11. The figure also indicates, that an increase of the wall force shifts the peak, but the shape of the profile remains different from the measured one. Also combined increase of both forces does not results in a satisfactory agreement of calculated and measured profiles, i.e. none of the forces discussed in chapter 2 is suitable to reproduce the intermediate peak. Two-phase turbulence has to be considered for modelling an appropriate force.

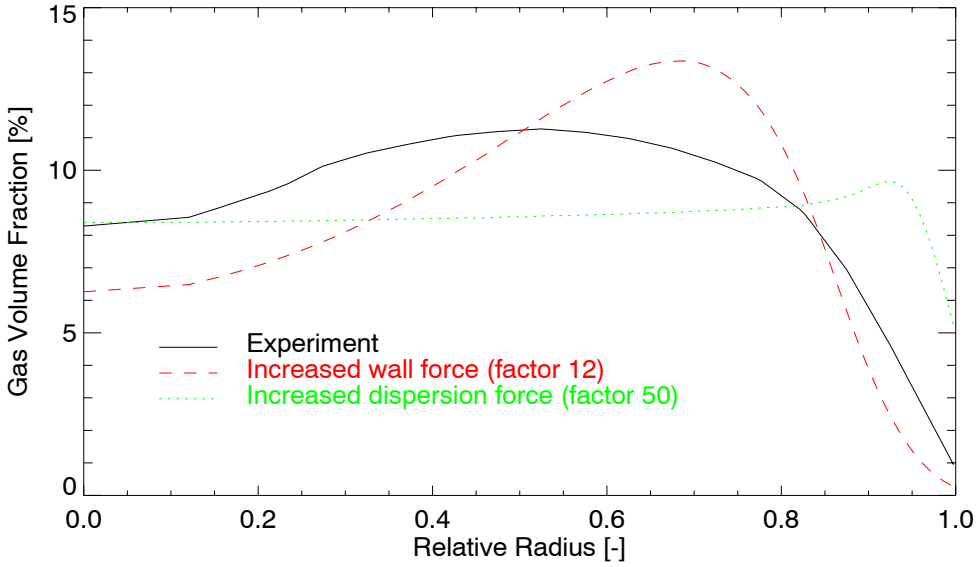

Fig. 3.11 Influence of the wall and the dispersion forces on the radial profiles in case of a measured intermediate peak, Jl = 4 m/s, Jg = 0.538 m/s

In the result of the investigations for the DN50 pipe it was found, that a set of the Tomiyama lift and wall force combined with the Favre averaged dispersion force reflect the experimental dates with the best agreement. As shown above similar results are obtained with the modification of the wall force coefficient by Hosokawa (eq. (2.18)) if it is combined with the deformation force (eq. (2.21)). Fig. 3.12 shows the results for a more extended part of the matrix measured. The transition from wall to centre peak is well predicted. The quantitative agreement is also satisfyingly despite for large water superficial velocities.

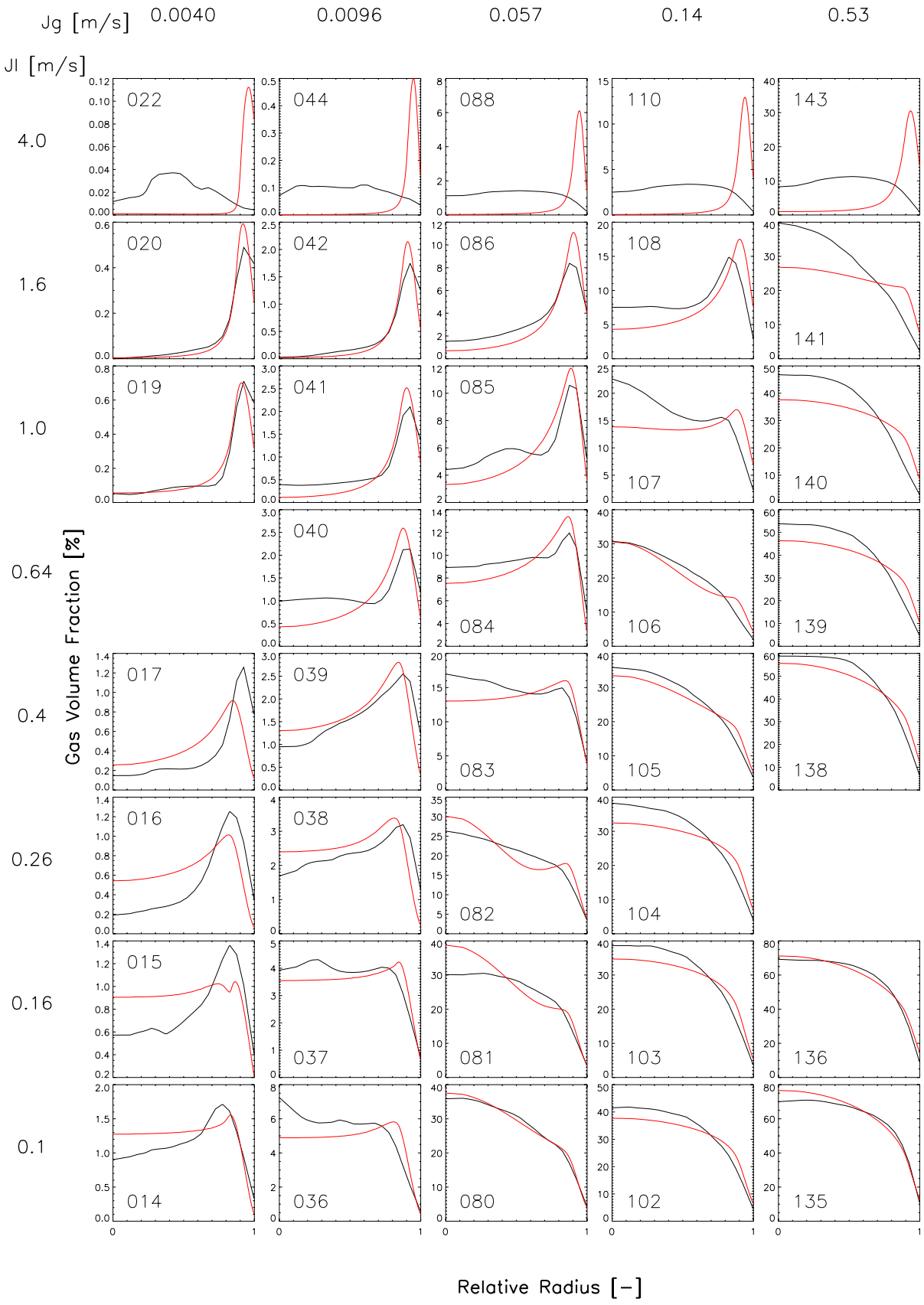

Fig. 3.12 Comparison of measured and calculated radial profiles of the gas volume fraction using the Tomiyama lift and wall force and the Favre averaged dispersion force for the MTLoop pipe (DN50).

3.3.2 Analyses for the DN200 pipe

The same set of forces was used without any modification or tuning for the analysis of experimental results obtained at the TOPFLOW facility for the large (DN200) pipe. In this section data from the vertical test pipe with air injected by a specific bubbling skittle (VTS) were used. In this case the inner pipe diameter is equal to 194.1 mm, the position of the wire-mesh sensor is located 7.66 m above the gas injection (L/D = 40). The details of the measurements are presented in the Technical Report "Experiments on upwards gas-liquid flow in vertical pipes". For the calculations the radius of the pipe was divided into 150 nodes of equal volume. The last node was subdivided in 10 nodes for the calculation of the profile of the radial water velocity according to the recommendations of the Sato-model. The bubble size distribution was represented in the calculations by 45 bubble classes with an increasing width. Variations of the number of nodes and bubble classes showed, that this guarantees the independency of the results from the discretisation.

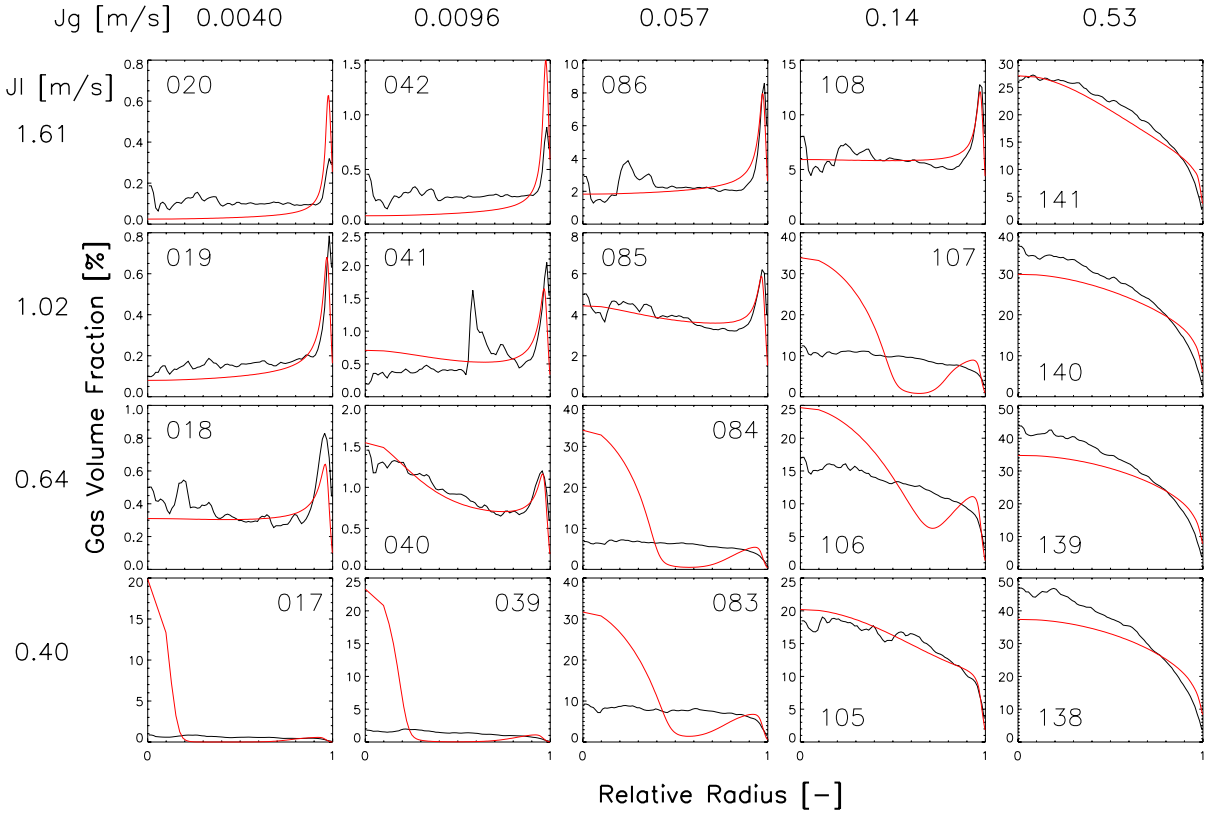

Fig. 3.13 Comparison of measured and calculated radial profiles of the gas volume fraction using the Tomiyama lift and wall force and the Favre averaged dispersion force for the DN200 pipe at TOPFLOW facility.

A very good agreement was achieved for all cases with a wall peak (Fig. 3.13). Also the transition from wall to centre peak is well predicted. But for most cases with a centre peak, the lift force is too strong compared to the dispersion force. This leads to a concentration of almost all large bubbles in a narrow region at the centreline of the pipe. This is caused by a positive feedback: Because of the lift force bubbles migrate to the pipe centre and increase the liquid velocity in this region and with that also its gradient. A higher gradient of the liquid velocity again causes an enlargement of the

lift force and in the results still a closer concentration of the bubbles near the centreline. The only force, which may stop this process is dispersion force. First calculations using the option of a dynamical migration of the bubbles instead of the assumption of equilibrium of the forces showed, that these migration process are much slower in case of the DN200 pipe compared to the DN50 pipe. The reasons are the lower gradients and the larger dimensions. Thus possibly the assumption of an equilibrium of the forces is not fulfilled in this case and this may be the reason for the discrepancy. Other possible reasons are shortcomings in the modelling of liquid turbulence for two-phase flows, which influences the liquid velocity profile and thus the above discussed feedback. Here further investigations are required.

Despite of this deficiency, the results show, that the chosen equations for the non-drag bubble forces are to certain extend scale-independent and the developed model is able to cover different geometric scales.

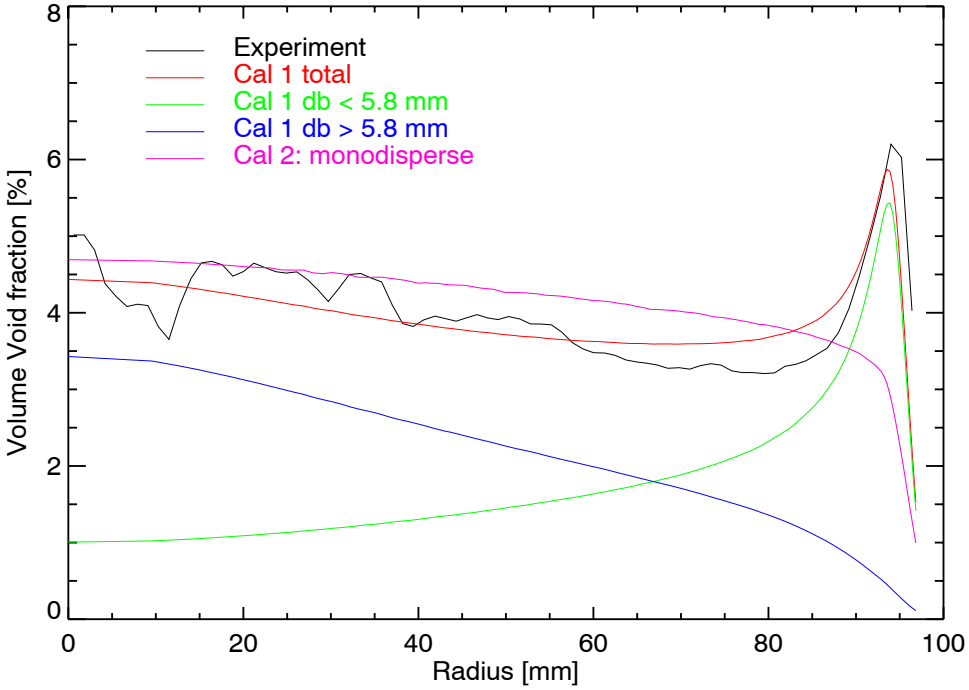

Fig. 3.14 Measured and calculated gas volume fraction profiles for the DN200 pipe, test 085 (J_L = 1.02 m/s, J_G = 0.057 m/s). In the calculation CAL 1 the measured bubble size distribution was considered, while in CAL 2 only an averaged bubble diameter was used. The green und blue lines decompose the total gas volume fraction (red line) according to the bubble size.

The bubble size distribution has a strong influence on the radial profiles. Ohnuki and Akimoto (2000) used in their investigations an averaged bubble diameter, but also stated that the influence of the spectrum of bubble sizes should be carefully investigated. For this reason two calculations were made for test 085 (J_L = 1.02 m/s, J_G = 0.057 m/s), one considers the measured bubble size distribution, the other uses only one bubble class with an average bubble diameter of 5.88 mm derived from the distribution. The results are shown at Fig. 3.14. There is a wall peak for the calculation, which considers the measured bubble size distribution (CAL 1), but a core peak if only an averaged bubble diameter is considered (CAL 2). The reason is

shown by a decomposition of the total gas volume fraction profile according to the bubble size. Fig. 3.14 also includes the partial gas fraction profiles, formed by bubbles smaller and larger 5.8 mm. This example demonstrates, that he consideration of the bubble size distribution is essential at least for cases where most of the bubble are in range of about 3 mm – 7 mm of equivalent bubble diameter.

3.3.3 Scaling considerations

A discussion on scaling effects for the DN50 and DN 200 pipes can be found in Lucas et al. (2004). Fig. 3.15 shows a comparison of measured and calculated gas volume fraction profiles for the two scales for J_l = 1.02 m/s and J_g = 0.015 m/s (test 052). For these parameter the measured bubble size distributions at the upper end of the pipe (L/D = 60 for DN50 and L/D = 40 for DN200) are approximately the same. For both calculations the same bubble size distribution and total gas volume fraction were used, namely those measured in the DN200 pipe, to exclude influences resulting from different bubble sizes and gas fraction. Thus the only difference in the calculations is the diameter of the pipe. The wall peak is shifted to a higher relative radius and appears sharper in the DN200 pipe compared to the DN50 pipe. As shown in the right part of the figure, the absolute distance of the peak from the wall is nearly the same in both cases, which can be understood as a result of the equilibrium of lift force and wall force. The calculated as well as the measured peaks are higher in the DN200 pipe. In the core region of the pipe the measured and calculated volume gas fraction is slightly higher in the large pipe.

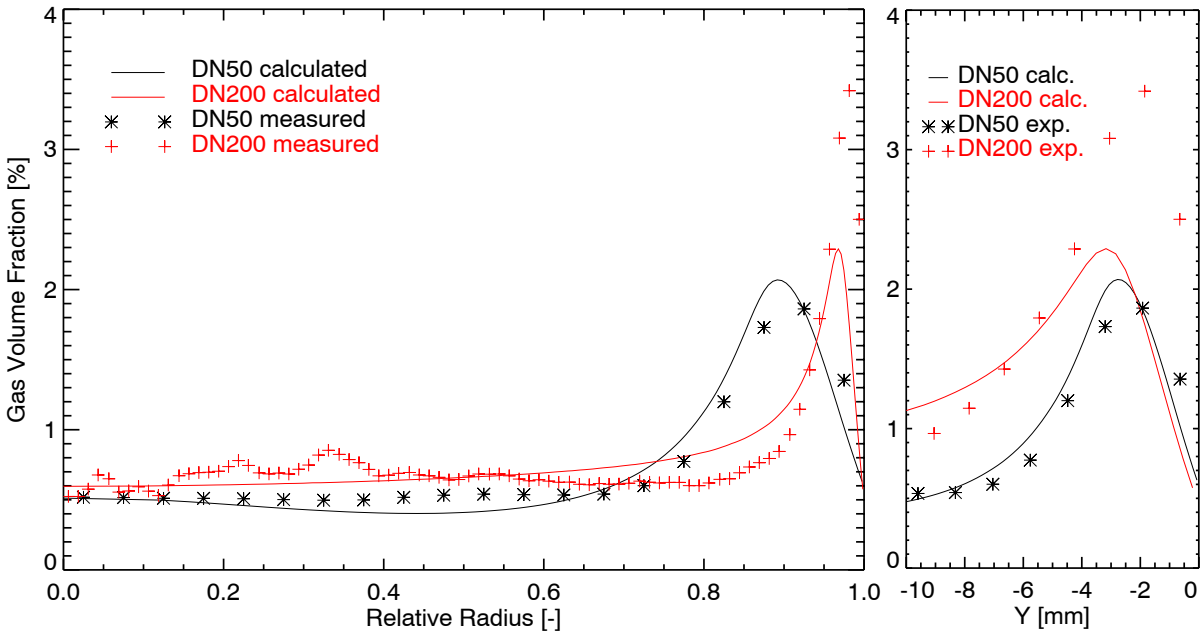

Fig. 3.15 Comparison of measured and calculated gas volume fraction profiles for both pipes, J_L = 1.02 m/s, J_G = 0.015 m/s (test 052), Y is the absolute distance from the wall

All these effects can be explained by the changes of the radial profiles of the liquid velocity. In terms of the relative radius the gradient of the liquid velocity is larger in the near wall region for the large pipe, but lower in the core region, as Fig. 3.16

shows. This causes the high sharp wall peak in case of the DN200 pipe compared to the DN50 pipe.

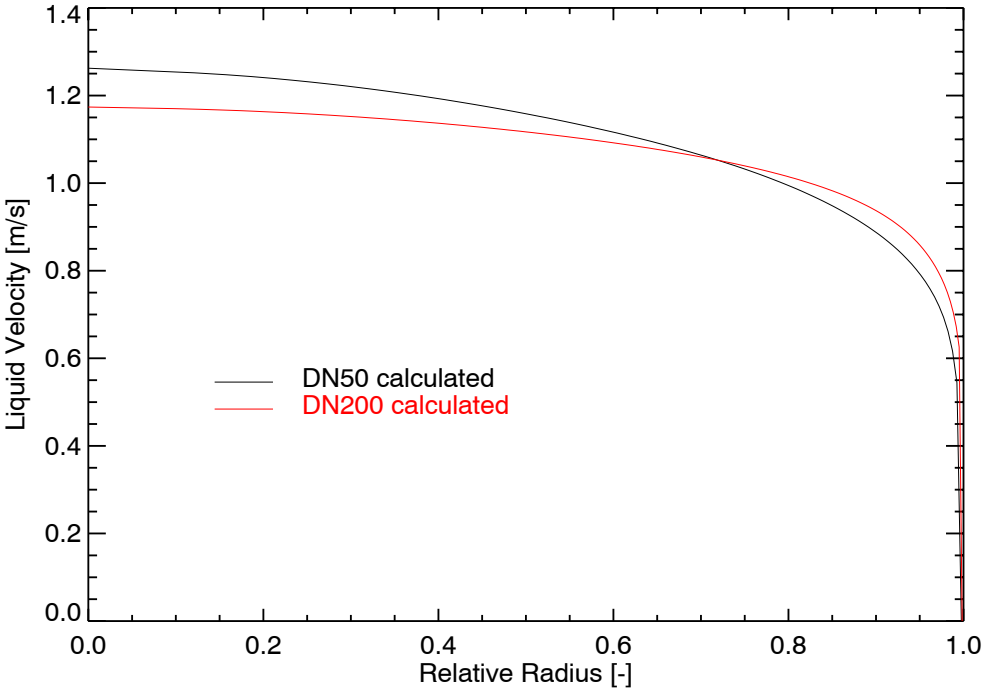

Fig. 3.16 Comparison the calculated liquid velocity profiles, J_L = 1.02 m/s, J_G = 0.015 m/s

One could assume to find a better similarity in the radial gas fraction profiles, if the radial profiles of the liquid velocity are more similar. For this reason the following analysis is made for two cases with approximately the same Reynolds number for the liquid and the same total volume gas fraction of about 1%, rather than for the same combination of superficial velocity.

To do this analysis, again the measured bubble size distribution and total gas volume fraction from DN200, test 052 (J_L = 1.02 m/s, J_G = 0.015 m/s) were used as an input of the calculation, but different values for the superficial velocities. For the small pipe the calculation was done using superficial velocities of J_L = 1.61 m/s, and J_G = 0.024 m/s (test 064) and for the large pipe the superficial velocities of J_L = 0.40 m/s and J_G = 0.0062 m/s (test 028). For all these combinations of superficial velocities the measured gas volume fractions are approximately the same. Thus the above mentioned assumptions for the calculations are close to reality. The pipe Reynolds numbers for the single phase liquid flow:

$$\mathrm{Re}_l = \frac{\rho_l J_L D}{\mu_l} \tag{3.21}$$

is also about the same in both cases. Instead of a scaling with equal gas and liquid superficial velocities, this is a comparison for equal single phase liquid pipe Reynolds number and equal gas volume fraction. Nevertheless the calculated gas volume fraction profiles differ significantly as Fig. 3.17 shows.

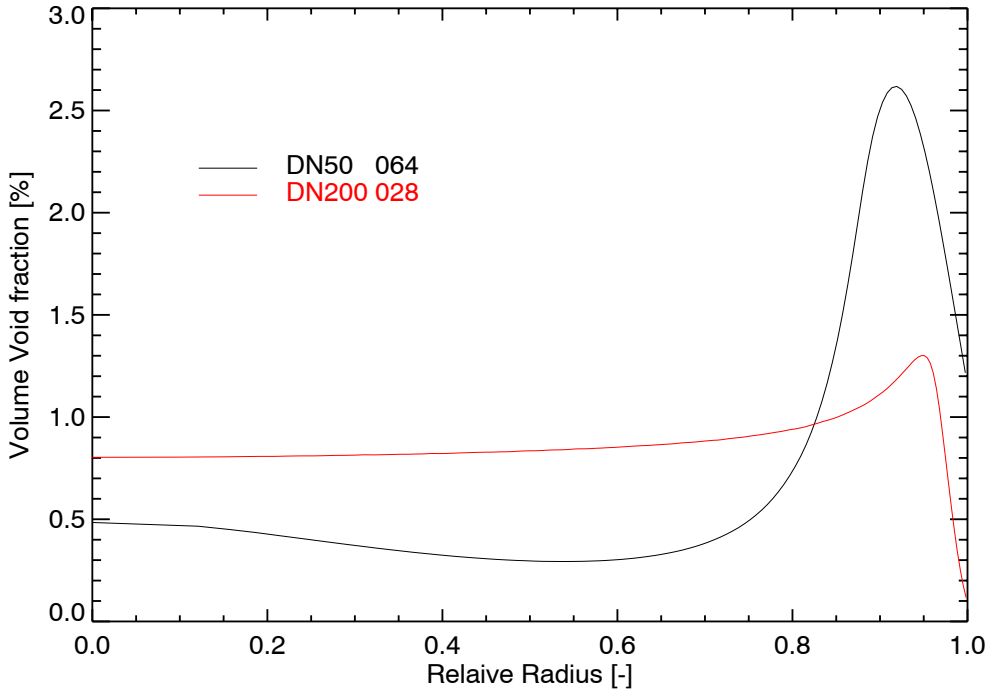

Fig. 3.17 Calculated gas volume fraction profiles in case of equal pipe Reynolds number of the liquid and equal total gas volume fraction. The bubble size distribution was always taken as the measured one for DN200, point 052. Superficial velocities for the simulation are taken according to tesr 064 (J_L = 1.61 m/s, J_G = 0.024 m/s) for the DN50 pipe and test 028 (J_L = 0.40 m/s, J_G = 0.0062 m/s) for the DN200 pipe.

Fig. 3.18 indicates, that also the radial profile of the liquid velocities differs for both cases. The reason is the deformation of this profile induced by the bubbles, which is important even at this low gas volume fraction. This is illustrated by the fact that the radial profiles are practically the same when the gas is absent (green and blue curves in Fig. 3.18, which are practically the same). The profile in the small pipe is mainly dominated by the wall shear and wall-generated turbulence because of the small tube diameter and the high liquid velocity. For this reason the profile of the liquid velocity for the small pipe is similar to the single phase profile. On the other hand, the larger dimensions and the lower liquid velocities in the large pipe lead to much lower influence of the wall shear stress and the effect of the bubble buoyancy on the liquid velocity profile becomes dominating. Thus in this case the profile clearly differs from the single phase profile.

The lower velocity gradients in the core region of the large pipe lead to the higher gas volume fraction in this region compared to the small pipe. This is mainly caused by a change of the lift force, since the turbulent dispersion, which is proportional to the turbulent viscosity of the liquid should be similar for both cases. Fig. 3.19 shows the turbulent viscosity of the liquid for the different combinations of superficial velocities. Whereas the turbulent viscosity is much larger in the DN200 pipe for the same combinations of the superficial velocity (test 052), it is quite similar for the cases with a similar pipe Reynolds number of the liquid (tests 028 <– >064).

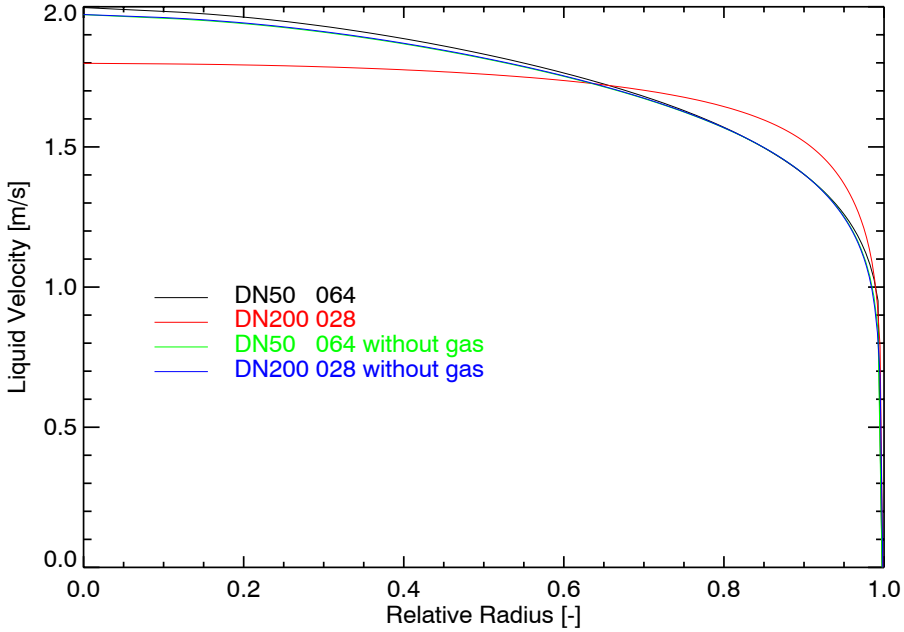

Fig. 3.18 Calculated liquid velocity profiles in case of equal pipe Reynolds number of the liquid and equal total gas volume fraction. For the black and the red line the bubble size distribution was taken as the measured one for DN200, test 052. The green and the blue line are the profiles in case of single phase liquid flow. (test 064: J_L = 1.61 m/s, J_G = 0.024 m/s, test 028: J_L = 0.40 m/s, J_G = 0.0062 m/s).

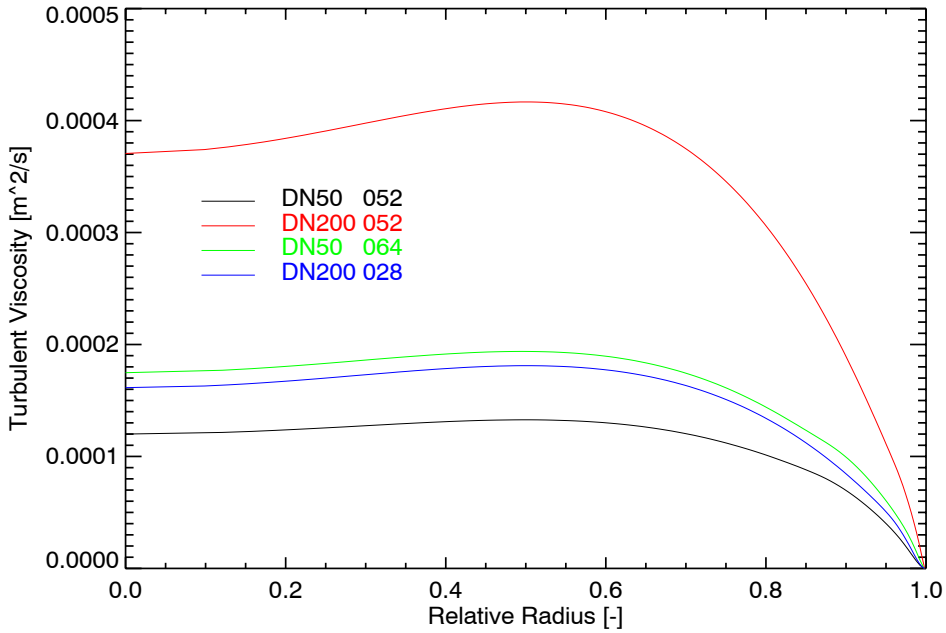

Fig. 3.19 Calculated profiles of the turbulent viscosity of the liquid. in case of equal pipe The bubble size distribution was always taken as the measured one for DN200, test 052 (J_L = 1.02 m/s, J_G = 0.015 m/s). (test 064: J_L = 1.61 m/s, J_G = 0.024 m/s, test 028: J_L = 0.40 m/s, J_G = 0.0062 m/s).

For the combinations of superficial velocities of gas and liquid, where a wall peak occurs in the small pipe but a core peak in the large pipe there are also differences in the bubble size distributions. The bubble size distributions are broader and the average bubble diameter is larger in case of the DN200 pipe. This is clearly the reason for the change of the radial profile, as the calculated radial gas volume fraction profiles in Fig. 3.12 and Fig. 3.13 show. The remaining open question is why the bubble size distributions differ in small and large pipes. It is discussed in the next section, since to answer this question the development of the flow along the pipe has to be taken into account.

The above shown analyses indicate, that no general scaling similarity can be found because of the different scaling behaviour of the non-drag bubble forces. The interaction between the bubbles and the liquid flow field leads to non-linear effects. On the other hand, local, meso-scale models have the capability to achieve scale-independent modelling, when embedded into a two-fluid model.

3.4 Analyses for developing bubbly flow

The Multi Bubble Size Class Test Solver with the extension for radial bubble migration was applied for the simulation of the development of a bubbly flow observed in the TOPFLOW VGE experiments (see Technical Report “Experiments on upwards gas-liquid flow in vertical pipes”). In this case the inner pipe diameter is 195 mm and the height 7.8 m. Gas was injected by rows of 1 mm or 4 mm orifices in the pipe wall respectively. The distance between gas injection and measuring plane (i.e. the wire-mesh sensor) was varied by using different height positions for the injection. Fig. 3.20 shows the distances for the different levels.

45 bubble size classes with increasing width covering the range from 2 mm up to 100 mm of equivalent bubble diameter were used. In the calculations the gas injection was always assumed to be located at the lower end of the pipe (height position 0 m). For the comparison with experimental data, obtained in the tests as described above, the same vertical distances between the injection and the corresponding levels were applied, i.e “Level R” marks the parameter calculated at the position 7.802 m above the gas injection. The initial bubble size distribution was taken from the measured bubble size distribution for the shortest distance between the gas injection and the wire mesh sensor (level A, 221 mm), i.e. it was assumed, that the initial bubble volumes do not depend on the pressure. The fact that the pressure is up to 76 kPa (0.76 bar) higher at level R compared to the upper end of the pipe (slightly depending on the average gas volume fraction) was neglected.

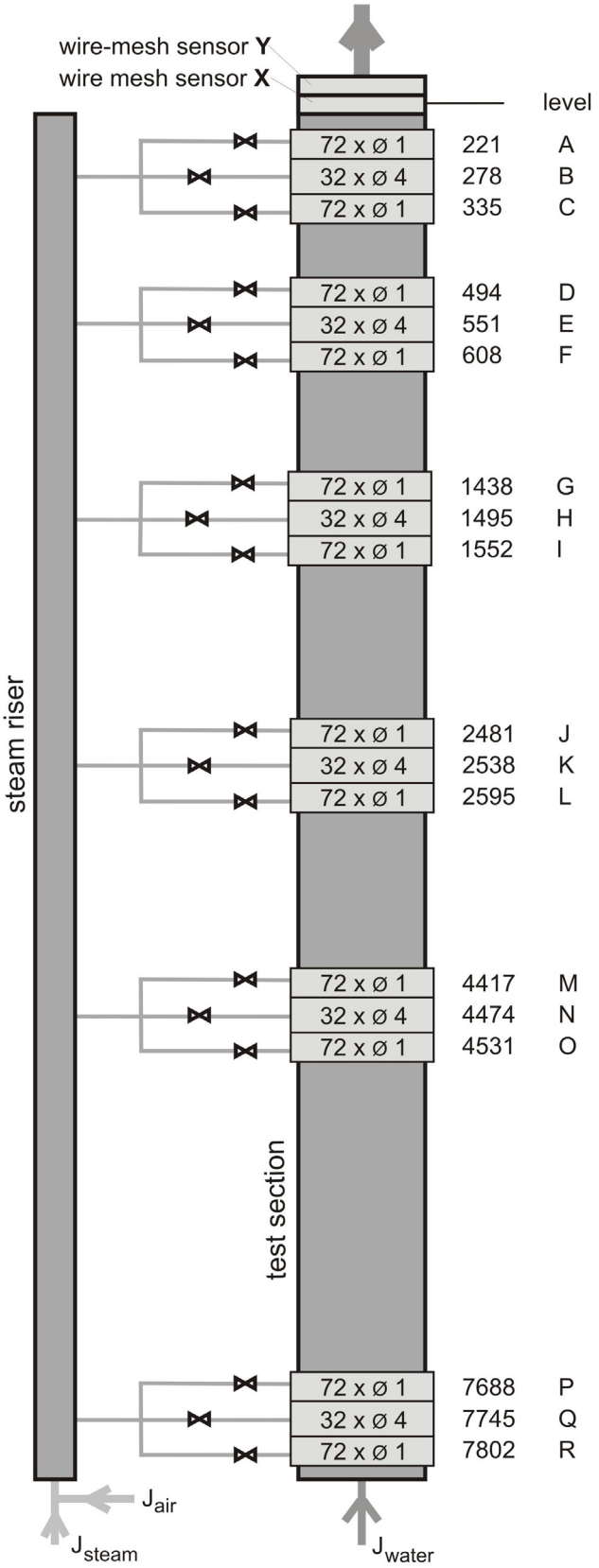

Fig. 3.20 Vertical pipe with variable gas injection. For levels B, E, H, K, N and Q the gas injected via 4 mm orifices, for the other levels via 1 mm orifices. Distances in mm.

3.4.1 Initial radial gas fraction profiles in case of injection of large bubbles

In first calculations it was assumed that the initial position of all bubbles is the radial node which is closest to the pipe wall. This led to a bubble migration towards the pipe centre much faster than observed in the experiments. This was possibly caused by the large initial momentum, transferred to the bubbles because of the action of the wall force or the deformation force. To test this hypothesis, in the next calculations the initial bubble positions were set according to the bubble diameter, i.e. the centre of mass of the bubbles was assumed to be at a distance from the wall equal to the bubble radius. For the repellent effect of the wall only the deformation force was considered, which vanishes for distances larger the bubble radius. These test calculations showed, that the effect of an initial momentum is of less importance and the velocity of the bubble migration from the pipe wall towards the pipe centre has only a very weak sensitivity on the initial bubble position, provided it is close to the wall. The bubbles reach very quickly a velocity, which is determined by equilibrium of the drag force and the non-drag forces. The virtual mass force is less important.

Nevertheless the Tomiyama wall force pushes the bubble away from the wall too strongly for most of the cases. On the other hand the deformation force acts only within a distance from the wall that is less than the equivalent radius of the bubble and the correlation for the wall force coefficient by Hosokawa et al. (2002) results in lower values for the wall force compared to Tomiyama in case of small bubbles. For this reason, the deformation force was applied together with the Hosokawa wall force correlation. This combination of forces was already identified during the analyses for fully developed flow as suitable wall force modelling (see section 3.3).

In case of high gas volume flow rates large bubbles are generated at the injection site. The left hand side of Fig. 3.21 shows the bubble size distribution measured close to the injection at level A for J_l = 1.017 m/s and J_g = 0.219 m/s. The right hand side compares the corresponding measured gas volume fraction profile with the profile, which is obtained, if all bubbles are assumed to have an elliptical shape (according to Wellek et al., 1966) and to be located in a distance from the wall equal to their horizontal radius. Even for this assumption the calculated gas volume fraction profile is too broad. This can only be explained by bubble shapes, which are stretched in vertical direction.

This assumption can be proofed by the data obtained by the wire-mesh sensor. Fig. 3.22 compares bubble size distributions obtained for the equivalent bubble diameter (diameter of a sphere with a volume equal to the measured bubble volume) with distributions based on the horizontal dimension of the bubbles. The bubble diameter used as axis of abscissa in the bubbles size distributions hxy are calculated as the equivalent diameter of the maximum horizontal cross section area of the bubble and for the distributions hr as the maximum extension of a bubble in radial direction. The shift of the bubble size distribution hxy to smaller bubble sizes compared to the bubble size distribution h testifies the above mentioned stretching of the bubbles in vertical direction. Since there is again a shift to smaller bubble sizes for the distribution hr, the bubbles are also more extended in azimuthal direction compared to the radial direction. As the figures show these strong deformations of the bubbles vanish with increasing L/D. To avoid the uncertainties connected with the distorted shapes of large bubble in following cases are considered, in which much smaller bubbles are injected.

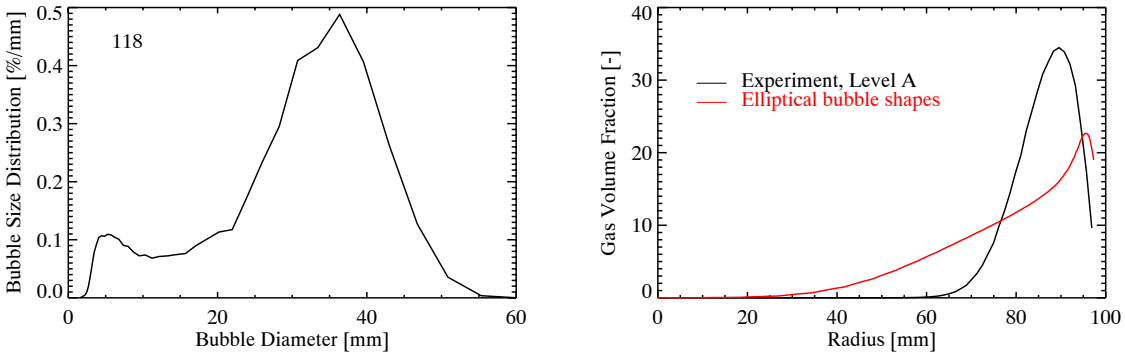

Fig. 3.21 Measured bubble size distribution (left) and radial gas volume fraction profile (right) for gas injection Level A (0.221 m below the wire-mesh sensor). J_L = 1.017 m/s, J_g = 0.219 m/s. The red curve represents the radial gas fraction profiles, which would be present, if all bubbles are ellipsoidal and located in a distance from the wall equal to their equivalent radius. Since such bubbles would be extended inside the wall, they are cut off at the pipe wall and renormalized.

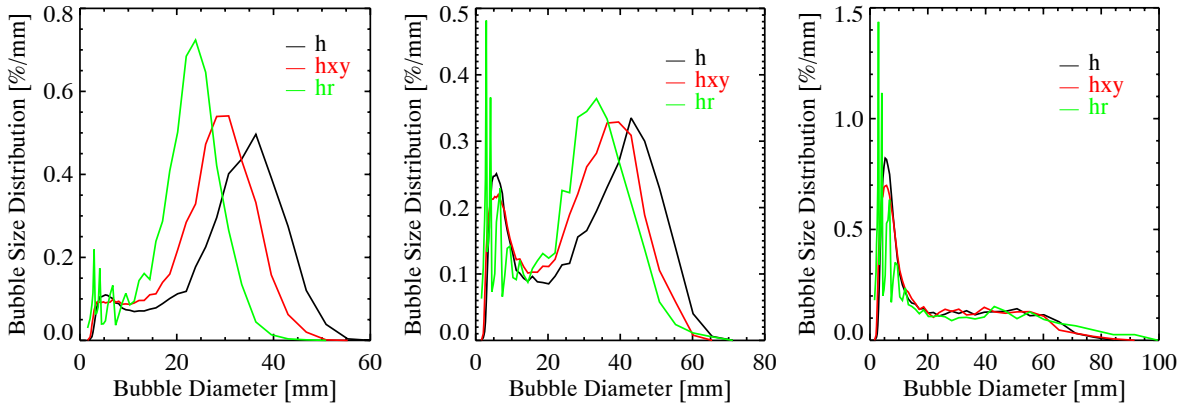

Fig. 3.22 Measured bubble size distributions for 3 different gas injection levels. J_L = 1.017 m/s, J_g = 0.219 m/s. At the black curves the axis of abscissa is calculated according to the volume equivalent bubble diameter. For the red curves the maximum horizontal cross section area was used for the calculation of an equivalent radius. The green curves base on bubble extension in radial direction.

3.4.2 Radial migration of small bubbles

But also for smaller bubbles, in case of which the bubble shape is of less importance, the radial bubble migration from the pipe wall towards the centre is faster in the simulations compared to the experimental results. Fig. 3.23 shows two examples. The total gas volume fraction differs in experiment and calculation, because of the different pressure. In the experiment the sensor is always located at the upper end of the pipe, i.e. the measurement is done at nearly ambient conditions. On the other hand, the calculation considers the increased pressure at the lower positions within the pipe. For this reason, the gas volume fraction is lower in the calculation compared to the experiment, but also the shapes of the profiles differ for the same height. The profiles measured at level L (2.4 m) look similar to the calculated ones for

level F (0.6 m). There is also a similarity of the profiles for the experimental data, level O (4.5 m) and the calculated data for level L (2.4). This indicates clearly, that the calculated bubble migration is too fast.

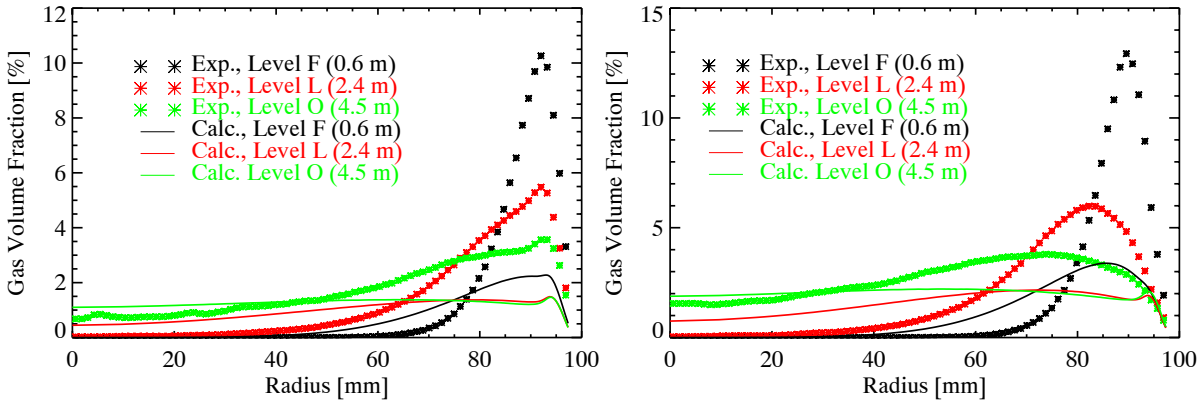

Fig. 3.23 Comparison of measured and calculated radial gas volume fraction profiles for different distances from the gas injection. Left: J_L = 1.017 m/s, J_g = 0.0235 m/s, Right: J_L = 1.017 m/s, J_g = 0.0368 m/s.

The main driving force, which pushes the bubbles towards the pipe centre, is the turbulent dispersion force. This is demonstrated in Fig. 3.24. It compares gas volume fraction profiles calculated using the complete set of bubble forces with results obtained when lift and wall forces are switched off. There are some differences in the near wall region, but in both cases the radial redistribution is clearly faster in the calculations, compared to the experiment. In the central region of the pipe there is almost no difference between the two calculations.

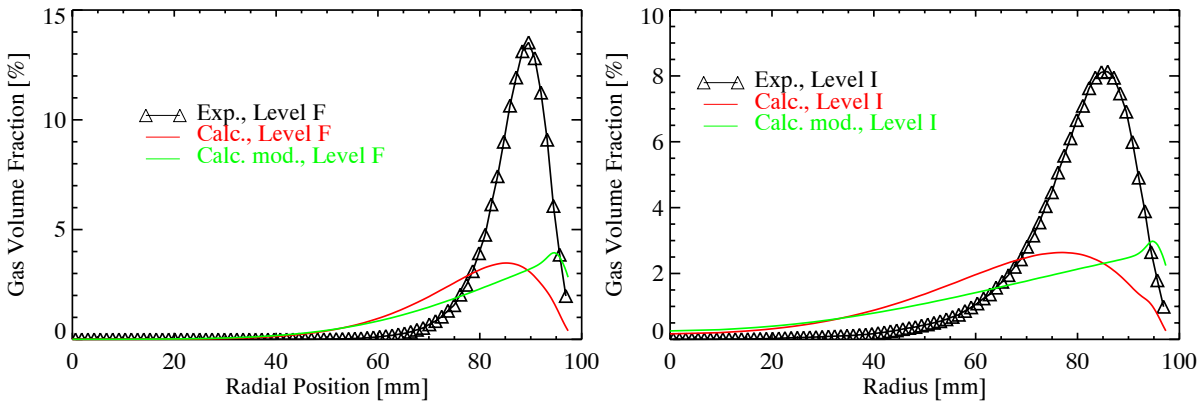

Fig. 3.24 Comparison of measured and calculated radial gas volume fraction profiles for Level F (0.6 m) and Level I (1.6 m). J_L = 1.017 m/s, J_g = 0.0368 m/s. The green curves show the results from a modified calculation, for which the lift and wall (and deformation) forces were switched off.

The turbulent dispersion force is proportional to the turbulent viscosity. Since a turbulence model was used, a comparison with results from a CFD calculation (CFX 5.7, SST model for liquid turbulence) was feasible for a simplified test case using

only one bubble class. The same superficial velocities were taken as in Fig. 3.24, but now a mono-dispersed bubbly flow with a uniform bubble size of 4.5 mm was assumed for both calculations. Fig. 3.25 compares radial gas fraction profiles as well as the turbulent viscosity calculated by the two models for this test case. There are of course some differences in the profiles, but they are still in acceptable agreement when we keep in mind the quite different modelling. At least the velocity of the bubble migration towards the pipe centre is comparable in both calculations. Thus the differences between experiment and simulation suggest, that the turbulent dispersion force is too large compared to the drag in radial direction. One reason could be, that not all eddies contribute to the bubble dispersion. Only eddies with a dimension comparable to the bubble diameter or larger are able to transport the bubble.

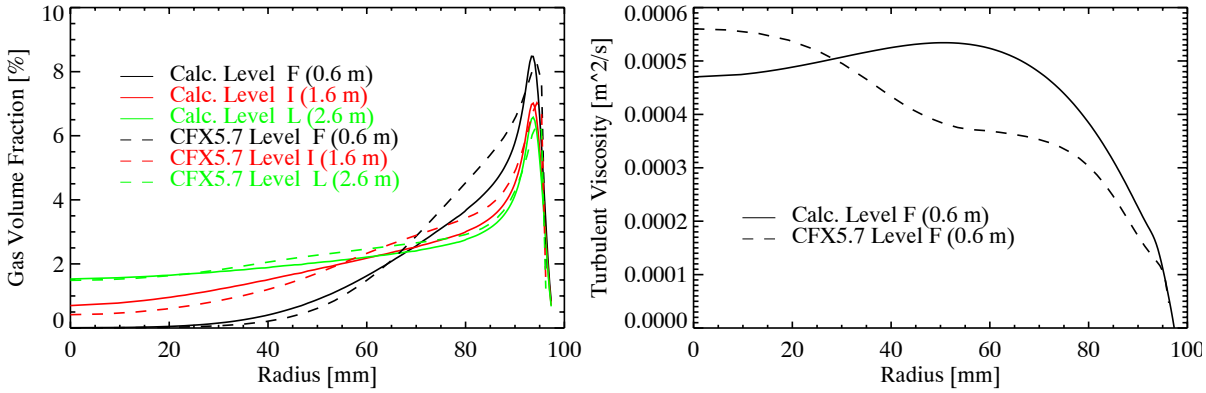

Fig. 3.25 Comparison of radial gas volume fraction profiles and turbulent viscosity profile calculated by the simplified model and CFX-5.7 for a test case at J_L = 1.017 m/s, J_g = 0.0368 m/s.

3.4.3 Evolution of the bubble size distribution

While bubble coalescence and fragmentation are less important for the radial redistribution close to the injection, it generally influences the evolution along the pipe. Previous investigations for a pipe with an inner diameter of 51.2 mm (Lucas et al., 2001b) have shown, that models for bubble coalescence and break up, which can be found in literature, differ in a wide range and their applicability is limited. These findings were confirmed by the present investigations. For this reason again the simplified models introduced by Lucas et al. (2001b) were applied. By tuning the model constants, a satisfactory simulation of the evolution of the bubble size distribution can be obtained for some combinations of gas and liquid volume flow rates, but no set of constants was found, which can be used to reflect the experimental findings in the wide range of volume flow rates covered by the experiments.

For combinations of a liquid superficial velocity of 1 m/s or higher and gas superficial velocities up to 0.037 m/s the changes of the bubble size distributions along the pipe are low. For this reason, calculations were done both applying the simplified models for bubble coalescence and breakup (Calc. a) as well as without the consideration of bubble coalescence and breakup. For the latter case calculations were done with (Calc. b) and without (Calc. c) consideration of the change of the bubble size distribution caused by expansion of the bubbles due to the pressure drop along the

pipe. Fig. 3.26 compares calculated bubble size distributions and radial gas volume fraction profiles for the upper end of the pipe (Level R, 7.802 m) with measured data for the gas injection at level R.

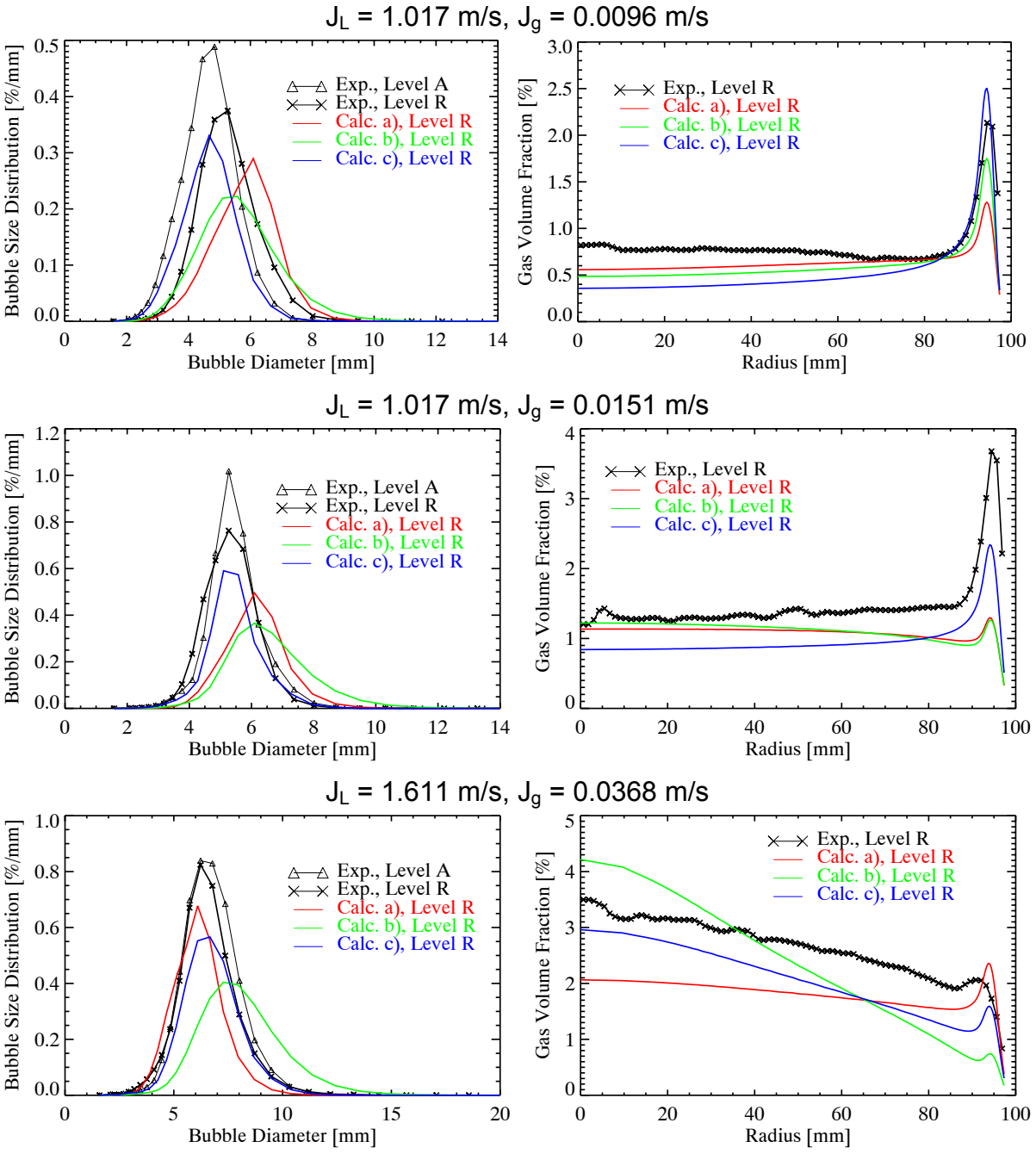

Fig. 3.26 Comparison of measured and calculated bubble size distributions (left) and radial gas volume fraction profiles (right) for Level R (7.8 m). Calc. a): with bubble coalescence and breakup, Calc. b): bubble coalescence and breakup switched off, Calc. c) in addition to Calc b) now also the bubble expansion caused by the pressure decrease is switched off.

For these cases a nearly fully developed flow is achieved at the upper end of the pipe. For this reason, these profiles do not depend on the velocity of the radial bubble migration. There is an acceptable agreement between the calculated and measured radial profiles for those calculations, which result in the best agreement with the measured bubble size distribution, too.

For the tuning of the constants for the coalescence and breakup models, the two cases shown in the Fig. 3.27 were considered. According to this tuning the calculated bubble size distributions at the upper end of the pipe show an acceptable agreement with the measured ones. The radial gas volume fraction profiles are also plotted for comparison.

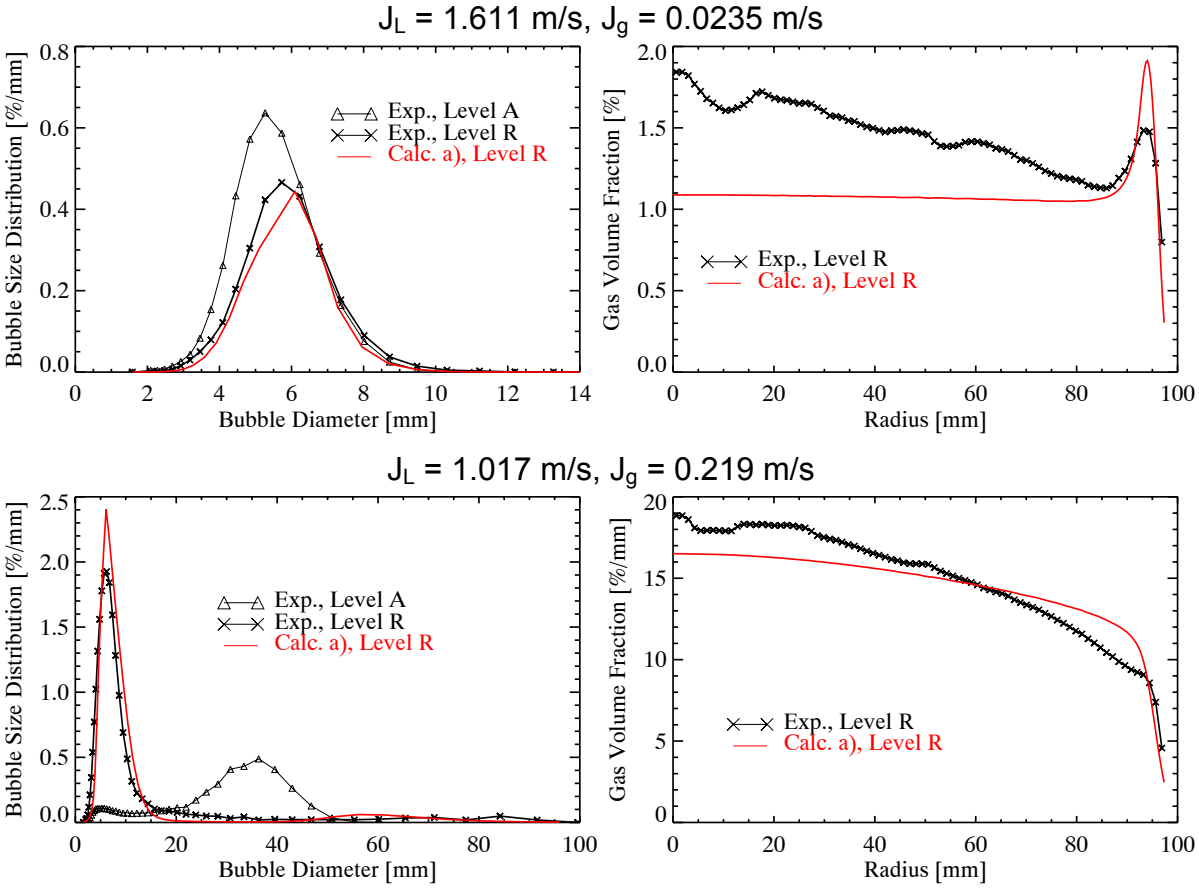

Fig. 3.27 Comparison of measured and calculated bubble size distributions (left) and radial gas volume fraction profiles (right) for Level R (7.8 m).

3.4.4 Scaling consideration

The remaining open question from the discussion on scaling effects in section 3.3.3 was related to the difference of bubble size distributions in the small (DN50) and large (DN200) pipes. There are some contradictory influences on the development of the flow. The first effect, which has to be considered, is the initial bubble size. Even if very similar bubble injection devices are used, there may be a difference in the size and spectrum of the initial bubbles. In our experiments as well as for the investigations from Ohnuki and Akimoto (2000) small and large pipes of different length were used. If there is atmospheric pressure at the upper end of the pipe, the

pressure differs at the location of the injections device because of the different pipe lengths, which may cause different initial bubble sizes (see experimental investigations discussed in the Technical Report “Experiments on upwards gas-liquid flow in vertical pipes”).

Assuming that the initial bubble size is the same for both pipes, analyses using the simplified model were made for the transition region between wall and core peak at the radial gas fraction profile. The following effects were identified to influence the development of the flow along the pipes in a different way.

Scaling regarding bubble coalescence and breakup: While L/D may be an acceptable parameter to compare the development of radial profiles, bubble coalescence and breakup are time dependent processes. As shown in some papers (Lucas et al. 2001b, 2003a) in most cases there is no fully developed flow at the upper end of the pipes regarding bubble coalescence and breakup even for large L/D. In the transition region between wall and core peak at the radial gas fraction profile ongoing bubble coalescence was observed also at the upper end of the pipes. That means that the bubble size distributions should be compared at the same L instead at the same L/D. In case of the two pipes considered in this work this effect should lead to larger bubbles at the upper end of the longer DN200 pipe compared to the DN50 pipe.

Pressure effect: The given air superficial velocity is always the gas volume flow rate at ambient conditions (i.e. it is the air superficial velocity at the upper end of the pipe). That means that the air flow rates and thus the gas volume fraction are lower in the lower part of the longer pipe. In case of the same initial bubble size the lower gas volume fractions leads to a lower bubble density in the large pipe. This reduces the coalescence drastically, because the coalescence rate increases proportional to the square of the bubble density. On the other hand the bubble size increases with the decreasing pressure along the pipe.

Effect of the radial gas fraction profile: There are clear differences in the radial gas fraction profiles for both pipe diameters as shown above. In many cases the calculated wall peak, which establishes along the pipe, is smaller in case of the large pipe and the gas volume fraction in the centre of the pipe is higher. In other words, the gas fraction profile is more flat, compared to the small pipe. This also reduces the coalescence rates averaged over the pipe cross section.

Effect of the bubble redistribution: The radial gas volume fraction profiles are always close to the profile that results from an equilibrium of the non-drag forces in the small pipe, while the processes of redistribution are much slower in case of the large pipe. This is caused by the large dimensions and the resulting smaller gradients.

The calculated bubble size distributions were shifted to larger bubbles in case of the larger pipe, but do not fit very well to the measured bubble size distributions. This may be also caused by the models used for bubble coalescence and breakup as discussed above. No clear trend regarding the different shapes of the radial profiles were observed. Further investigations should compare pipes with the same length. Measurements for different distances between gas injection and the wire-mesh

sensor, which are up to now available only for the DN50 pipe, should give more detailed information.

3.5 Simulation of experiments with bubble condensation

The Multi Bubble Size Class Test Solver was used for some general tests regarding the influence and applicability of a multi bubble size class modelling for cases with phase transfer. Experimental data for bubble condensation obtain at the TOPFLOW facility using the Variable Gas Injection were used. In case of the experiments with condensation an overpressure was generated in the vertical test pipe by an globe valve, which was mounted on top of the test section (i.e. at the outlet). A detailed description of the experiments can also be found in the Technical Report "Experiments on upwards gas-liquid flow in vertical pipes". Also the experiments together with the simulations shown below are published by Lucas et al. (2007a).

3.5.1 Effects of the multi bubble class modelling

First a simple test case was used to verify the implementation of condensation models described in section 3.1.3. This test case assumes an initially uniform radial gas fraction distribution with mono-dispersed bubbles of 40 mm volume equivalent diameter. The nominal pressure was set to 1 MPa, the overpressure compared to saturation to 0.1 MPa and the initial steam volume fraction to 25%. Bubble coalescence and breakup as well as any change of pressure over the height position within the pipe were switched off in the simulation, i.e. the bubble size changes only by condensation. On the other hand condensation acts only to shrink the bubbles until they reach a critical diameter to collapse. To have the same rates of shrinking for all the bubbles, the liquid temperature was set to the averaged value for each radial node after each time step, i.e. an ideal mixing of the liquid in radial direction was assumed.

In the simulation only bubbles of the smallest bubble size group were allowed to vanish by collapsing. That means for the test case, that the bubble number density divided by the averaged fluid density related to the liquid density $\rho_{av,rel}$ according to eq. (3.18), had to remain constant, until the first bubbles occur in the smallest size group. This was used as a first test of the model.

In the results was found, that there is a slight change of this modified bubble number density during the shrinking of the bubbles. Fig. 3.28 gives examples showing the influence of bubble size classes used. The reason for this deviation is a numerical diffusion along the coordinate of bubble size. This uncertainty caused by the discretisation decreases with increasing number of bubble classes considered. For the simulation bubble classes defined on basis of equivalent bubble diameter were used. The width of the bubble size classes increases by a constant factor larger than 1. The range of bubble sizes was set from $d_{b,max}^{1}$ = 2 mm for the maximum of the smallest bubble size group up to $d_{b,max}^{N}$ = 70 mm for the largest one (according to the range of bubble sizes observed in the experiments with additional overpressure discussed above).

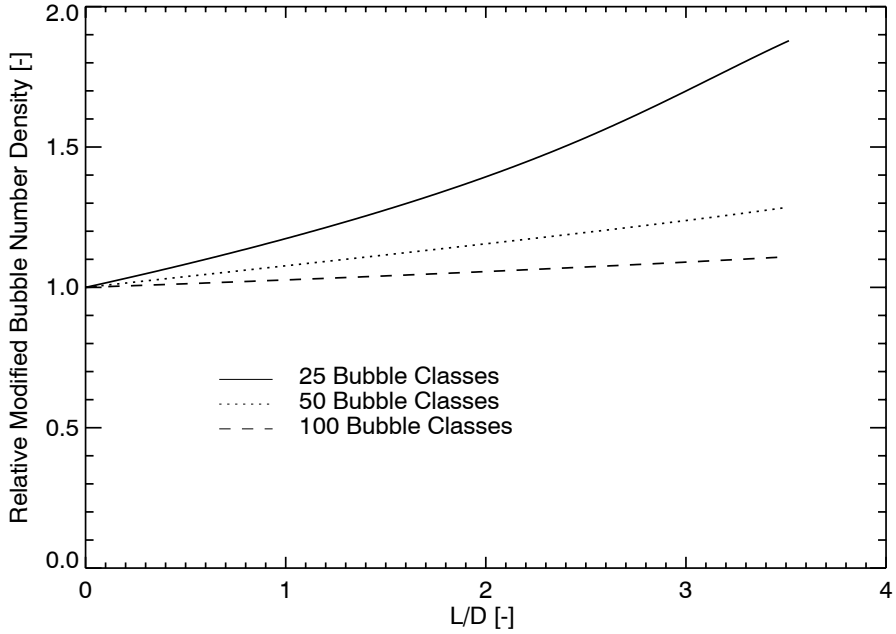

Fig. 3.28 Change of the bubble number density divided by the averaged fluid density related to the liquid density $\rho_{av,rel}$ according to equation (9) in dependence on the number of bubble size classes used.

It was found, that the numerical diffusion strongly depends on the number of bubble classes used. Fig. 3.29 compares calculated bubble size distributions obtained by 25, 50 and 100 bubble classes calculated for the instant or, respectively, vertical position in the pipe, where the gas volume decreased to 1/8th of the initial value. The initial (mono-dispersed) distributions are also included in the figure. Some small deviations from the initial diameter of 40 mm occur, because of the different width of the bubble class. Considering the associated change of the total volume, the accordant cross section averaged steam volume fraction has to be dropped down from initial value α_0 to α_1 according to

$$\alpha_1 = \frac{\alpha_0}{8 - 7\alpha_0(1 - \rho_g / \rho_l)} \tag{3.22}$$

For α_0 = 25% this equation yields α_1 = 3.993 %. Since there are no other sources for the change of bubble sizes, the equivalent bubble diameter has to be half of the initial one, i.e. about 20 mm, when this value of the void fraction is reached. As shown in Fig. 3.29 this is true for the mean value of the distributions, but there is a clear spreading of the distribution caused by numerical diffusion. The slight asymmetry of the spreading results from the non-equidistant bubble size classes.

Another test case aimed on a quantification of the improvement gained by a multi bubble size class model. Again bubble coalescence and breakup as well as changes of the bubble size caused by changes of pressure were neglected. The nominal pressure was 2 MPa, the overpressure compared to saturation set to 0.16 MPa and the initial gas volume fraction was 25%. The bubble size distribution (based on the extension of the bubbles in the horizontal measuring plane as described in the Technical Report “Experiments on upwards gas-liquid flow in vertical pipes”) measured for the gas injection via 4 mm holes at L/D = 1.4 was used as initial bubble

size distribution (see Fig. 3.30a). The evolution of the resulting cross section averaged steam volume fraction over L/D is shown at Fig. 3.30b. It is compared with different calculations using only one averaged bubble diameter, which changes according to eq. (3.19).

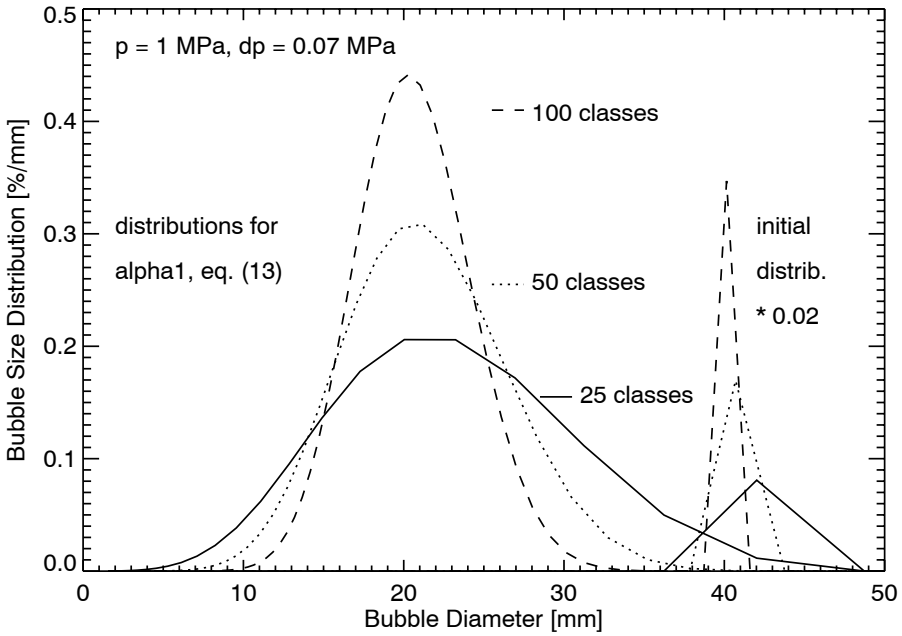

Fig. 3.29 Initial (multiplied by 0.02) and calculated bubble size distributions for the simplified test case by variation of the number of bubble size classes used.

4 different initial bubble diameters were chosen as shown in Fig. 3.30a. They were obtained from the bubble size distribution as:

Case A: volume fraction weighted bubble diameter

$$d_0^A = \sum_i \alpha_i d_{b,i} \Big/ \alpha \,, \tag{3.23}$$

Case B: volume equivalent bubble diameter

$$d_0^B = \sqrt[3]{\sum_i \alpha_i d_{b,i}^3 \Big/ \alpha} \,, \tag{3.24}$$

Case C: surface equivalent bubble diameter assuming a spherical bubble shape

$$d_0^C = \sqrt{\sum_i \alpha_i d_{b,i}^2 \Big/ \alpha} \quad \text{and} \tag{3.25}$$

Case D: surface equivalent bubble diameter assuming a ellipsoidal bubble shape

$$f(d_0^D) = \sum_i f(d_{b,i}) \,, \tag{3.26}$$

whereas f is the interfacial area density according to eq. (3.17).

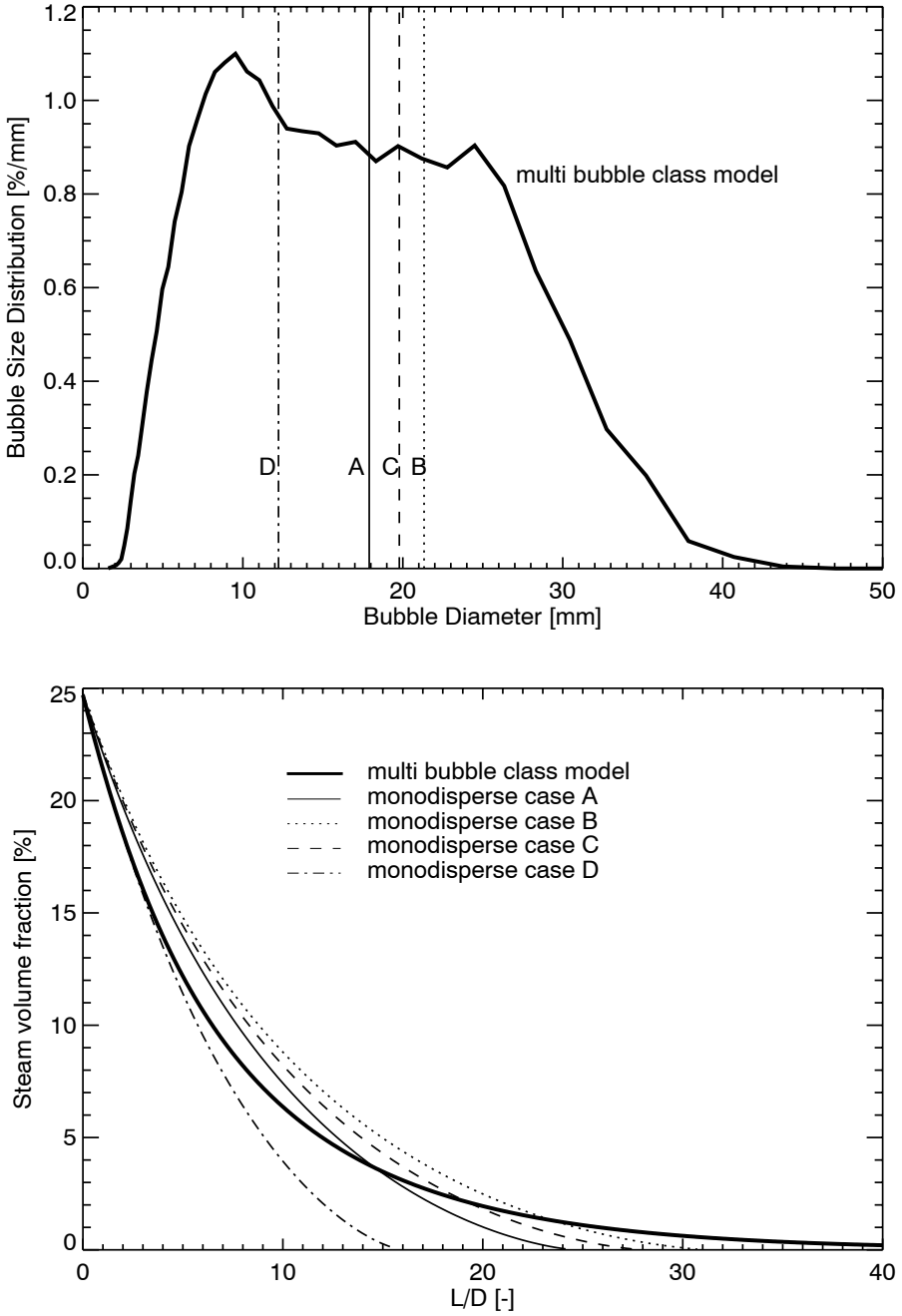

Fig. 3.30 a) Initial bubble size distribution and initial bubble diameter used for the comparison between the multi bubble size model and the modelling considering only one bubble size group. b) Evolution of the cross section averaged steam volume fraction using the multi bubble size model compared with results from simulations considering only one bubble size group.

The qualitative deviations are the same for cases A – C. For low L/D the calculated condensation rates are lower in the case of the mono-disperse approaches. This is caused by the non-reflected high condensation rates of small bubbles (i.e. parts with large interfacial area density). In contrast for large L/D the condensation rates are overestimated, since the large bubble are not represented. At the point, where the steam volume fraction becomes zero, a bubble diameter equal to zero is achieved,

i.e. all bubbles vanish at the same time (or L/D). For the multi bubble size class approach the small bubbles vanish during the whole simulation. In case D the initial condensation are same as for the multi bubble size class approach, since the interfacial area is equal. In the result, the calculation reproduced the slope of the void fraction decrease well for small L/D. The initial bubble diameter is much lower compared to cases A – C, that causes the condensation process to complete much earlier, i.e. at much lower L/D.

3.5.2 Comparison with the experiment

In the next step the multi bubble size class model was used to simulate the experimentally observed condensation process. In these experiments the measuring plane was always at the upper end of the pipe, but the level of the gas injection was varied (see Technical Report “Experiments on upwards gas-liquid flow in vertical pipes”). The initial bubble size distribution, radial gas fraction profile and total gas volume fraction for the simulation were taken according the data measured close to the gas injection (L/D=1.1 for injection via 1 mm holes, L/D=1.4 for injection via 4 mm holes). It has to be kept in mind that measured bubble sizes represent the diameter of the circle equivalent to the maximum area of the measuring plane covered by the bubble during its passage through the sensor. For the input into the model, volume equivalent bubble sizes are needed. The use of the measured distributions as a boundary condition is therefore a compromise that has to be taken, since other data is not available.

The initial liquid temperature was set to the measured values. The pressure was set to the nominal pressure in the steam drum plus the overpressure generated by partially closing the ball valve. In addition the growing hydrostatic pressure and the resulting decrease of the saturation temperature with decreasing height in the vertical pipe is considered in the simulation. The development of the flow was calculated for the available distances between the gas injection and the wire-mesh sensor. The result of the wire-mesh measurements at the levels L/D = 1.1 or, respectively, 1.4 were used as input boundary conditions to calculate the total steam volume fraction, radial steam volume fraction profiles and bubble size distributions for the rest of the measuring positions ($2.5 \leq L/D \leq 40$). Separate calculations for each distance were necessary because of the different initial pressure values according to the different height positions of the gas injection.

Fig. 3.31 compares the evolution of the cross section averaged steam volume fraction over the pipe length for each individual calculation with experimental data. The single calculations for the different L/D are similar, but some small differences occur caused by the different initial pressure values. The calculations are good agreement with experimental data. The effect of the initial bubble size caused by the different diameter of the injection orifices is clearly reproduced in the simulations. The calculated and measured bubble size distributions for the same case are compared in Fig. 3.32. The measured distributions at L/D = 1.1 and 1.4 were taken as input for the simulation respectively. The evolution of the bubble size distribution is in general in good agreement with the experimental findings. Nevertheless some deviations occur. They are presumably caused by weaknesses of the bubble breakup model. This was found in earlier air-water experiments, too, where the models of bubble

coalescence and breakup lead to deviations from experimental data (see Lucas et al. 2007b).

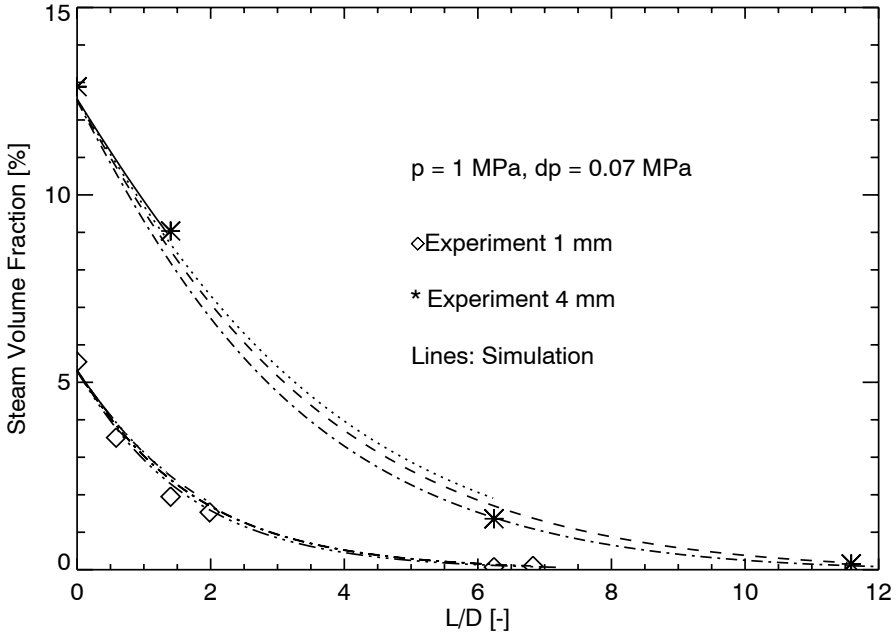

Fig. 3.31 Comparison of the calculated evolution of the cross section averaged steam volume fraction with experimental results. The different lines results from the separate calculations conducted for the different L/D measured.

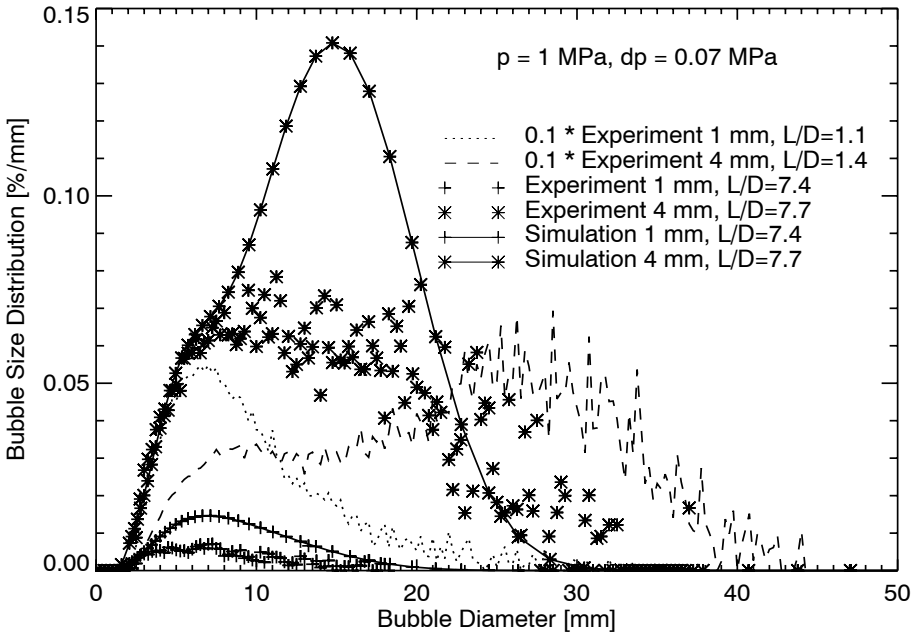

Fig. 3.32 Comparison of the calculated and measured bubble size distributions. The measured distributions at L/D = 1.1 and 1.4 were taken as input for the simulation respectively.

In some other cases the calculated decrease of the steam volume fraction with L/D is less pronounced compared to the experiment, i.e. the calculated condensation rates are to small, e.g. for the 1 mm injection at p = 2 MPa and Δp = 0.16 MPa as shown in Fig. 3.33. In this figure only the values calculated for the measured L/D are shown. Possible reasons of the deviations are uncertainties in the interfacial area and the questionable validity of the Hughmark correlation for the heat transfer coefficient in case of very large bubbles (initial bubble sizes are up to 60 mm equivalent bubble diameter).

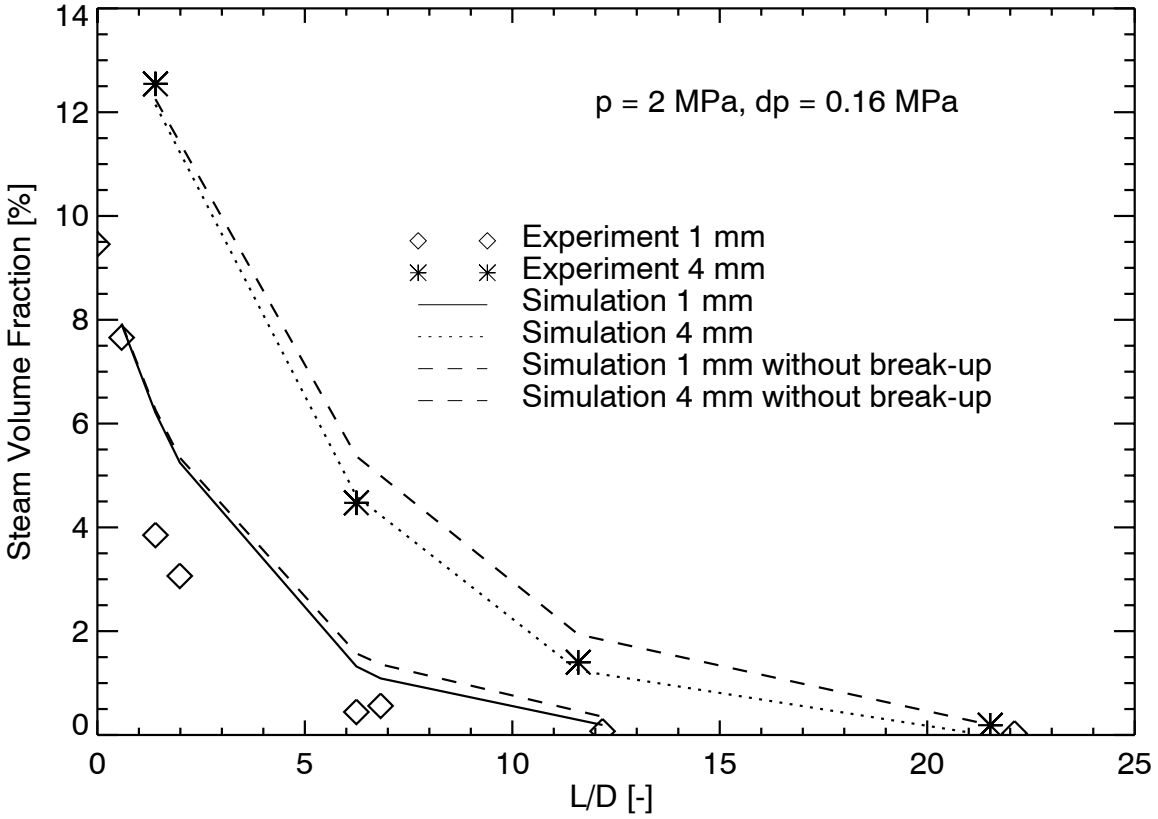

Fig. 3.33 Comparison of the calculated evolution of the cross section averaged steam volume fraction (with and without consideration of breakup) with experimental results

Test calculations where the assumption of the absence of a radial heat transport in the liquid was replaced by an ideal radial mixing did not result in significantly different results, which means that radial heat transport in the liquid is of less importance. On the other hand, the breakup of the initially generated large bubbles enhances the condensation process, because the interfacial area concentration is increased. Fig. 3.34 compares the results from calculations with and without bubble coalescence and bubble breakup (bubble breakup is clearly the dominant process for these experimental runs – see Technical Report “Experiments on upwards gas-liquid flow in vertical pipes”). For the 4 mm steam injection a good agreement between calculated and measured cross section averaged steam volume fraction is achieved for the case with breakup, while moderate deviations occur in case of neglected breakup. Although the breakup model does not exactly reproduce the shape of the bubble size distribution, Fig. 3.34 demonstrates that this distribution is important for the correct prediction of the condensation process.

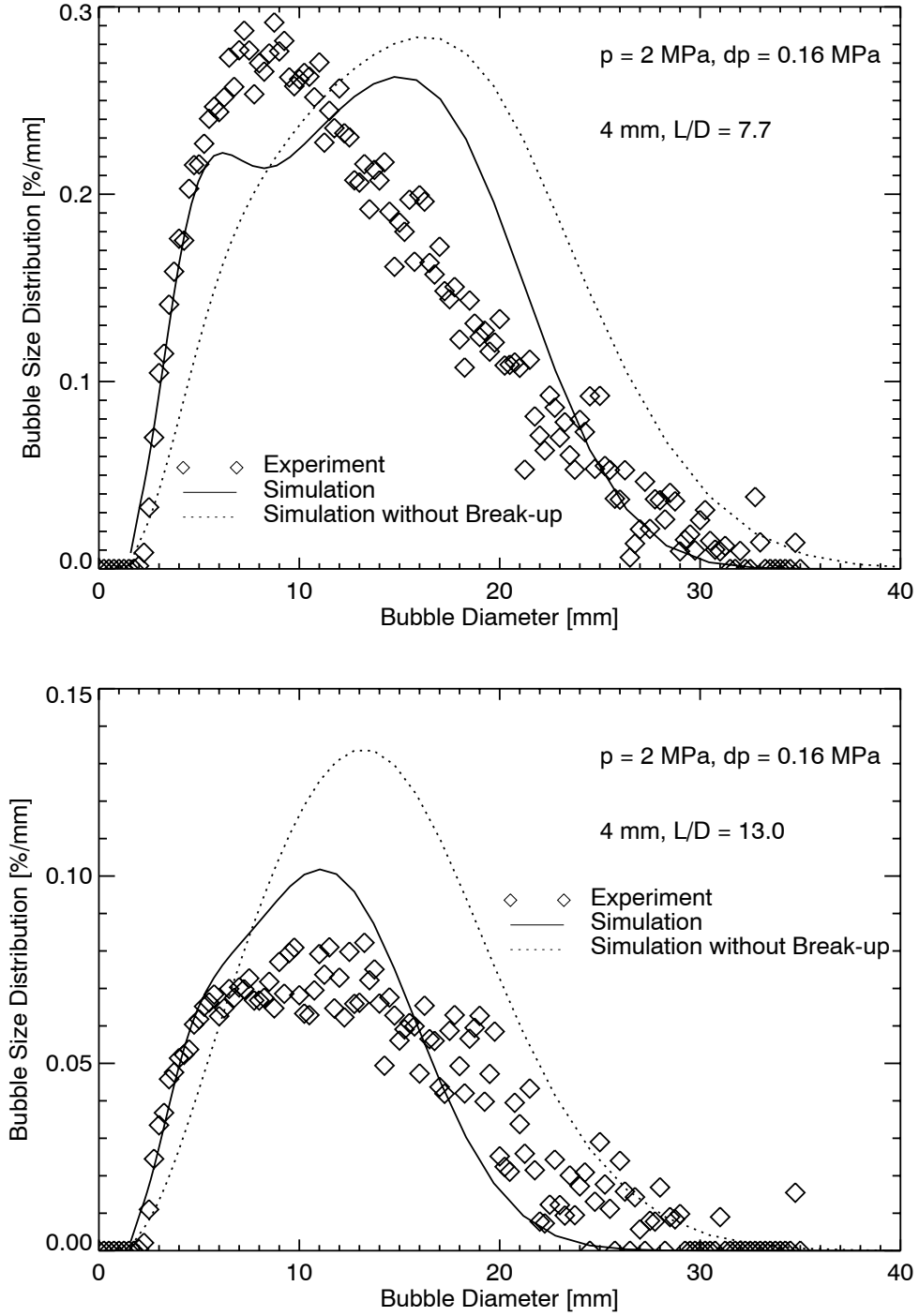

Fig. 3.34 Comparison of the calculated and measured bubble size distributions for 2 different L/D.

The simulations demonstrate the necessity for a multi bubble class model to reproduce the interfacial area and the connected local mass transfer rates in a proper way. Depending on the initial bubble size there are clear differences in the speed of the condensation process. Bubble breakup also increases the interfacial area and thus accelerates condensation. Some uncertainties arise from the contribution of large bubbles to interfacial area as well as from the choice of the heat transfer

models, which will be subject of future work. For this also new experiments with improved definition of boundary conditions are needed.

3.6 Conclusions for the CFD model development

The investigations done with the Multi Bubble Size Class Test Solver demonstrate that there is a strong feedback between bubble sizes and local bubble distributions. In accordance with the experimental observations the local separation between small and large bubbles can be reproduced with an approach, which considers a number of bubble size groups. If simulations are done considering only one averaged bubble size, these effects are neglected. On the other hand the local distributions determine the local coalescence and breakup rates. For this reason the development of bubbly flows and especially transient bubbly flows are determined by such effects. In case of phase transfer also the transfer rates depend on the local interfacial area density. It is determined by local bubble density as well as bubble sizes.

The evolution of a bubbly flow is determined by bubbles size dependent bubble forces and bubble coalescence and breakup. A complete set of bubble forces including drag, virtual mass, lift, wall (deformation) and turbulent dispersion forces has to be considered. Despite some open questions for high liquid volume flow rates and regarding some transient effects as discussed above to suggested models seem to have a certain extent of generality. More difficult is the modeling of bubble coalescence and breakup. Up to now no models is available, which can be applied over a wide range of parameters. One reason maybe also lie in the shortcomings of the turbulence modeling for two-phase flows. Both coalescence and breakup strongly depend on the dissipation rate of turbulent energy. Usually in CFD codes the Sato model is applied to modify the turbulent viscosity for the additional turbulence generated by the bubbles. This improves the resulting velocity fields, but may lead to completely wrong values for the turbulent kinetic energy and the dissipation rate of the turbulent kinetic energy. Here improvements of the presently available models are required.

Because of the above mentioned dependence of the evolution of the flow on the bubble size distribution it is necessary to consider it for the simulation of poly-dispersed bubbly flows (and bubbly flows are poly-dispersed in most practical applications!) using CFD codes. Beside a consideration in the mass balance also a number of bubble size groups have to be considered in the momentum balance to simulate the above mentioned local separation of bubbles of different size.

This was done for the CFD code CFX by an extension of the MUSIG model by Lo to a so-called N*M MUSIG model. The details are discussed in chapter 4 of this report. In the presently implemented basis version of the code a mass transfer between the bubble classes can occur only from bubble coalescence and breakup. In case of flows with local or temporal changes of pressure as well as for flows with evaporation or condensation additional source and sink terms have to be included for the mass balance of the single bubble classes. Such extensions of the N*M MUSIG models are planned.

4. Extension of the MUSIG Model in CFX

4.1 The MUSIG model by Lo

For larger gas volume fractions, several bubble size classes that include the exchange of mass caused by bubble coalescence and breakup phenomena have to be considered. In principle, the two fluid approach described above can be extended to simulate a continuous liquid phase and several gaseous dispersed phases solving the complete set of balance equations for each phase. The investigations using the test solver described in chapter 3 however showed that for an adequate description of the gas volume fraction profile including a population balance model decades of bubble size classes would be necessary. In a CFD code, such a procedure is limited by the increased computational effort to obtain converged flow solutions.

To solve this problem, the multiple size group model implemented by the code developer in CFX-4 solves only one common momentum equation for all bubble size classes (homogeneous MUSIG model, see Lo 1996, 2000a, 2000b). Mathematically, the Multiple Size Group model MUSIG is based on the population balance method and the two-fluid modelling approach. The dispersed phase is divided into M size fractions. The population balance equation is applied to describe the mass conservation of the size fractions taking into account of the inter-fraction mass transfer resulting from bubble coalescence and breakup. This model approach allows a sufficient number of fraction size groups required for the coalescence and breakup calculation to be used and has found a number of successful applications to large-scale industrial multiphase flow problems.

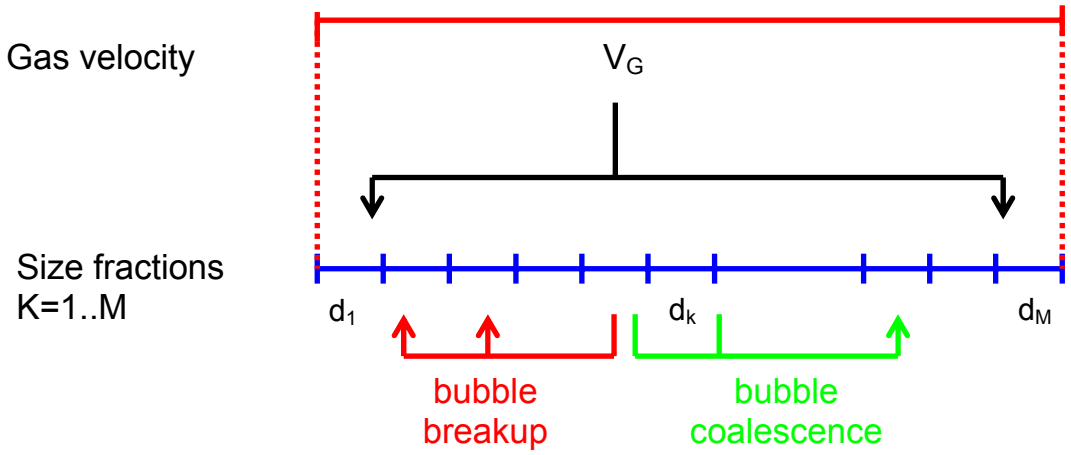

Fig. 4.1 Schema of the standard MUSIG model: All size fractions representing different bubble sizes moves in the same velocity field

Nevertheless, the assumption also restricts its applicability to homogeneous dispersed flows where the slip velocity of particles are approximately independent of particle size and the particle relaxation time is sufficiently small relative to inertial time scales. Thus, the asymptotic slip velocity can be considered to be attained almost instantaneously. The homogeneous MUSIG model described above fails to predict the correct phase distribution when heterogeneous particle motion becomes important. One example is the bubbly flow in vertical pipes where the non-drag forces play an essential role on the bubble motion. In chapter 2.1.3 the lift force was

described to change its sign, when applied for large deformed bubbles, which are dominated by the asymmetrical wake. The lift force in this case has a direction opposite to the shear induced lift force on a small bubble. For this reason, large bubbles tend to move to the pipe core region resulting in a core void maximum whereas a wall void peak is measured for small bubbles. The radial separation of small and large bubbles, which was shown to be very essential for the establishment of the flow pattern (see chapter 2.3) cannot be predicted by the homogeneous MUSIG model.

4.2 New strategies – the inhomgeneous MUSIG model

A combination of the consideration of different dispersed phases and the algebraic multiple size group model was proposed to combine both the adequate number of bubble size classes for the simulation of coalescence and breakup and a limited number of dispersed gaseous phases to limit the computational effort (see Shi et al. 2003, Krepper et al. 2005). The inhomogeneous MUSIG model was developed in cooperation with ANSYS CFX and is implemented in CFX-10 (Shi et al. 2004, 2005, Zwart et al. 2003, Frank et al. 2005).

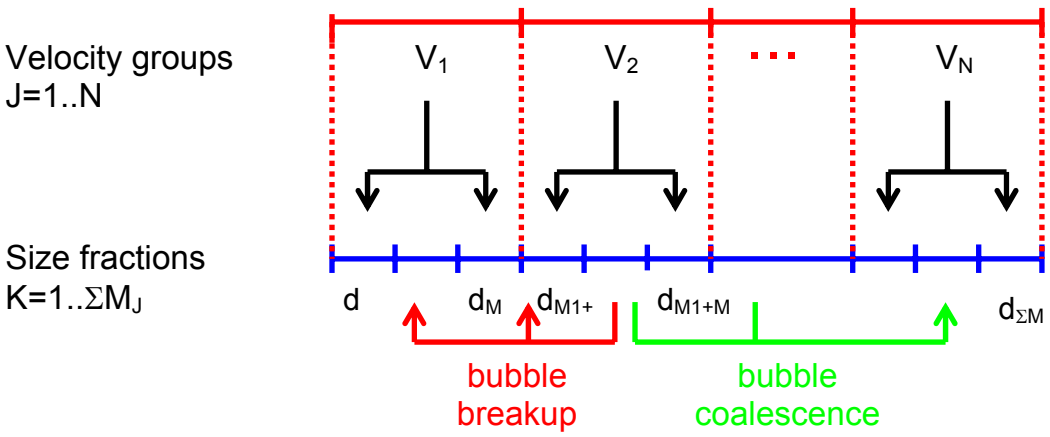

Fig. 4.2 Improvement of the polydispersed approach: The size fractions M_j are assigned to the velocity field *Vj*

In the inhomogeneous MUSIG model the gaseous disperse phase is divided into a number N so-called velocity groups (or phases), where each of the velocity groups is characterized by its own velocity field. Further, the overall bubble size distribution is represented by dividing the bubble diameter range within each of the velocity groups j in a number Mj j=1..N bubble sub-size fractions. The population balance model considering bubble coalescence or bubble breakup is applied to the sub-size groups (see Fig. 4.2). Hence the mass exchange between the sub-size groups proceeds independent on the boundaries of the velocity groups.

The lower and upper boundaries of bubble diameter intervals for the bubble size fractions can be controlled by either an equal bubble diameter distribution, an equal bubble mass distribution or can be based on user definition of the bubble diameter ranges for each distinct bubble diameter fraction. The subdivision should be based on the physics of bubble motion for bubbles of different size, e.g. different behaviour of differently sized bubbles with respect to lift force or turbulent dispersion. Therefore, it can be suggested that in most cases N=2 or 3 velocity groups should be sufficient

in order to capture the main phenomena in bubbly or slug flows. The investigation of the number of velocity groups necessary for the adequate simulation of the flow is subject of chapter 6.1.

The continuum equation for the gaseous dispersed phase j can be written as:

$$\frac{\partial}{\partial t}\left(\alpha_j \rho_g\right)+\nabla\cdot\left(\alpha_j \rho_g \vec{U}_j\right)=S_j \tag{4.1}$$

the momentum equations for the gaseous phases *j* has the form:

$$\begin{aligned}&\frac{\partial}{\partial t}\left(\alpha_j \rho_g \vec{U}_j\right)+\nabla\cdot\left(\alpha_j \rho_g \vec{U}_j\times\vec{U}_j\right)=\nabla\cdot\left(\alpha_j \mu_g\left(\nabla\vec{U}_j+\left(\nabla\vec{U}_j\right)^T\right)\right)\\&-\alpha_j\nabla p+\alpha_j\rho_g\vec{g}+\vec{M}_j+\vec{S}_{Mj}\end{aligned} \tag{4.2}$$

with

$$\vec{F}_j=\vec{F}_{j,D}+\vec{F}_{j,L}+\vec{F}_{j,W}+\vec{F}_{j,TD} \tag{4.3}$$

where α_j, ρ_g, μ_g are the void fraction, density and viscosity of the gas and $\vec{F}_j$ represents the sum of interfacial forces like the drag force $F_{j,D}$, lift force $F_{j,L}$, wall lubrication force $F_{j,W}$ and turbulent dispersion force $F_{j,TD}$. $\vec{S}_{Mj}$ represents the transfer of gaseous phase momentum between different velocity groups due to bubble breakup and coalescence processes leading to bubbles of certain size belonging to a different velocity group.

Additional for each sub-size fraction *i* (*i*=1..M_j) in the velocity group *j* $f_i\alpha_j$ the continuum equation has to be solved:

$$\frac{\partial}{\partial t}\left(f_i\alpha_j \rho_g\right)+\nabla\cdot\left(f_i\alpha_j \rho_g \vec{U}_j\right)=S_{ij} \tag{4.4}$$

The source terms, S_{ij}, represent the local transfer of gaseous phase mass due to bubble breakup and coalescence processes. They can be assigned to S_k, which are the elements of the population balance model. Note that the above equations the index *j* extends over the range *1..N* and the index *k* over the range 1.. $\sum_{j=1}^{N} M_j$. The population balance equations have then the form:

$$S_k=B_{k,B}-D_{kB}+B_{kC}-D_{kC} \tag{4.5}$$

where $B_{k,B}$ is the bubble birth rate due to breakup of larger bubbles, $D_{k,B}$ is the bubble death rate due to breakup of bubbles from size group *k* into smaller bubbles, $B_{k,C}$ is the bubble birth rate into size group *k* due to coalescence of smaller bubbles to bubbles belonging to size group *k* and finally $D_{k,C}$ is the bubble death rate due to coalescence of bubbles from size group *k* with other bubbles to even larger ones. The inhomogeneous MUSIG model approach does not presume a certain coalescence or breakup model. As an example the validation calculations presented in the chapter 6 and 7 were performed applying the breakup model of Luo and Svendsen (1996) and the bubble coalescence model of Prince and Blanch (1990).

5. Validation for vertical pipe flow with lower gas fraction

5.1 Model options

The extensive investigations of upward bubbly flow performed in FZ Dresden-Rossendorf applying a wire mesh sensor at different distances from the gas injection were used to validate the CFD models described in the previous chapters. In the experiments cross sectional gas volume fraction distributions and bubble size distributions were measured. The measurements at the facility MT-Loop performed in the years 2000 to 2003 used a pipe diameter of 51.3 mm and a pipe length of 3.3 m (see e.g. Lucas et al. 2005a). Since 2002, the facility TOPFLOW has also been available. Experiments in tubes having a diameter up to 195.3 mm and a pipe length up to 8 m were performed (see e.g. Prasser et al. 2003b).

Table 5.1 lists the parameters of the presented experiments. Whereas simulations for the tests 017 to 041 were conducted for the 51.3 mm tube of MT-Loop, the other tests refer to experiments at the 195.3 mm tube at TOPFLOW. Simulations for test 118 were done for both facilities.

Tab. 5.1 Water and gas superficial velocities J_L and J_G of the investigated tests

		J_G [m/s]					
		0.0040	**0.0096**	**0.0368**	**0.0898**	**0.140**	**0.219**
J_L [m/s]	**1.611**				097		
	1.017	019	041	074	096	107	118
	0.405	017	039				

The Euler/Euler approach was used to define the multiphase interactions and a Shear Stress Turbulence model (Menter 1994) was applied to the liquid water phase. The turbulence modulation by bubbles increasing the turbulent viscosity according to Sato (1975, 1981) was considered. The phase drag was simulated according to Grace (1976). For the lift bubble force the approach of Tomiyama (1995, 1998) considering the dependency on the bubble size was simulated. The wall force considered was also based on the studies of Tomiyama.

The tube was simulated as a 60° sector where the side faces were defined as symmetry boundary conditions. The inlet profiles for the water flow from below were set for the velocity, the turbulent kinetic energy and the turbulent dissipation. These values were determined by additional calculations simulating single phase flow. So at the inlet the conditions for a fully developed single phase flow were set. The gas injection was modelled by point sources, representing the inlet nozzles of the test facility. For the outlet at the upper part a pressure boundary condition was defined. During a grid refinement study the independence of the numerical solution on the grid was proven.

For the tests 017, 019, 039 und 041 (see Tab. 5.1) a low gas volume fraction is found which can be simulated by only one dispersed gas phase having a certain bubble size diameter. The results are presented in chapter 5.2. The validation on the basis of the profiles of fully developed flow enables the tests of the relation of the non drag bubble forces. The correct simulation of the absolute value is checked considering the smoothing out of the inlet profiles in chapter 5.3 and investigating the flow in

slightly inclined tubes in chapter 5.4. In the test 107 and 18 larger bubbles are found and a bubble class model has to be applied. In chapter 6.1 the application of several dispersed phases modelling test 118 is described. In the chapter 6.2.1 on the example of test 118 the MUSIG approach is demonstrated by simulating additional bubble fragmentation and coalescence. In the chapter 6.2.2 the test 107 performed at TOPFLOW is presented.

5.2 Tests simulating monodispersed flows

For the measurement at the MT-Loop facility a sensor with 24*24 wires was used. For each cross point the local gas volume fraction averaged over the measuring time of 10 seconds was determined. The measurement time is limited by the measuring hardware equipment. The scattering of the measured values in Fig. 5.1 are mainly caused by flow instabilities found particularly at low gas superficial velocities.

Fig. 5.1 shows the comparison of experimental and calculated values (cases 17, 19, 39 and 41) for the upper end of the tube. It could be concluded that the described Euler/Euler approach applying the described models is able to describe bubbly flows at low gas volume fraction with good agreement to measurements.

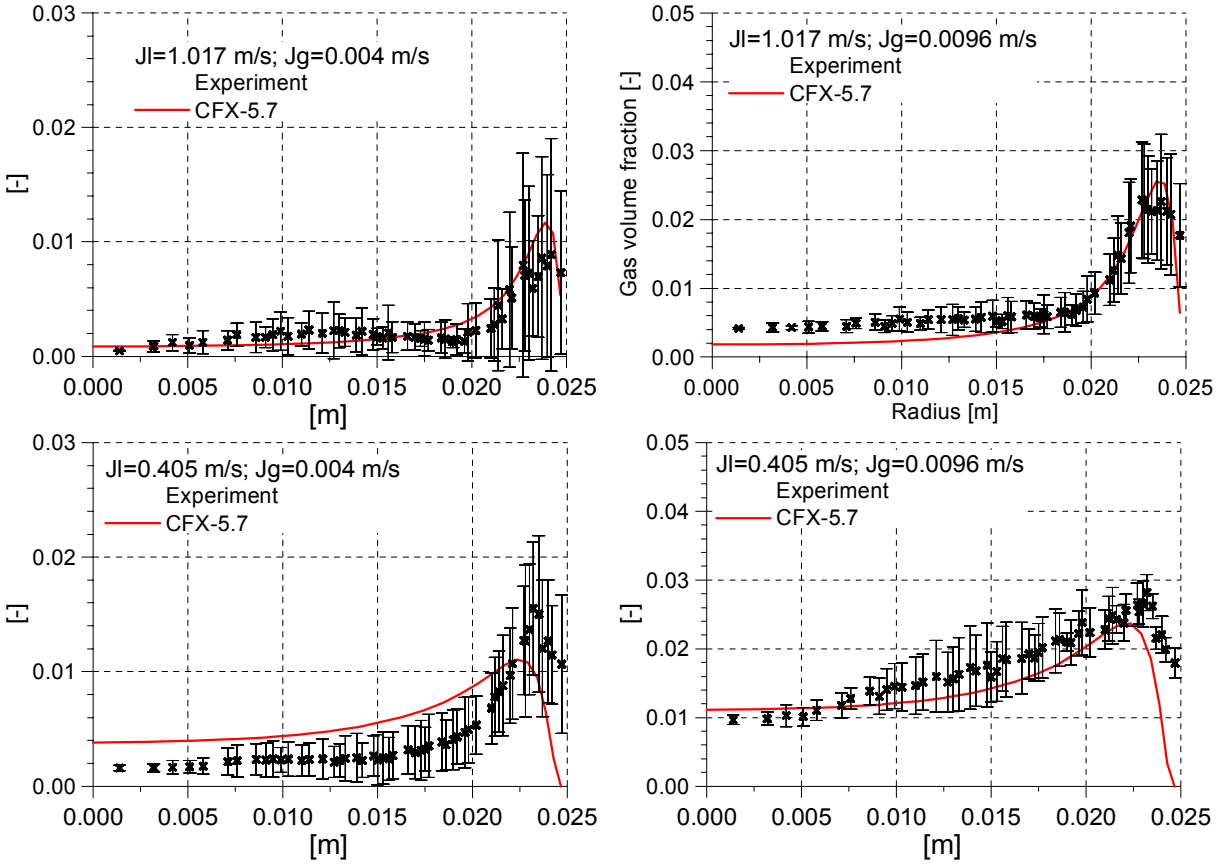

Fig. 5.1 Measured and calculated gas volume fraction distribution for monodispersed bubbly flows

5.3 Comparison of the smoothing out of the injection profile

At the upper end of the pipe it can approximately be assumed, that the flow is fully developed regarding the lateral bubble displacement caused by the non-drag forces. For this reason a comparison of the calculated radial gas volume fraction profiles at the upper end of the pipe with the measured ones can only be used for a validation of the relation between the components of the non drag forces, not for the validation of their absolute value.

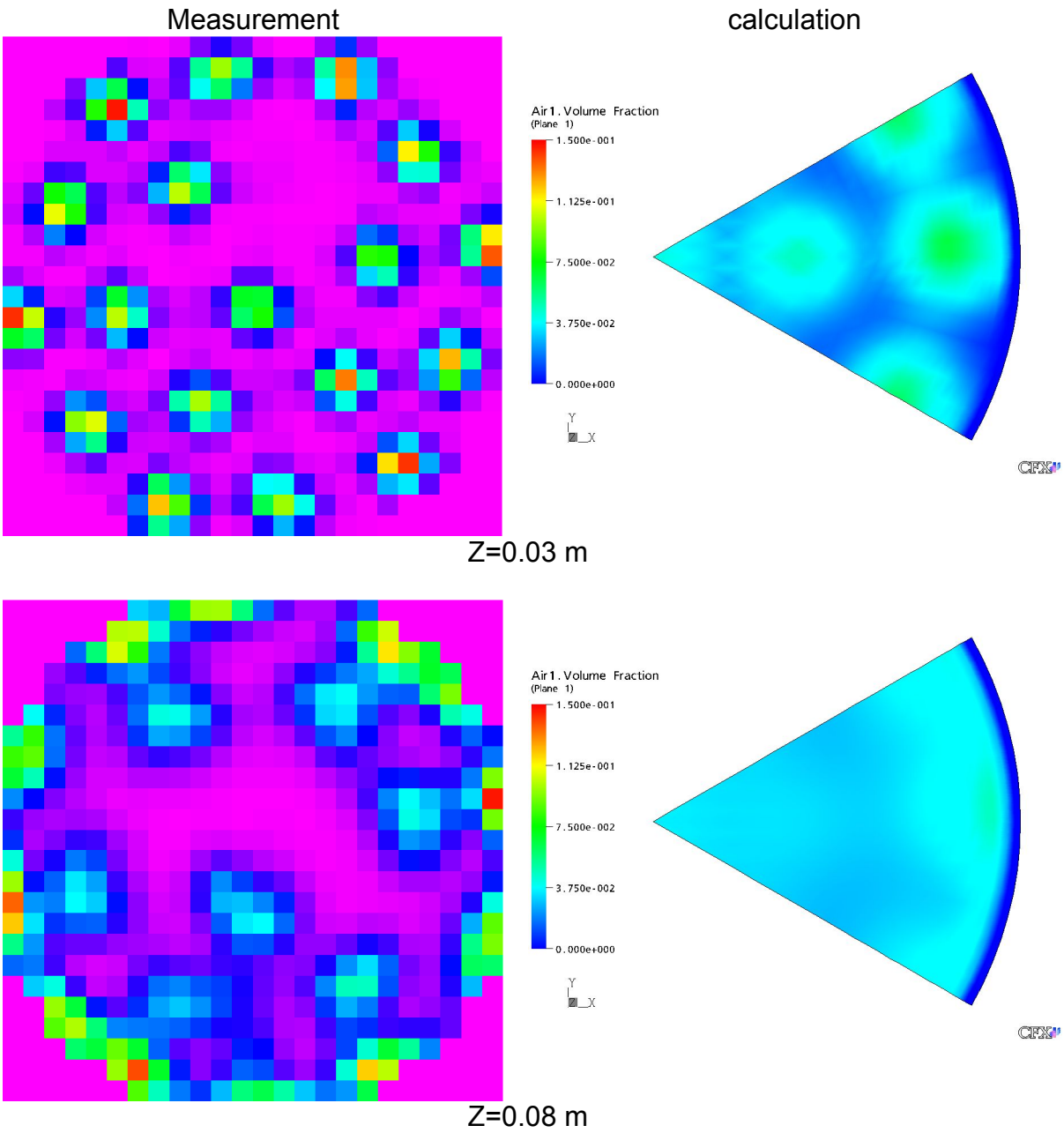

Fig. 5.2a Measured and calculated cross sectional gas volume fraction distribution at different distances Z short after the gas injection (test FZR-074, JL=1.017 m/s, JG=0.0368 m/s)

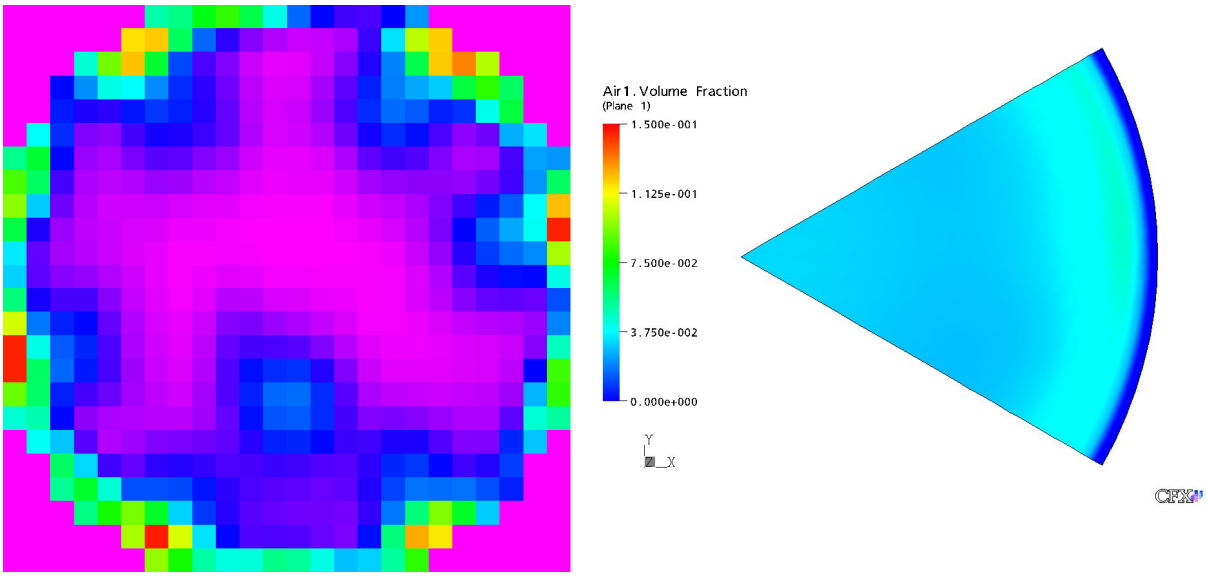

Z=0.13 m

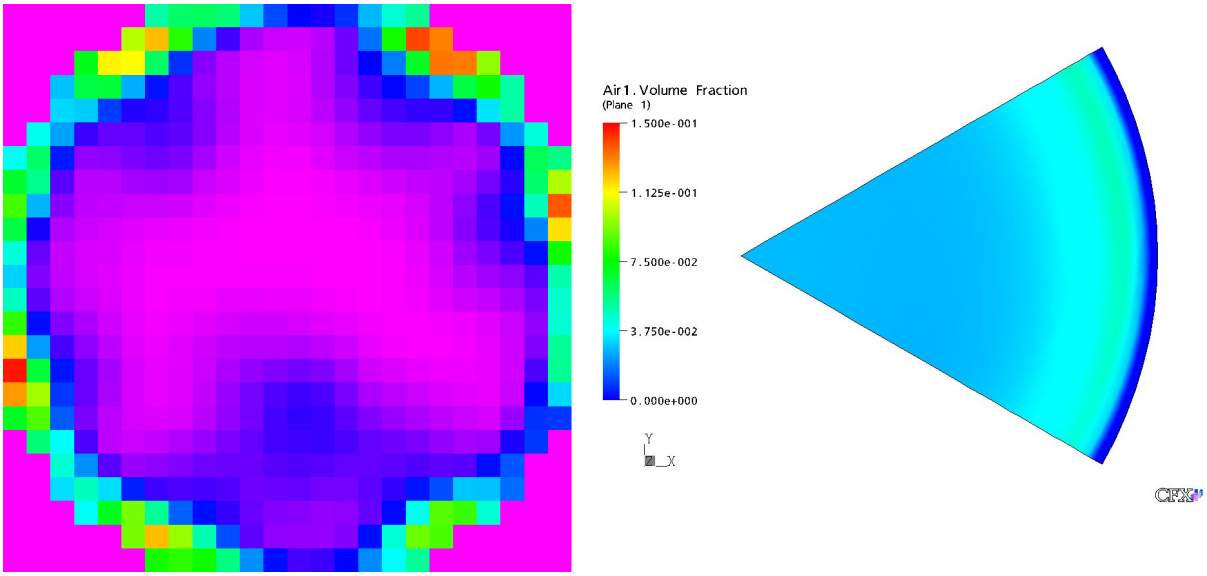

Z=0.23 m

Fig. 5.2b Measured and calculated cross sectional gas volume fraction distribution at different distances Z short after the gas injection (test FZR-074, J_L=1.017 m/s, J_G=0.0368 m/s)

The absolute magnitude of the forces can be assessed by studying the development of the gas distribution along the tube. In the MT_Loop experiments the gas was injected through up to 19 nozzles, which were equally distributed in the injection plane. Closely after the injection the gas distribution caused by the capillaries is found in the wire mesh measurements (see Fig. 5.2, left side). With increasing distance from the gas injection this structure is smoothed out (Fig. 5.2, right side). Whereas Fig. 5.2 shows the cross sectional void fraction distribution, in Fig. 5.3 the radial profiles are presented. In the experiments the profiles are smoothed out after a longer distance (z=0.13..0.23 m) then in the calculations (z=0.08..0.13 m). There are indications that for air/water flow considered here at normal conditions the applied FAD model overestimates turbulence dispersion force mode this force for higher gas volume fractions.

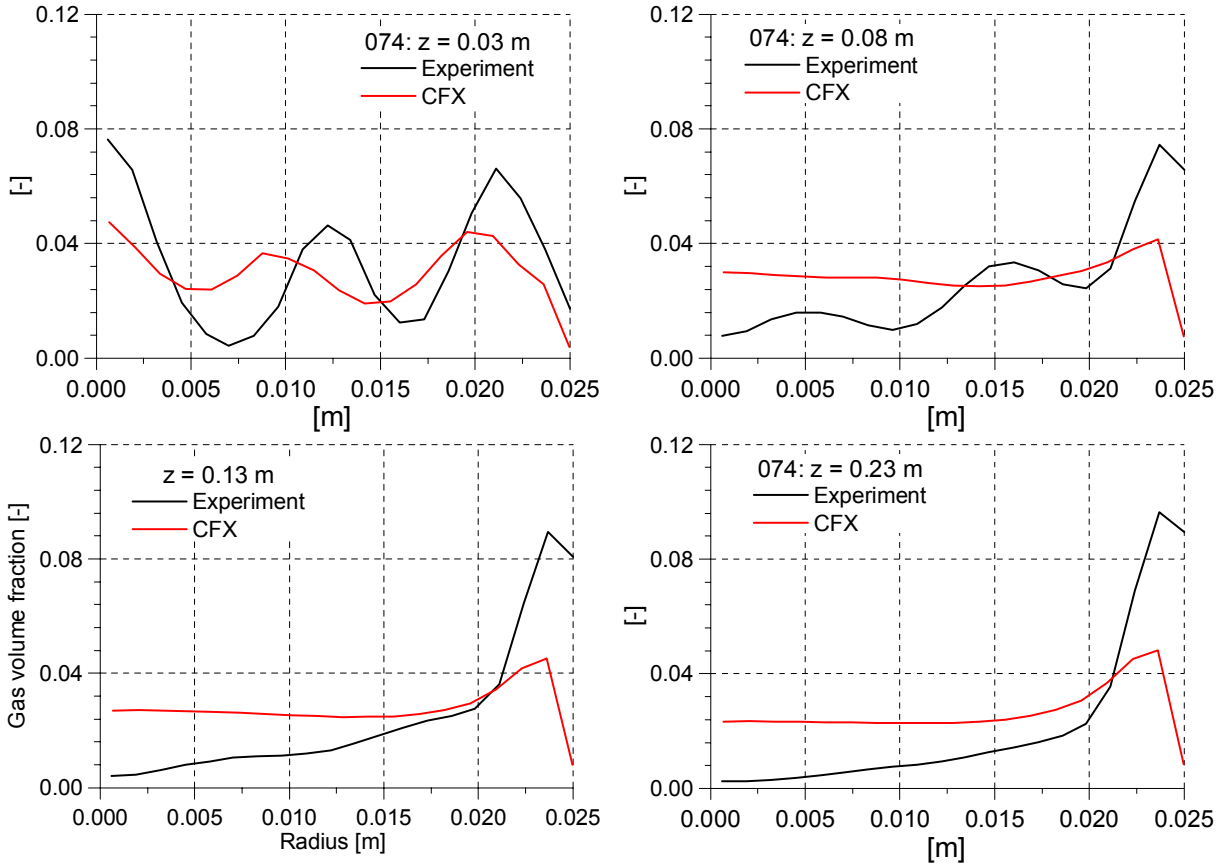

Fig. 5.3 Measured and calculated radial gas volume fraction profiles

5.4 Simulation of a slightly inclined tube

In the MT-Loop tests experiments with slightly disturbed cylindrical symmetry were performed: The tube was slightly inclined. The consequence is a gas accumulation on the opposite of inclination direction (see Prasser et al. 2003a). Inclinations up to 25.61 mm/m and gas superficial velocities J_G=0.006 .. 0.14 m/s at J_L=0.405 m/s were investigated.

Fig. 5.4 and Fig. 5.5 show the measured results for the tests MT-Loop-039 and MT-Loop-050. The tube was inclined in the upper right direction. The radial profiles were determined in this direction. The bubble size distribution was added to show, that despite the higher gas fraction bubble coalescence plays not yet a role and a monodispersed model approach is justified.

A full 3D grid was used for the simulation. Fig. 5.6 shows the cross sectional distribution calculated for the test 050. In Fig. 5.7 measured and calculated gas profiles are compared. To show the influence of the absolute value of the non drag forces an additional result with at 20% reduced non drag forces was added.

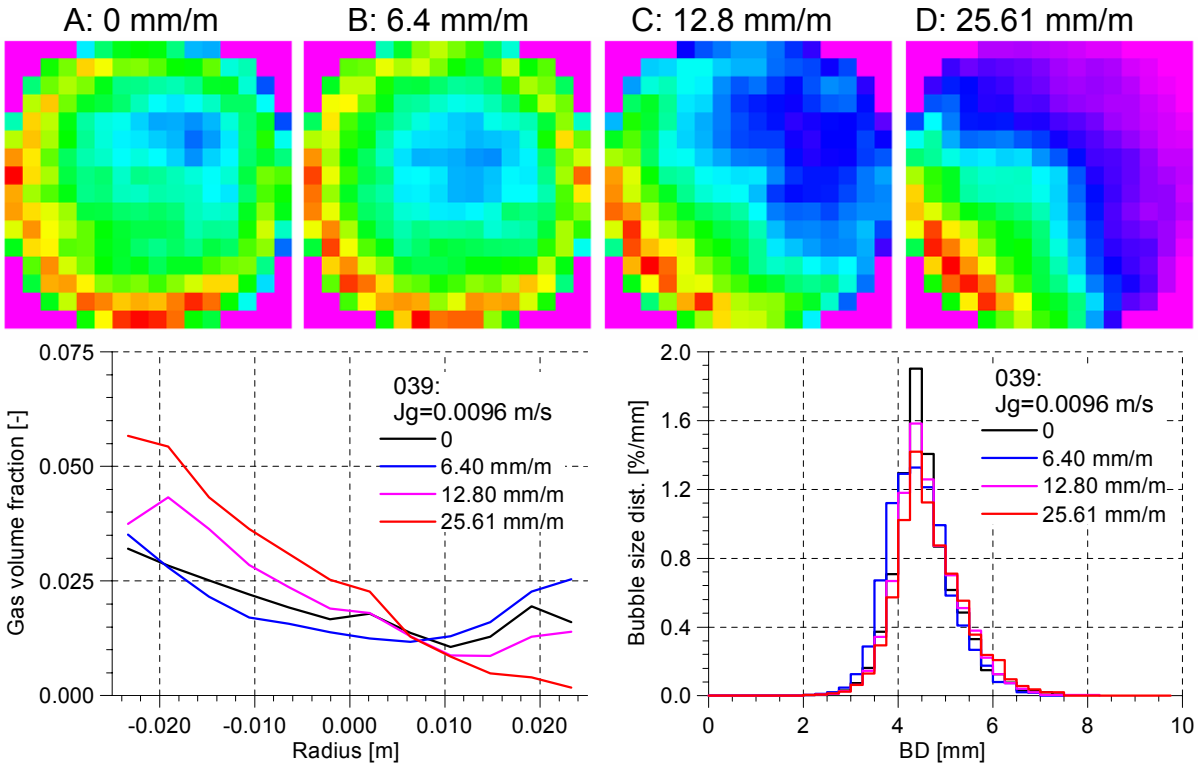

Fig. 5.4 Cross sectional distribution of the air volume fraction, radial profiles and bubble size distributions for the test FZR-039 (J_L=0.405 m/s; J_G=0.0096 m/s)

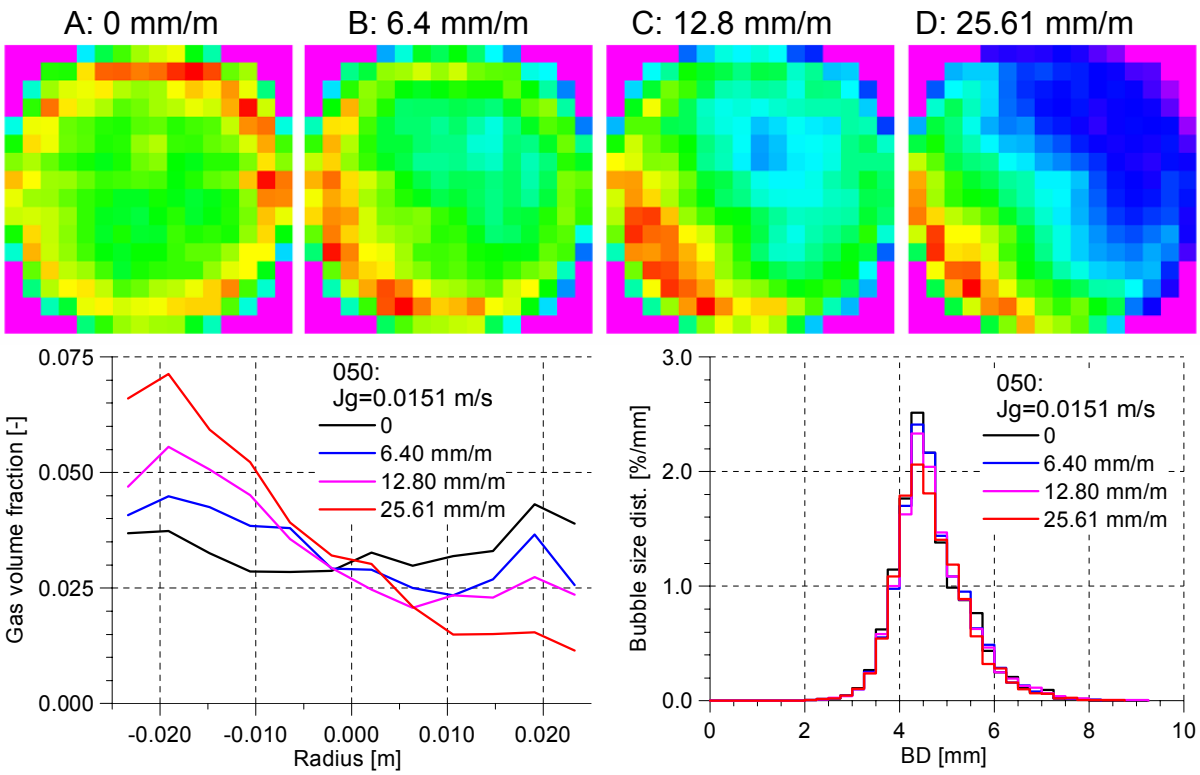

Fig. 5.5 Cross sectional distribution of the air volume fraction, radial profiles and bubble size distributions for the test FZR-050 (J_L=0.405 m/s; J_G=0.0151 m/s)

A full 3D grid was used for the simulation. Fig. 5.6 shows the cross sectional distribution calculated for the test 050. In Fig. 5.7 measured and calculated gas profiles are compared. To show the influence of the absolute value of the non drag forces an additional result with at 20% reduced non drag forces was added.

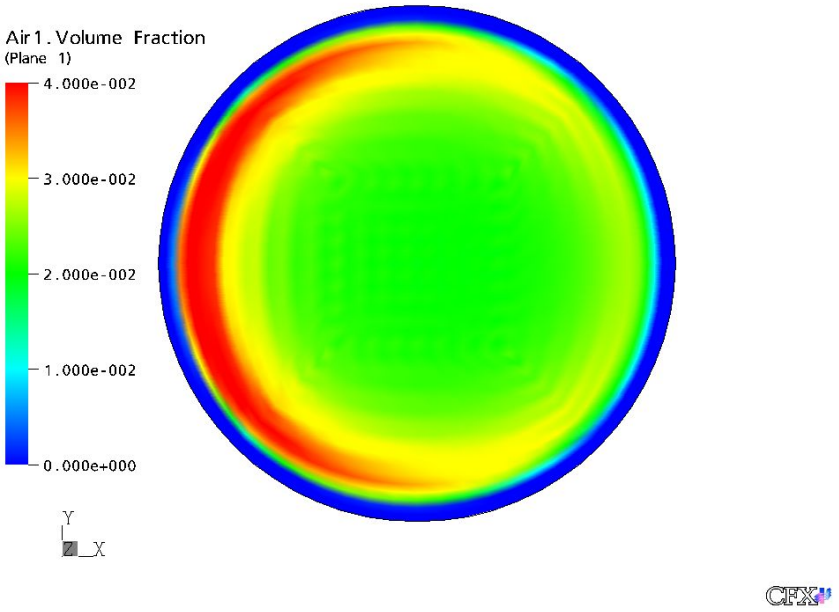

Fig. 5.6 Cross sectional gas volume fraction distribution at 3.00 m for the tests MT-Loop-050 with an inclination D: 25.61 mm/m

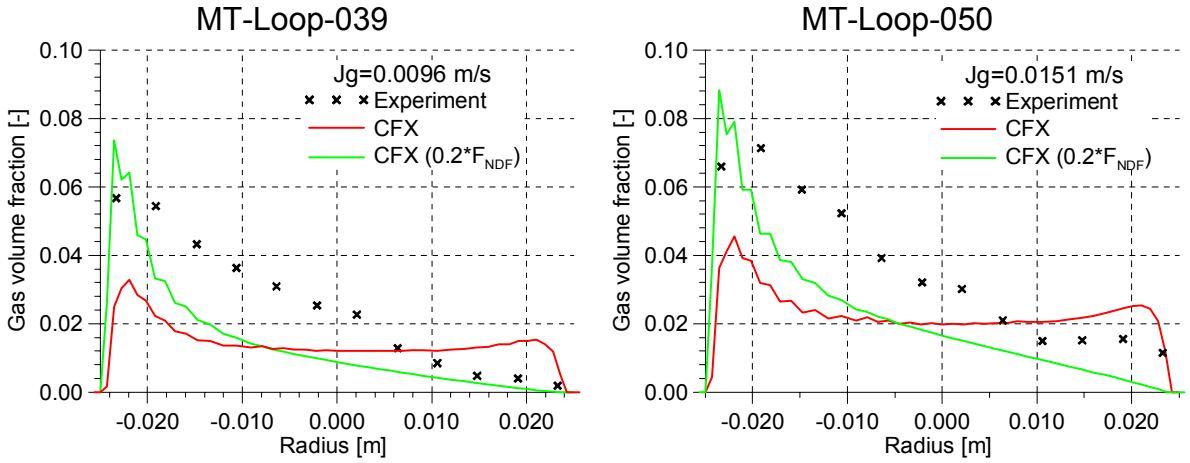

Fig. 5.7 Measured and calculated radial gas profiles at z=3.0 m

The results show that the change of the gas distribution by the tube inclination is underestimated by the calculations. Reducing the simulated non drag forces the solution shifts towards the experimental results. Also these investigations indicate the slightly overestimated non drag forces for air/water flow at normal conditions.

6. Tests with higher gas volume fraction

6.1 Simulation of different dispersed phases

For the test 118 in the MT-loop experiments at the upper end of the tube, a radial gas volume fraction according to Fig. 6.1a and a bubble size distribution according to Fig. 6.1b were found.

To describe a bubbly flow showing a core gas fraction peak according Fig. 6.1a several dispersed phases with each having its own velocity field were simulated. As a first step the mass exchange between the gas phases was excluded. Simulations with 2, 3 and 4 different bubble size classes were performed to investigate the necessary number of dispersed phases for an adequate simulation. According to the measured bubble size distribution at the upper end of the tube (Fig. 6.1 b) the fraction and the averaged bubble size of each bubble size class was determined and given as an inlet condition (see Table 2). The selection of the range boundaries was performed considering the dependency of the lift coefficient on the bubble size. In the simulation only the dependence of the bubble forces on the bubble size – particularly the lift force was considered. The resulting radial gas fraction distributions for the variants are shown in Fig. 6.2.

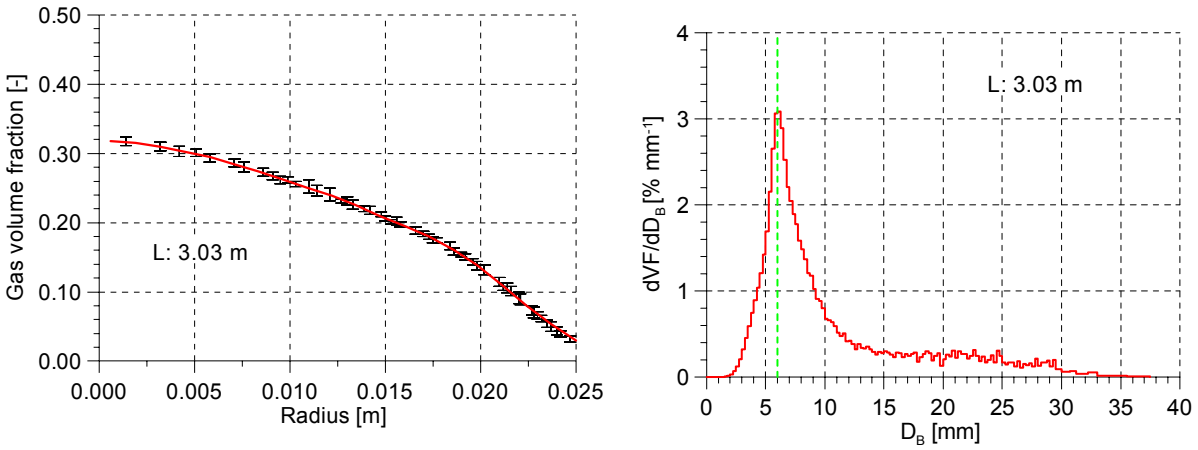

a) radial gas fraction distribution

b) bubble size distribution

Fig. 6.1 Measured radial gas fraction distribution and bubble size distribution for the test 118 (J_L=1.017 m/s, J_G=0.219 m/s)

Tab. 6.1	Parameters of the simulations with several dispersed gas phases				
2 classes	range	0 - 6		> 6	
	av. diameter	4.95		12.55	
	gas fraction	0.04185		0.12358	
3 classes	range	0 – 4.5	4.5 – 7.5		>7.5
	av. diameter	3.76	6.09		15.02
	gas fraction	0.01136	0.06707		0.08698
4 classes	range	0 – 4.5	4.5 - 6	6 – 7.5	>7.5
	av. diameter	3.76	5.39	6.68	15.02
	gas fraction	0.01136	0.03050	0.03661	0.08698

The expected dependencies were observed, i.e. for the classes with small bubbles a wall peak and for bubble size classes with large bubbles a core peak is found. The total values correspond to the measured values. However, according to Fig. 6.2d almost no difference between the investigated three cases was found. The improved physical representation of the bubble classes was negated by the numerical effort increase with increasing number of bubble size classes. The investigations were performed also for the test 107 (J_L=1.017 m/s, J_G=0.14 m/s) with the same results.

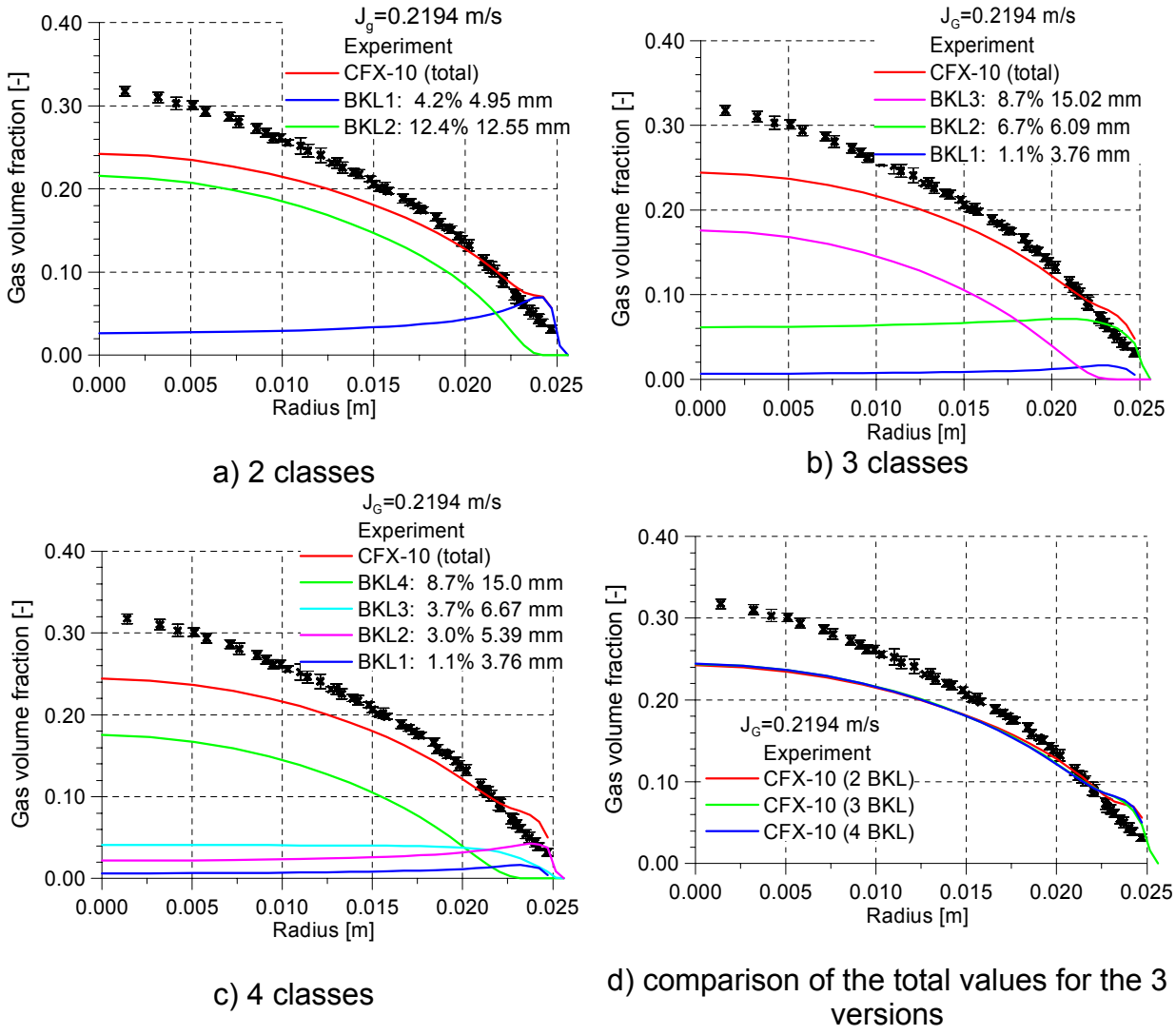

Fig. 6.2 Radial gas fraction profiles for simulation with different dispersed phases

6.2 Tests with higher gas volume fraction - application of the inhomogeneous MUSIG-Modell

In addition to the studies described in chapter 5.3, the current chapter reconsiders the previous case with the inclusion of the mass exchanged by bubble coalescence and fragmentation, i.e. the change of the bubble size distribution was investigated. The bubble size distribution at the inlet was given and adapted to experimental results. The development of the size distribution and of the radial gas profile along the flow was subject of the model studies described in this section here.

6.2.1 Test MT-Loop 118

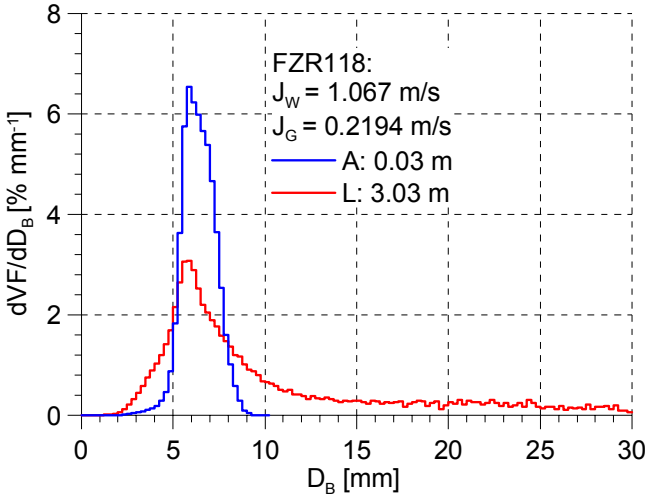

Fig. 6.3 Measured development of the bubble size distribution from the inlet (level A) to the outlet (level L)

Fig. 6.3 shows the measured size distribution at the inlet and the outlet of the tube. In the actual test case the mean Sauter diameter between inlet and outlet remains almost constant, whereas the size distribution is expanded by both coalescence and fragmentation.

Two dispersed phases were simulated. The first phase was further assigned to 12 and the second phase to 22 sub-size MUSIG-groups. Over all 32 groups having a equidistant size step of 0.5 mm were simulated.

The bubble breakup model of Luo and Svendsen (1996) and the bubble coalescence model of Prince and Blanch (1990) were applied. The results indicated that tuning coefficients as dimensionless factors of the mass transfer rates F_B for bubble breakup and F_C for bubble coalescence had to be set to harmonize the mechanisms of fragmentation and coalescence. In Fig. 6.4 different examples for the bubble size distribution and the radial air volume fraction profile are shown. Best agreement to the measurements was found for a breakup coefficient F_B=0.25 and a coalescence coefficient F_C=0.05. All further calculations for air/water in a vertical tube were performed using these same set of coefficients.

Fig. 6.5 presents the development over the tube height of the bubble size distribution and of the radial gas profiles. On the left side in each bubble size distribution also the distribution at the injection is presented (blue). During each measurement run also gas fraction profiles assigned to a certain bubble size region are determined. The radial gas profiles on the right side show also the measured radial gas profiles for d_b<6 mm (blue stars) and d_b>6 mm (green stars) and compares to the calculated profiles of the calculations (solid lines).

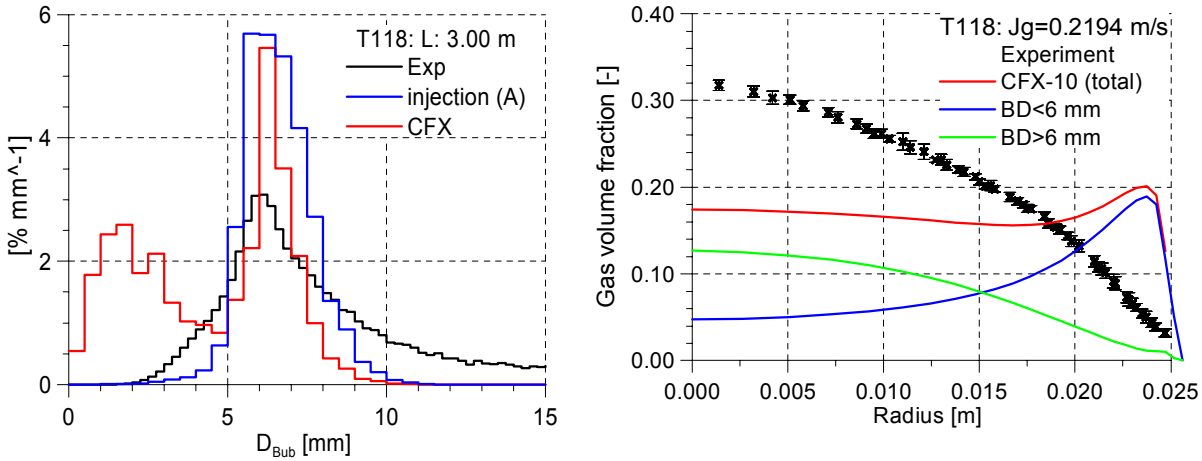

F_B = 1; F_C=0.05

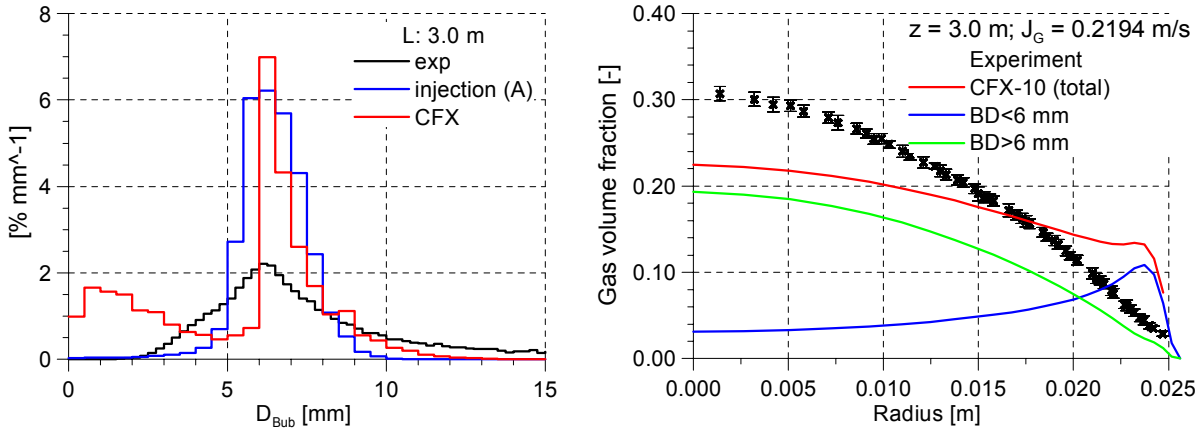

F_B = 1; F_C=0.5

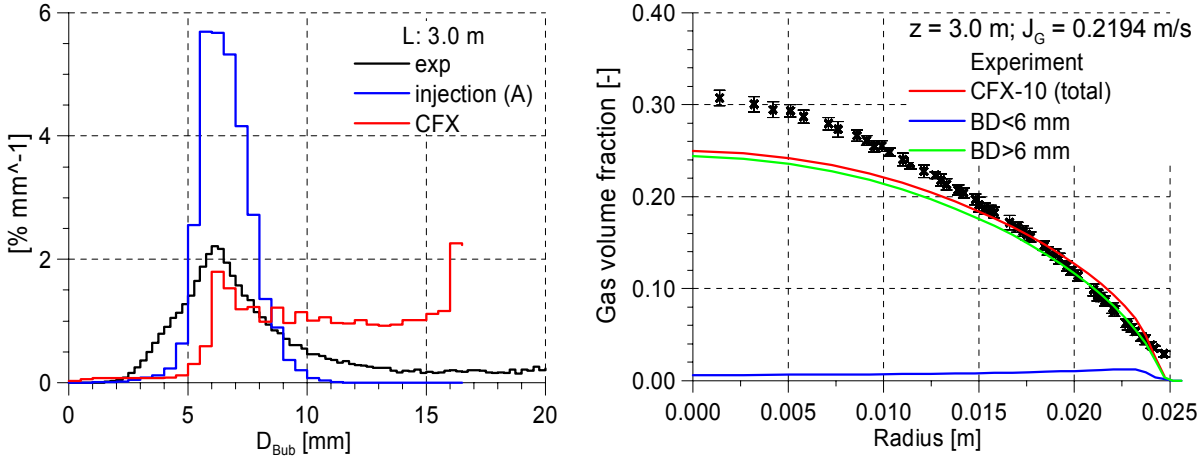

F_B=0.05; F_C=0.5

Fig. 6.4 Bubble size distribution (left side) and radial gas volume fraction profile (right side) at the end of the tube for different coefficients for breakup (F_B) and coalescence (F_C) for the test case MT-Loop-118 (J_L=1.017 m/s; J_G=0.2194 m/s)

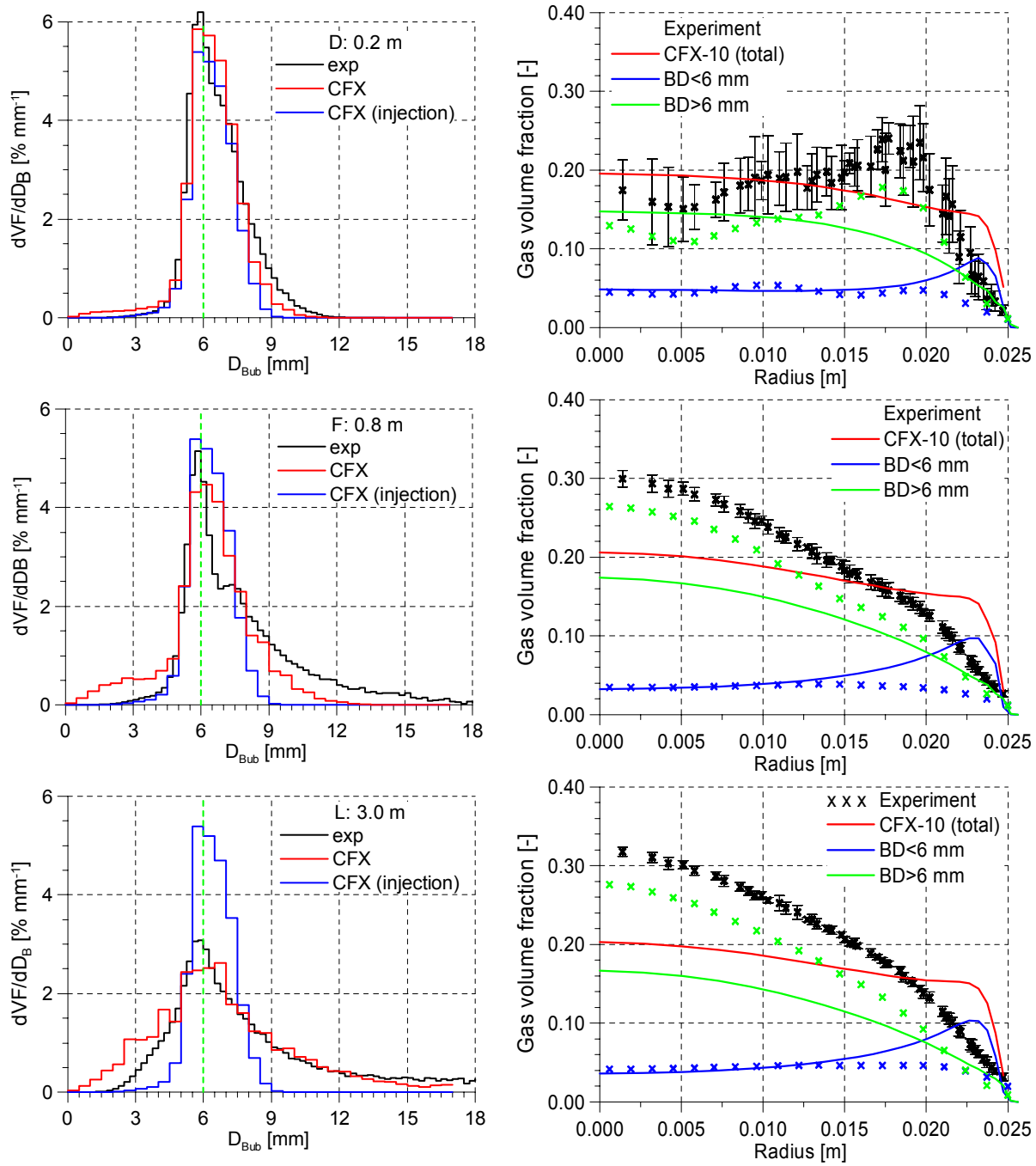

Fig. 6.5 Development of the bubble size distribution (left) and the radial gas fraction profiles (right) of the simulation of the test case MT-Loop 118 (J_L=1.017 m/s; J_G=0.2194 m/s) 2 dispersed phases, 34 MUSIG Groups (F_B=0.25, F_C=0.05)

Fig. 6.6 shows calculated results with the same set of parameters and the same number of 34 MUSIG mass fraction groups but now assigned to 3 instead of 2 dispersed phases. In the Fig. 6.9 the 34 MUSIG mass fraction groups are assigned to 4 dispersed phases. The assignment was performed according to the bubble size regions presented in Tab. 6.1. Also in the last both figures the measured radial volume fraction profiles were decomposed according to the corresponding bubble size region (marked by stars) and compared to the calculated profiles. Criterion for

the comparison was the development of the bubble size distribution and the profile of the total gas volume fraction.

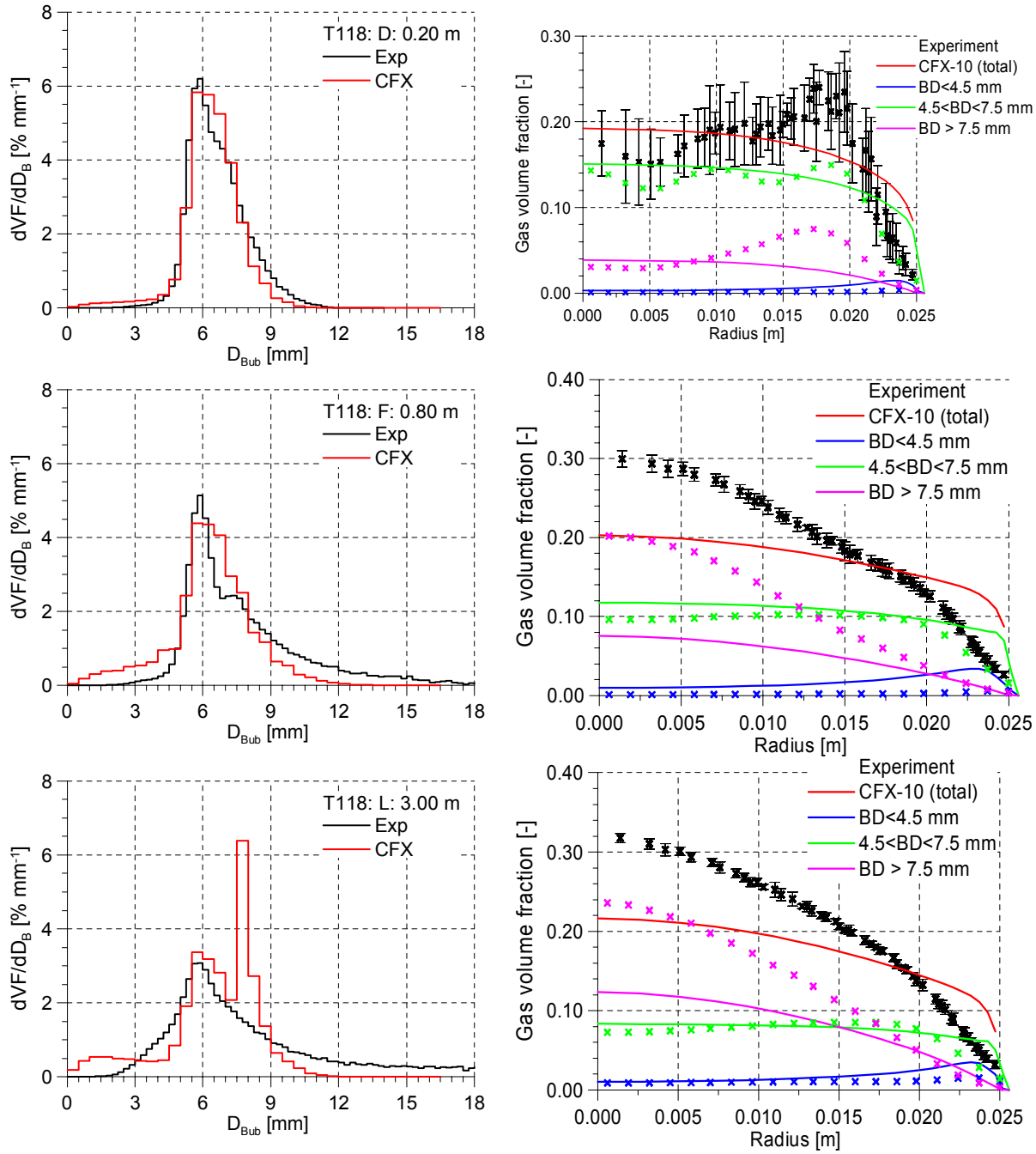

Fig. 6.6 Development of the bubble size distribution (left) and the radial gas fraction profiles (right) of the simulation of the test case MT-Loop 118 (J_L=1.017 m/s; J_G=0.2194 m/s) 3 dispersed phases, 34 MUSIG Groups (F_B=0.25, F_C=0.05)

The investigations show that the increasing number of dispersed phases does not improve the agreement to the measurements. On the other side the computational effort is increased and it is becoming more difficult to achieve a certain convergency level.

The same investigations but not presented here with the same set of parameters for breakup and coalescence were performed also for the test 107 (J_L=1.017 m/s, J_G=0.14 m/s). Here the 21 MUSIG groups were assigned to 2, 3 and 4 dispersed phases with the overall same results.

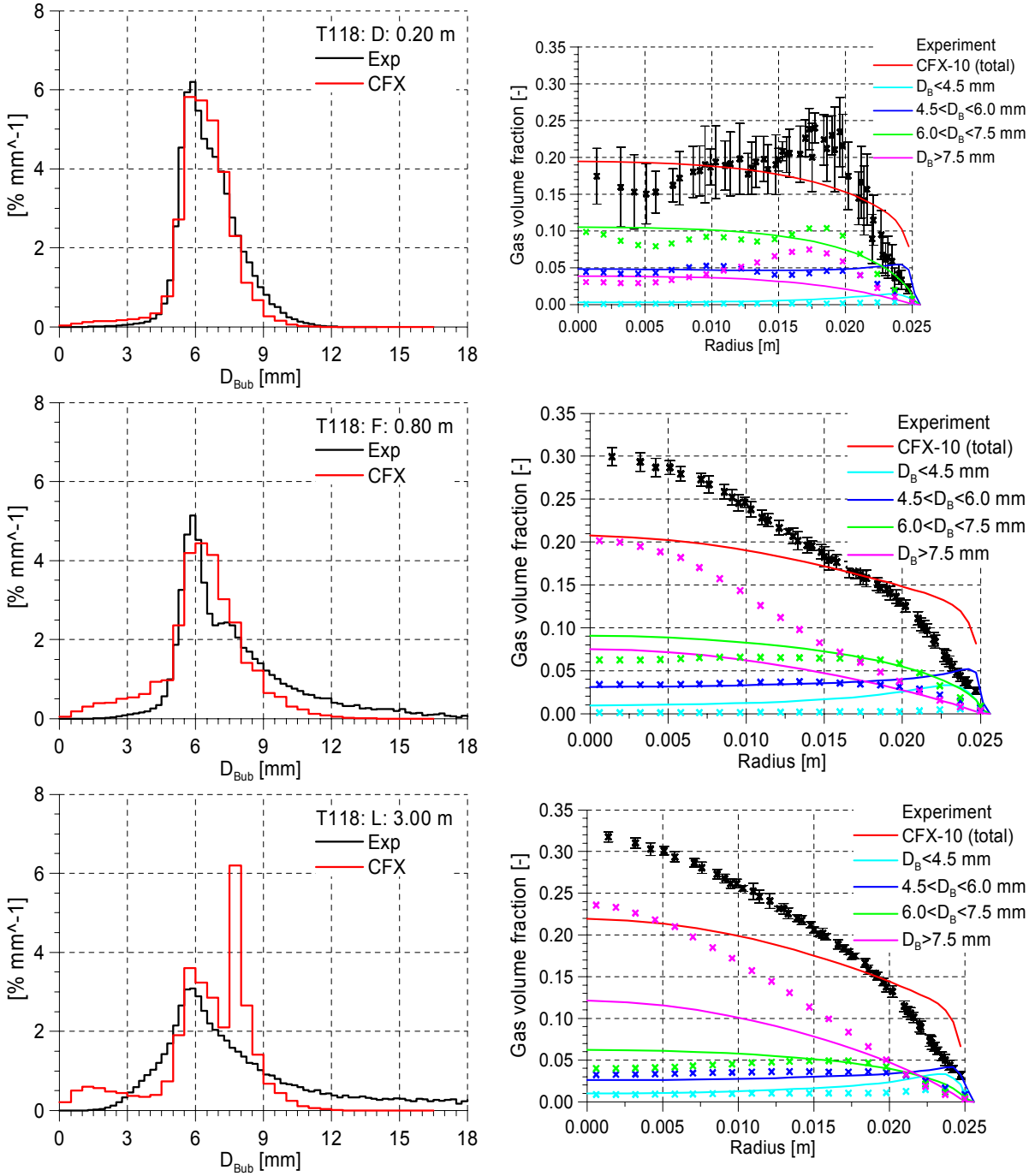

Fig. 6.7 Development of the bubble size distribution (left) and the radial gas fraction profiles (right) of the simulation of the test case MT-Loop 118 (J_L=1.017 m/s; J_G=0.2194 m/s) 4 dispersed phases, 34 MUSIG Groups (F_B=0.25, F_C=0.05)

6.2.2 Test TOPFLOW-107 and 118

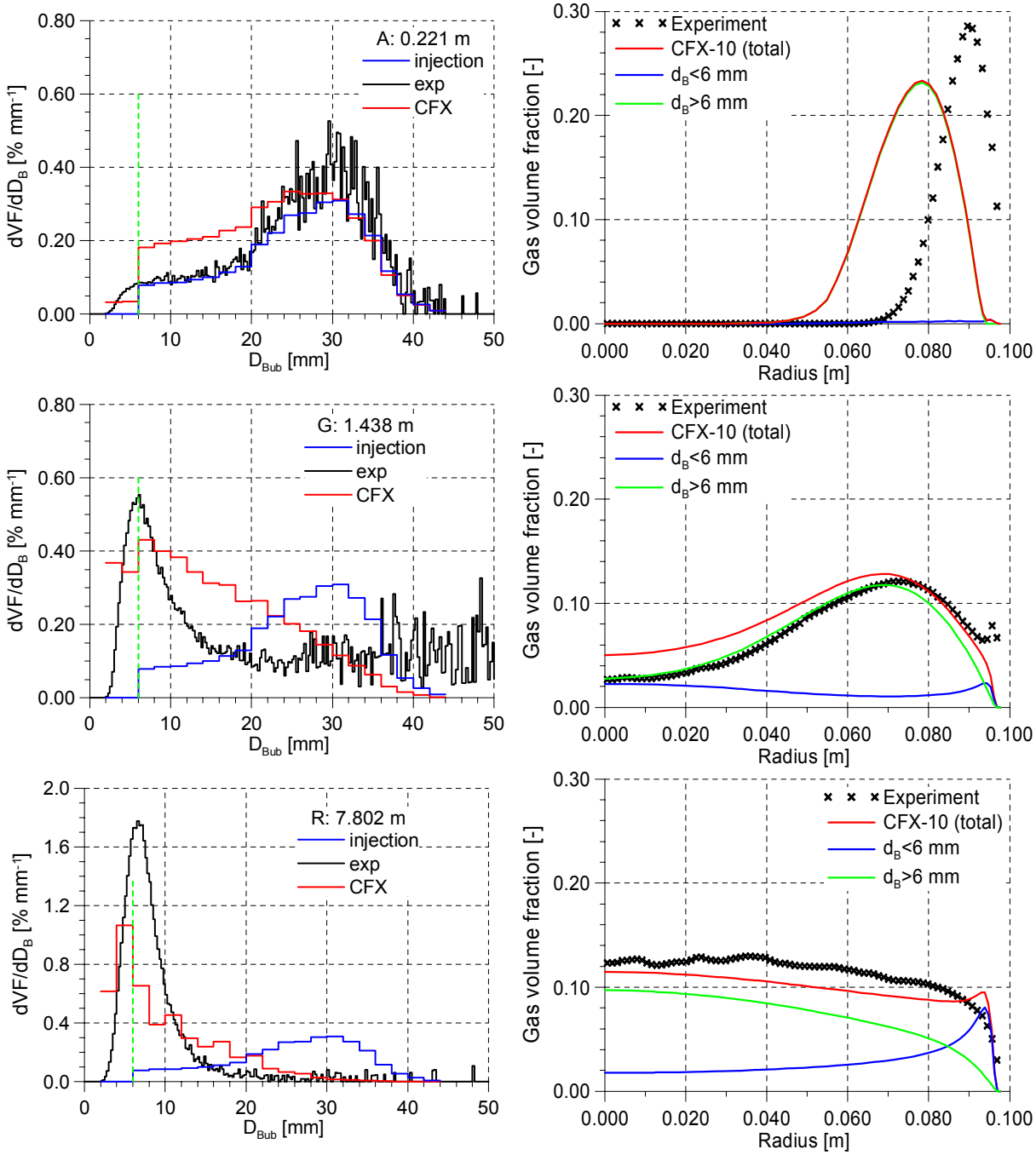

Fig. 6.8 Development of the bubble size distribution (left) and the radial gas fraction profiles (right) of the simulation of the test case TOPFLOW 107 (J_L=1.017 m/s; J_G=0.140 m/s) (F_B=0.25, F_C=0.05)

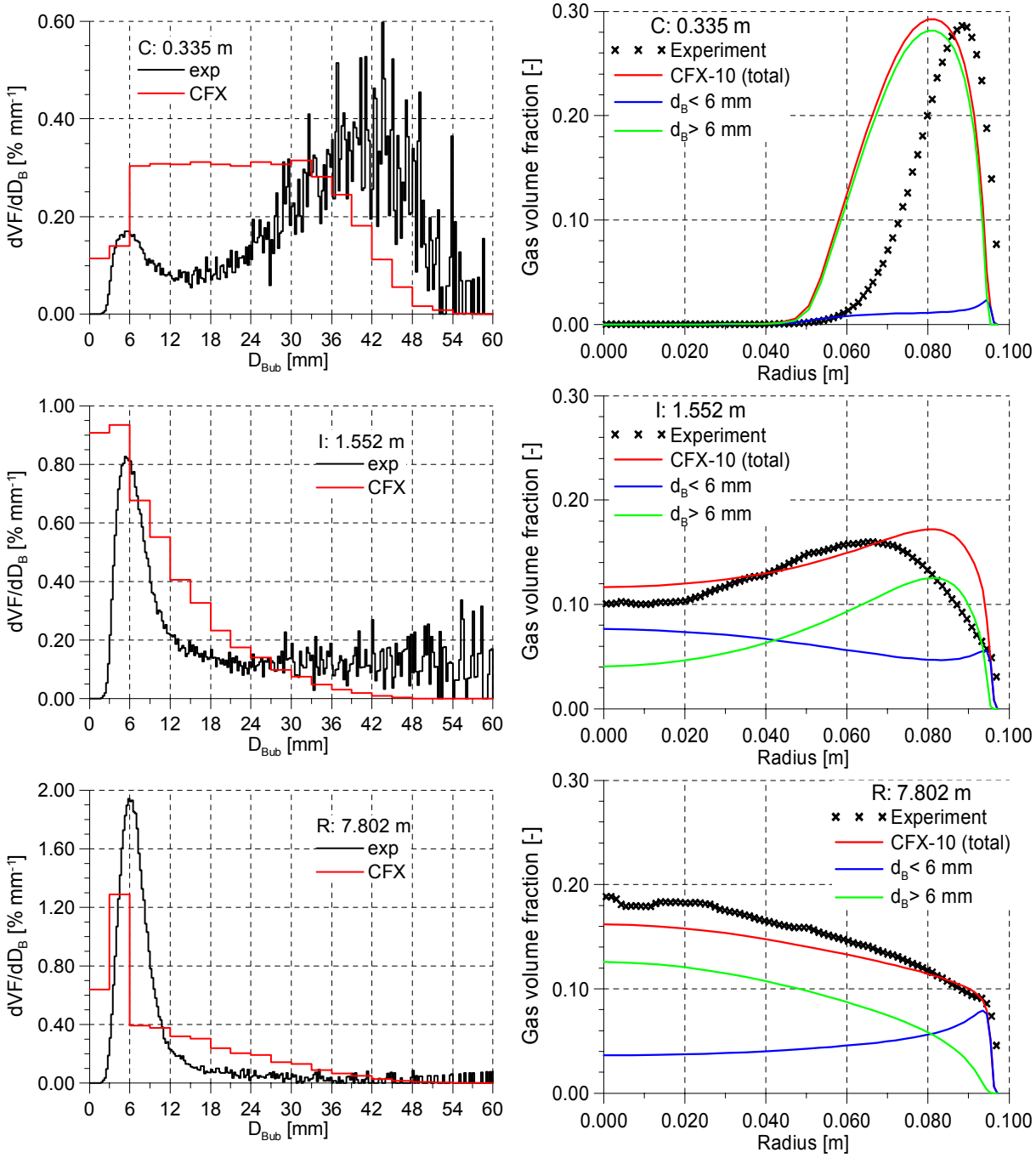

Fig. 6.9 Development of the bubble size distribution (left) and the radial gas fraction profiles (right) of the simulation of the test case TOPFLOW 118 (J_L=1.017 m/s; J_G=0.2194 m/s) (F_B=0.25, F_C=0.05)

In the TOPFLOW test, bubbles were injected from the side walls through 4 mm nozzles into a tube of diameter 195.3 mm (see Fig. 6.8 radial profiles for level A). The bubble size distribution near the inlet compared to the MT-Loop test in 6.2.1 is shifted to much larger values of the bubble diameter (blue size distribution left side). Whereas in the MT-Loop test at the inlet a maximum bubble size of about 10 mm was found, here the injected bubble size is extended to about 40 mm. During the upward flow through the tube the size distribution is shifted towards lower values. Thus the development of the bubble size distribution is mainly determined by

fragmentation processes. Bubble coalescence plays only a minor role at the flow conditions of the experimental test. Fig. 6.8 shows the bubble size distribution and radial gas profiles for the test case TOPFLOW 107. Note that only two dispersed phases were defined for the numerical model. 21 sub-size groups were then specified the first 2 sub-size groups assigned to the first dispersed phase and the other 19 to the second dispersed phase. The bubble size diameter was defined up to 44 mm, the size step between the sub-size groups amounts to 2 mm. Like for the previous case the breakup coefficient was set to F_B=0.25 and the coalescence coefficient to F_C=0.05. Fig. 6.10 compares the development of the cross sectional averaged mean sauter diameter for the MT-Loop tests (left side, see 6.2.1) and the TOPFLOW tests (right side, see 6.2.2).

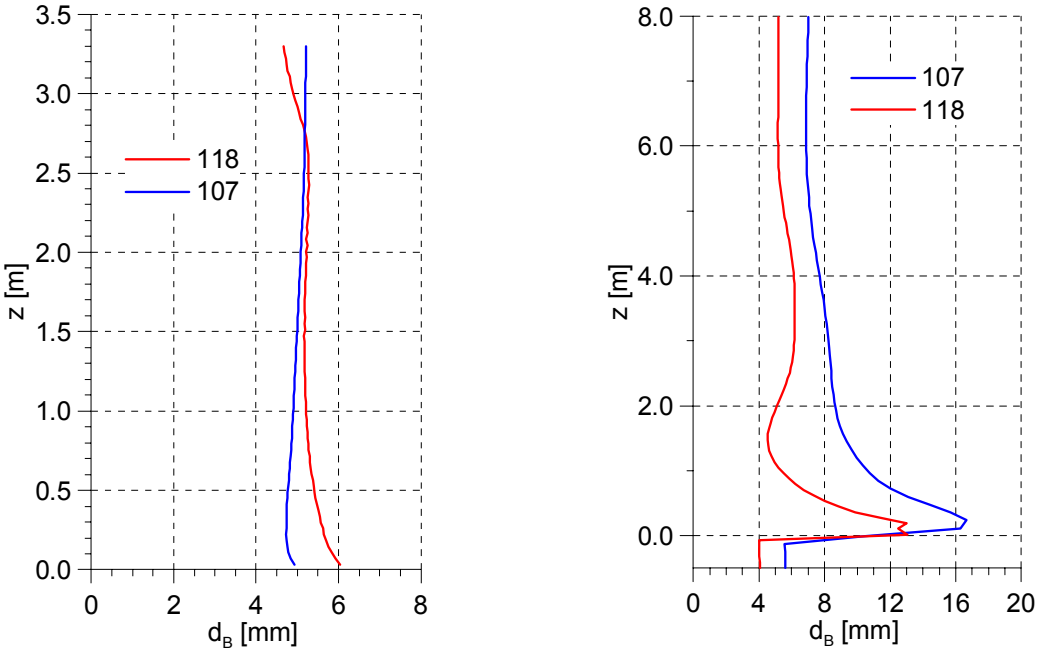

MT_Loop (see chapter 6.2.1) TOPFLOW (see chapter 6.2.2)

Fig. 6.10 Development of the cross sectional averaged mean sauter diameter

6.3 Experiments with water/steam at saturation conditions

6.3.1 Boundary conditions

Water/steam flow was investigated at pressures of 1, 2, 4 and 6.5 MPa. Analysing water/steam instead of water/air flow the changed fluid properties and phase transfer by evaporation or condensation has to be considered. As a first step in the experiments the phase transfer was excluded respective limited by keeping saturation conditions. Saturation conditions can be adjusted only locally. Caused by the hydrostatic pressure, the saturation temperature at the upper end of the tube is lower then at the steam injection at the lower end. This saturation temperature difference is smaller for higher system pressures. Whereas at normal conditions T_{sat} changes by more than 3 K/m at 2 MPa the change amounts to only 0.2 K/m (see Fig. 6.11). Therefore for the first calculations tests with the highest investigated pressures – here 6.5 MPa - was selected.

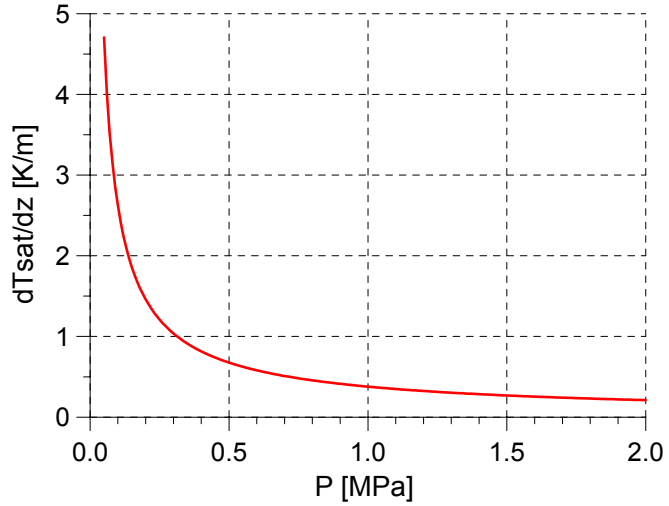

Fig. 6.11 Hydrostatic height gradient of T_{sat} at different system pressure

In chapter 2.1.3 was shown, that the lift coefficient C_L changes its sign with higher bubble size. For air/water flow at normal conditions the critical bubble size, for which C_L=0 amounts to be 5.8 mm. The analysis of the correlation for the lift coefficient (eq. (2.11) given by Tomiyama (1998) shows, that with higher pressure the critical bubble size is shifted towards lower values (see Fig. 6.12). For steam/water at 6.5 MPa a value of about 3.5 mm and at 15 MPa of about 2 mm was found. These tendencies were confirmed by the TOPFLOW experiments (see Prasser et al. 2005).

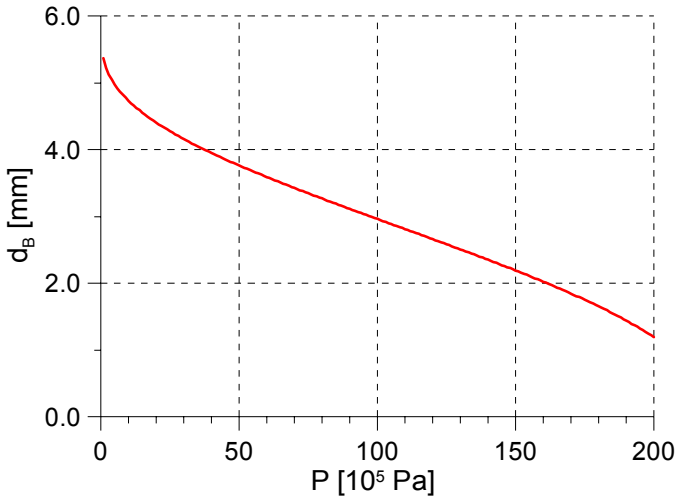

Fig. 6.12 Dependency of the critical bubble size (C_L =0) on the pressure according eq. (2.11)

The changed fluid properties have influence on the calculated turbulence parameters of the liquid. Fig. 6.13 shows the radial profiles for the turbulence kinetic energy, the turbulence dissipation and the turbulent viscosity. For steam/water at 6.5 MPa the first two values are almost doubled compared to air/water flow. Since the bubble fragmentation is strongly influenced by the turbulence dissipation of the liquid phase it is not surprising that the fragmentation coefficient has to be strongly reduced.

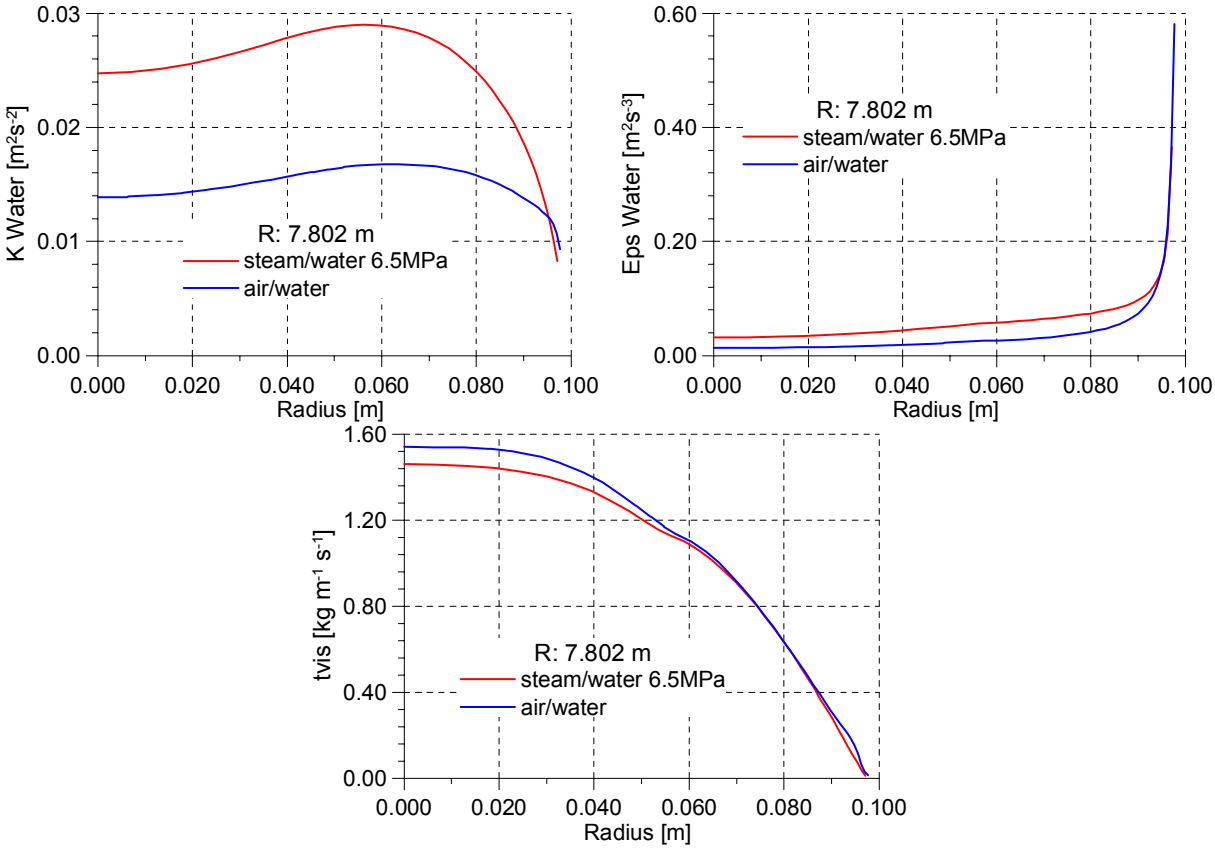

Fig. 6.13 Comparison of the turbulent kinetic energy, the turbulent dissipation and the turbulent viscosity for air/water and steam/water for J_L=1.0167 m/s, J_G=0.140 m/s (TOPFLOW-107)

6.3.2 Results for test TOPFLOW 107 and 118

Fig. 6.15 presents the development of the bubble size distribution and of the radial volume fraction profiles for the steam/water test TOPFLOW-107 and Fig. 6.16 for TOPFLOW-118. At 6.5 MPa steam water flow with superficial velocities J_L=1.017 m/s and J_G=0.140 m/s (TOPFLOW-107) respective J_G=0.12194 m/s (TOPFLOW-118) was analyzed. In both simulations 25 sub-size gas fractions assigned to two dispersed phases were simulated. For TOPFLOW-107 the minimum considered bubble size was 0.5 mm and the maximum 25.5 mm. For TOPFLOW-118 the minimum considered bubble size was 0 mm and the maximum 37.5 mm. With equidistant bubble size distribution only the lowest three sub-size gas fractions (107) respective two (118) were assigned to the first dispersed phase. For these flow conditions the critical bubble size for C_L=0 was 3.5 mm.

Whereas the factor for bubble coalescence was set like in the air/water simulations F_C=0.05 the fragmentation coefficient lead to a strong overestimation of bubble fragmentation (see Fig. 6.14 for test 107). Consequently this coefficient in the further simulations was remarkably reduced to F_B=0.025. Fig. 6.15 and Fig. 6.16 show that applying the models with these tuned coalescence and fragmentation coefficients a reasonable simulation of the development of bubble size distribution and radial gas volume fraction profile is possible.

Compared to the air/water simulations (see Fig. 6.8, Fig. 6.9 for TOPFLOW-107, 118) the migration of the bubbles from the injection at the wall to the centre of the tube is simulated slower in the steam/water case. Whereas in the air/water simulations the air moves too fast from the side wall injection into the tube centre, in the steam/water tests the gas migration to the tube centre is underestimated. The reason could be the overestimated turbulent dispersion bubble force in the air/water cases. This corresponds also with the investigations in chapter 5.3 and 5.4. Caused by the other fluid properties the turbulent bubble dispersion force seams to be underestimated. Further investigations are necessary.

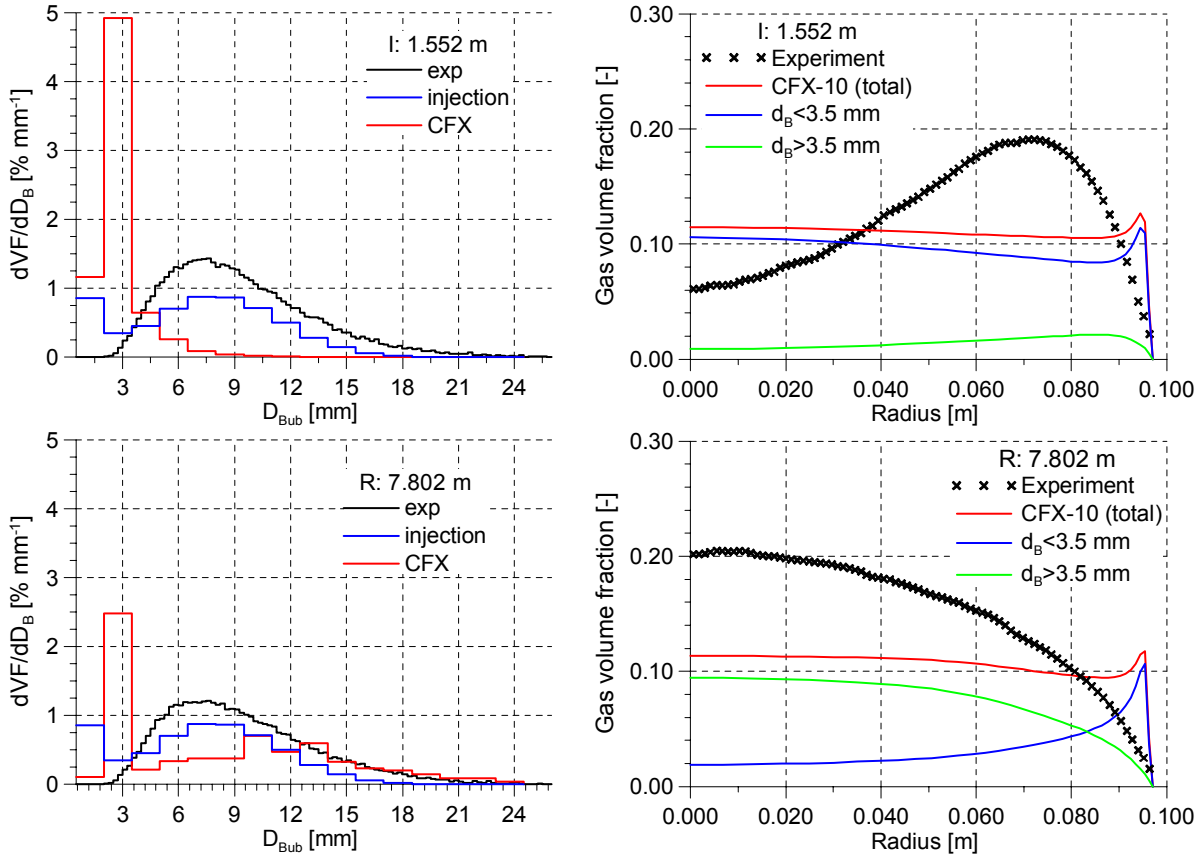

Fig. 6.14 Development of the bubble size distribution (left) and the radial gas fraction profiles (right) of the simulation of the test case TOPFLOW 107 for saturated steam/water at 6.5 MPa (J_L=1.017 m/s; J_G=0.140 m/s) (F_B=0.25, F_C=0.05)

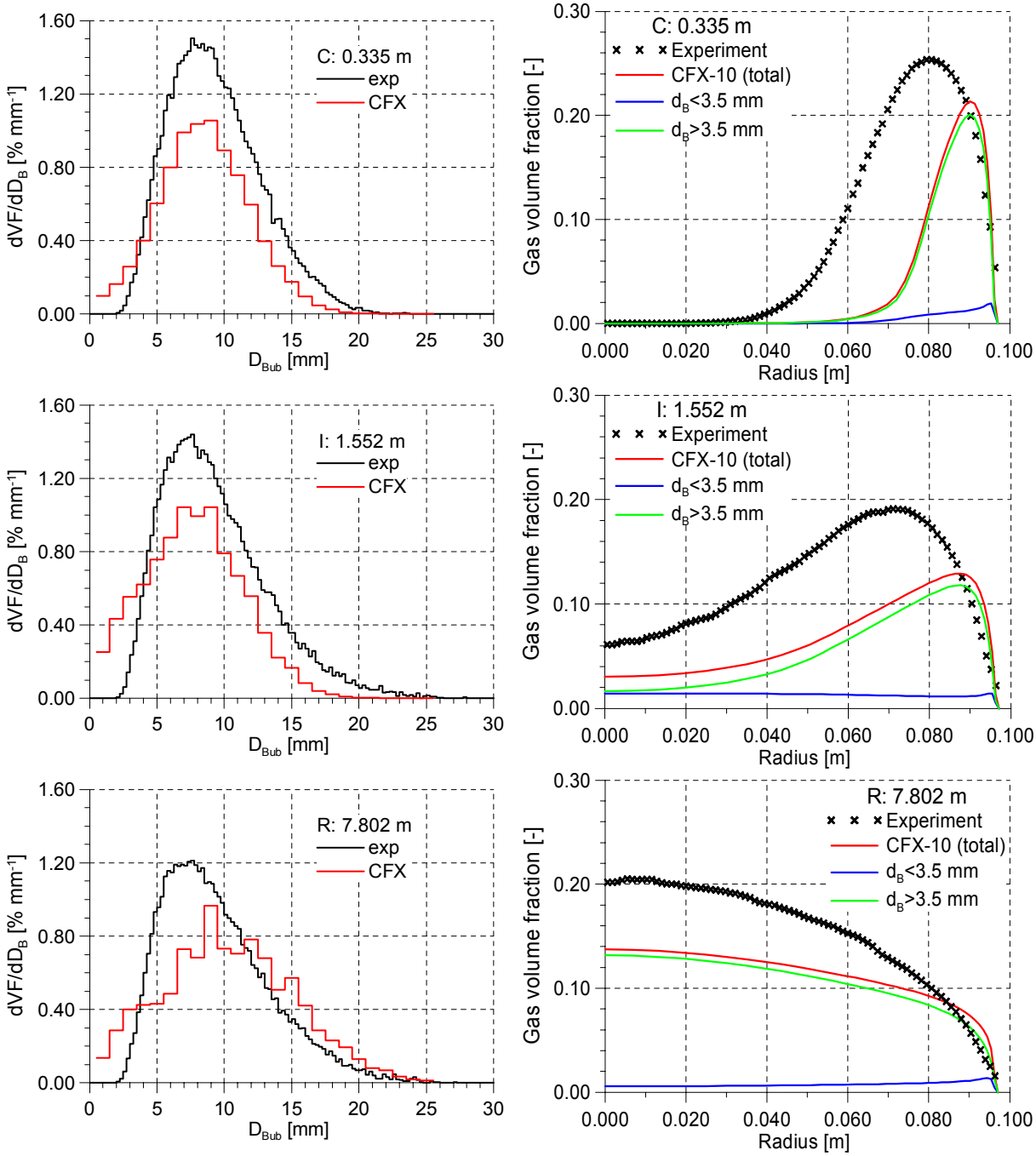

Fig. 6.15 Development of the bubble size distribution (left) and the radial gas fraction profiles (right) of the simulation of the test case TOPFLOW 107 for saturated steam/water at 6.5 MPa (J_L=1.017 m/s; J_G=0.140 m/s) (F_B=0.025, F_C=0.05)

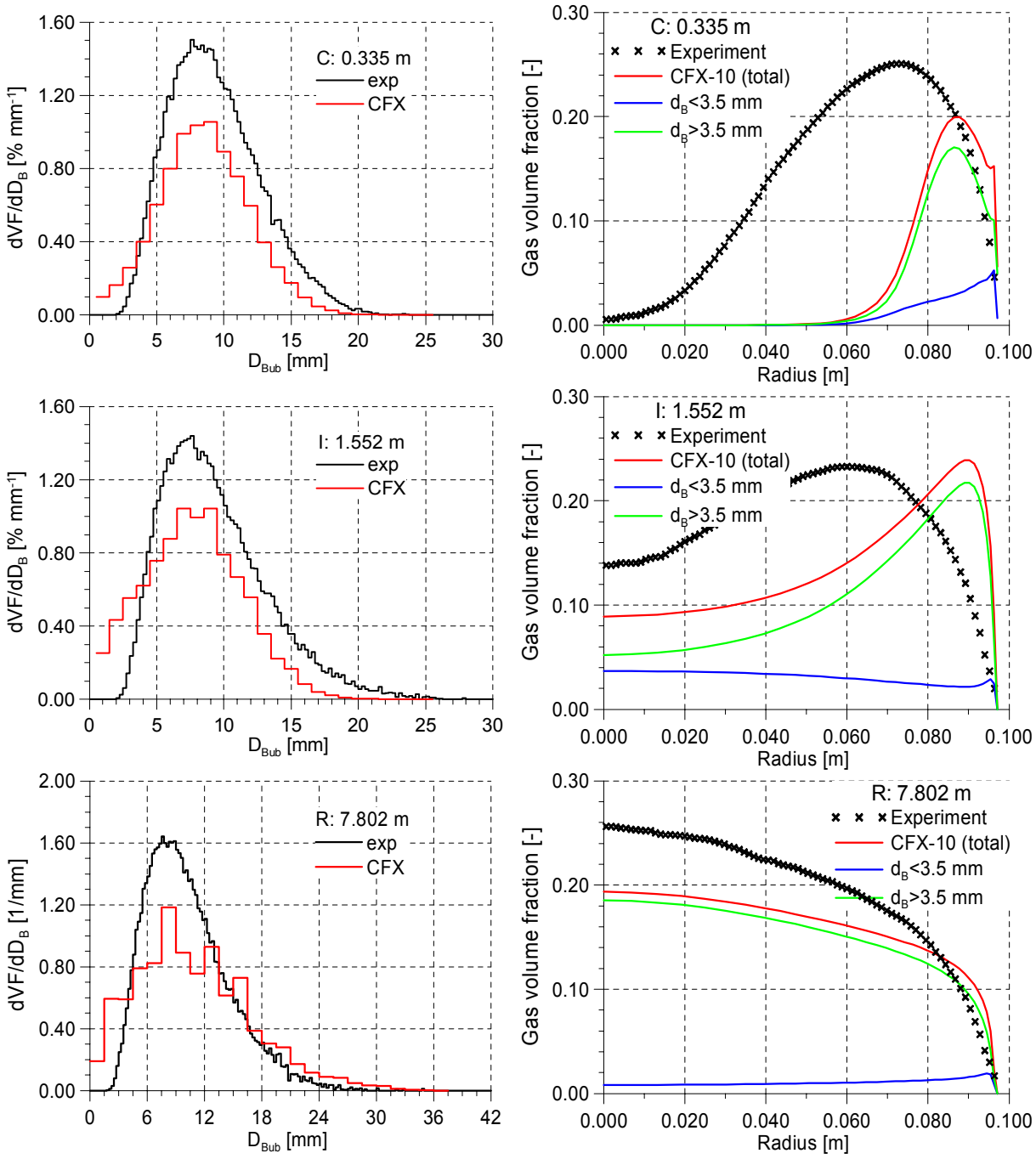

Fig. 6.16 Development of the bubble size distribution (left) and the radial gas fraction profiles (right) of the simulation of the test case TOPFLOW 118 for saturated steam/water at 6.5 MPa (J_L=1.017 m/s; J_G=0.2194 m/s) (F_B=0.025, F_C=0.05)

7. Validation for obstacle

The large test section with a nominal diameter of DN200 was used to study the flow field around an asymmetric obstacle (see Fig. 7.1). This is an ideal test case for CFD code validation, since the obstacle creates a pronounced three-dimensional two-phase flow field. Curved stream lines, which form significant angles with the gravity vector, a recirculation zone in the wake and a flow separation at the edge of an obstacle are common in industrial components and installations.

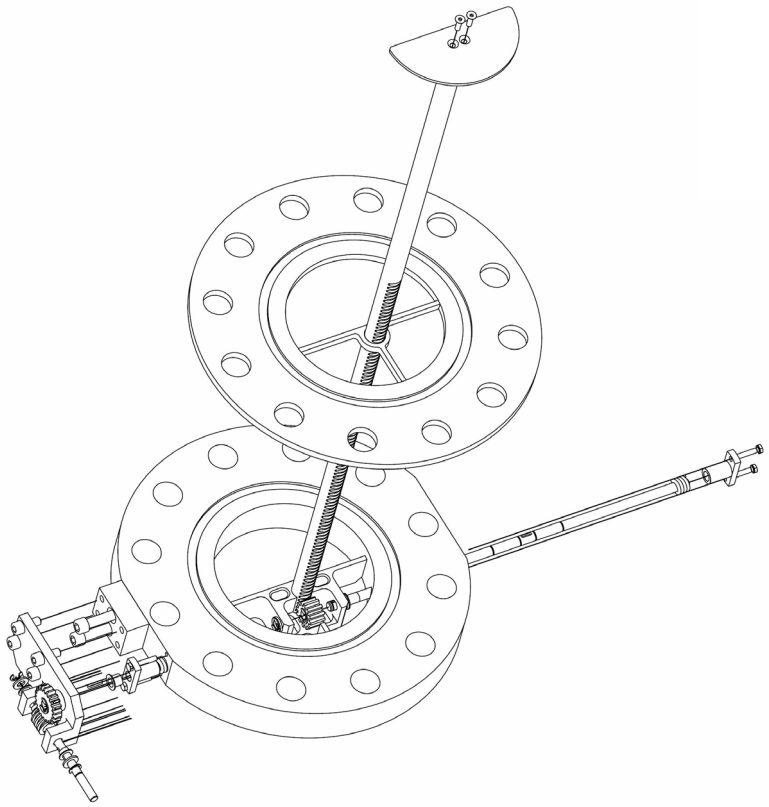

Fig. 7.1 Sketch of the movable obstacle with driving mechanism - a half-moon shaped horizontal plate mounted on top of a toothed rod

Experiments were performed with an air-water flow at ambient conditions as well as with a steam-water mixture at a saturation pressure of 6.5 MPa. The measurements were carried out in the vertical test section of TOPFLOW using a DN200 wire-mesh sensor. The wire-mesh sensors are available for ambient conditions as well as for saturated conditions at a pressure up to 7 MPa and supply detailed data on the instantaneous flow structure with a high resolution in space and time. In particular, this allows to visualize the structure of the gas liquid interface. A detailed description of the experiments is given in the Technical Report “Experiments on two-phase flow in a vertical tube with a moveable obstacle”.

Pretest calculations using CFX-10 applying a monodispersed bubble size approach were performed for the conditions of test 074 (J_L = 1.017 m/s, J_G = 0.0368 m/s) (see Frank, 2006, Prasser et al. 2005). All phenomena later observed during the experiments for low gas content were predicted already by the first calculations. In

the calculation a fluid domain 1.5 m upstream and downstream the obstacle was modeled.

In the actual report the inhomogeneous MUSIG approach is applied for the air/water case also with higher gas injection rates. The capability of the model framework simulating the complex relations between bubble dynamics and bubble size distributions were investigated.

7.1 The main observed phenomena

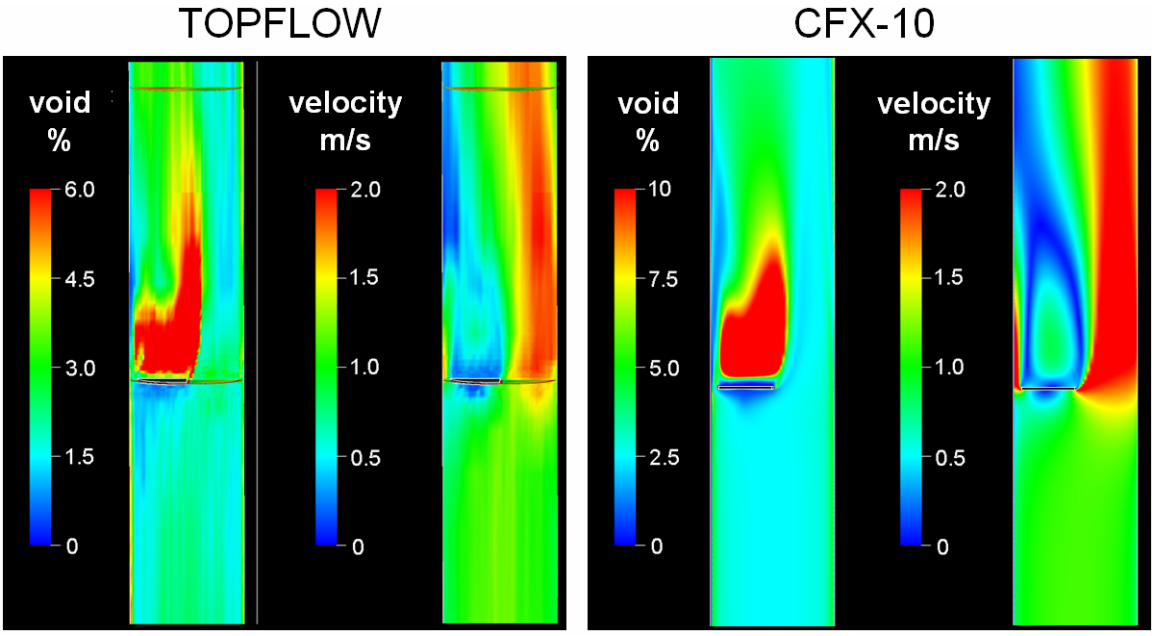

Fig. 7.2 Comparison of time averaged void fraction and liquid velocity distributions up- and downstream of the obstacle in the air-water test run 074, J_L = 1.017 m/s, J_G = 0.0368 m/s

Like in the pretest calculations also the steady-state ANSYS CFX calculations applying the inhomogeneous MUSIG model could reproduce all qualitative details of the flow structure of the two-phase flow field around the diaphragm for the low gas fraction of run 074.

The ANSYS CFX simulation results have been compared to three-dimensional wire-mesh sensor data by importing pre-interpolated experimental data for bubble size, volume fraction and phase velocity components into the CFX post-processor. Fig. 7.2 shows the comparison. In the CFX-10 results for the void fraction the total air volume fraction summarized over all size fractions is presented.

Short behind the obstacle a strong vertex of the liquid combined with a higher accumulation of gas is found. The measured and calculated shape and extension of the recirculation area very well agree. At the obstacle upstream a stagnation point with lower gas content is seen in experiments and calculation. Smaller details, like the velocity and void fraction maxima above the gap between the circular edge of the obstacle and the inner wall of the pipe are also found in a good agreement between experiment and calculation.

7.2 Bubble size distributions

25 sub-size gas fractions representing equidistant bubble sizes up to 25 mm were simulated assigned to 2 dispersed gaseous phases. The first 6 fractions were assigned to the lower and the remaining 19 to the higher gaseous phase. The bubble size distribution found in the experiment at the inlet was set as an inlet boundary condition for the calculation.

It can be assumed that bubble fragmentation will take place at the edges of the obstacle. Coalescence might become of strong importance in regions of bubble accumulation i.e. in the wake behind the obstacle. Fig. 7.3 presents the turbulence dissipation which is accountable for bubble fragmentation. Both bubble coalescence (see gas accumulation shown in Fig. 7.2) and bubble breakup (see distribution of turbulence dissipation Fig. 7.3) are expected short behind the obstacle. Therefore besides the bubble size distribution 0.52 m upstream and downstream the obstacle particularly the distribution at z=0.08 m was observed.

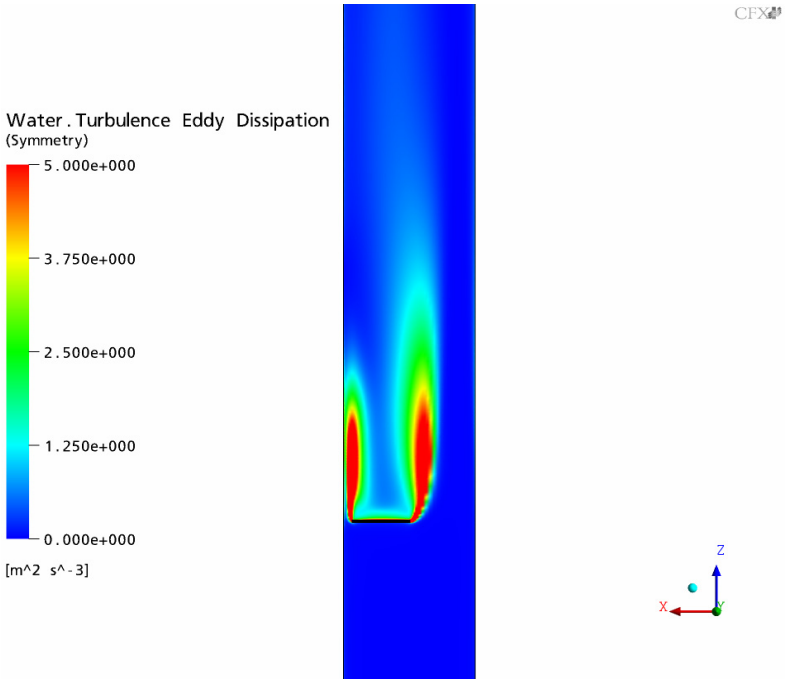

Fig. 7.3 Calculated turbulence eddy dissipation

Fig. 7.4 for the test T074 (J_G=0.0368 m/s) and the left sides of Fig. 7.6 and Fig. 7.7 for the tests T096, T097 and T118 show a shift of the bubble size distribution towards larger bubbles. The measurements show that short behind the obstacle the bubble coalescence caused by gas accumulation exceeds the bubble fragmentation caused by the increased turbulence dissipation at the edges of the obstacle. The calculations were started applying breakup and coalescence coefficients giving the best results for the empty tube (see chapter 6). For the actual test case however these coefficients resulted in a strong overestimation of the bubble breakup (see Fig. 7.5). Even a reduction of the bubble breakup coefficient leads to an overestimation of the bubble breakup (see Fig. 7.6). Finally only the exclusion of the bubble fragmentation lead to the best qualitative agreement to the measured values (see Fig. 7.7).

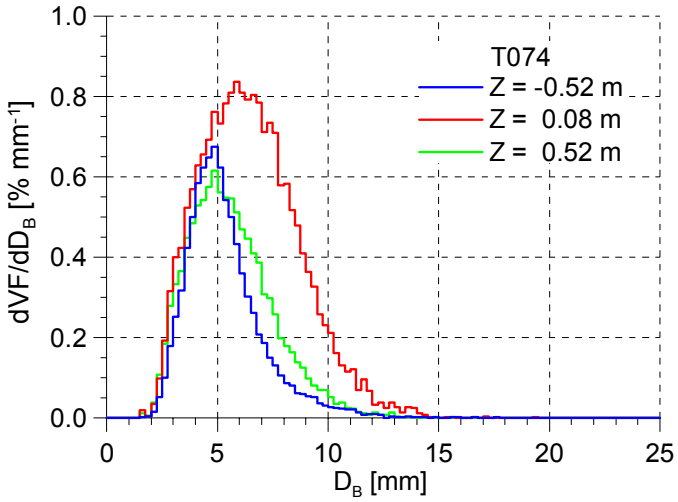

Fig. 7.4 Measured bubble size distribution for the test T074 (J_G=0.0368 m/s)

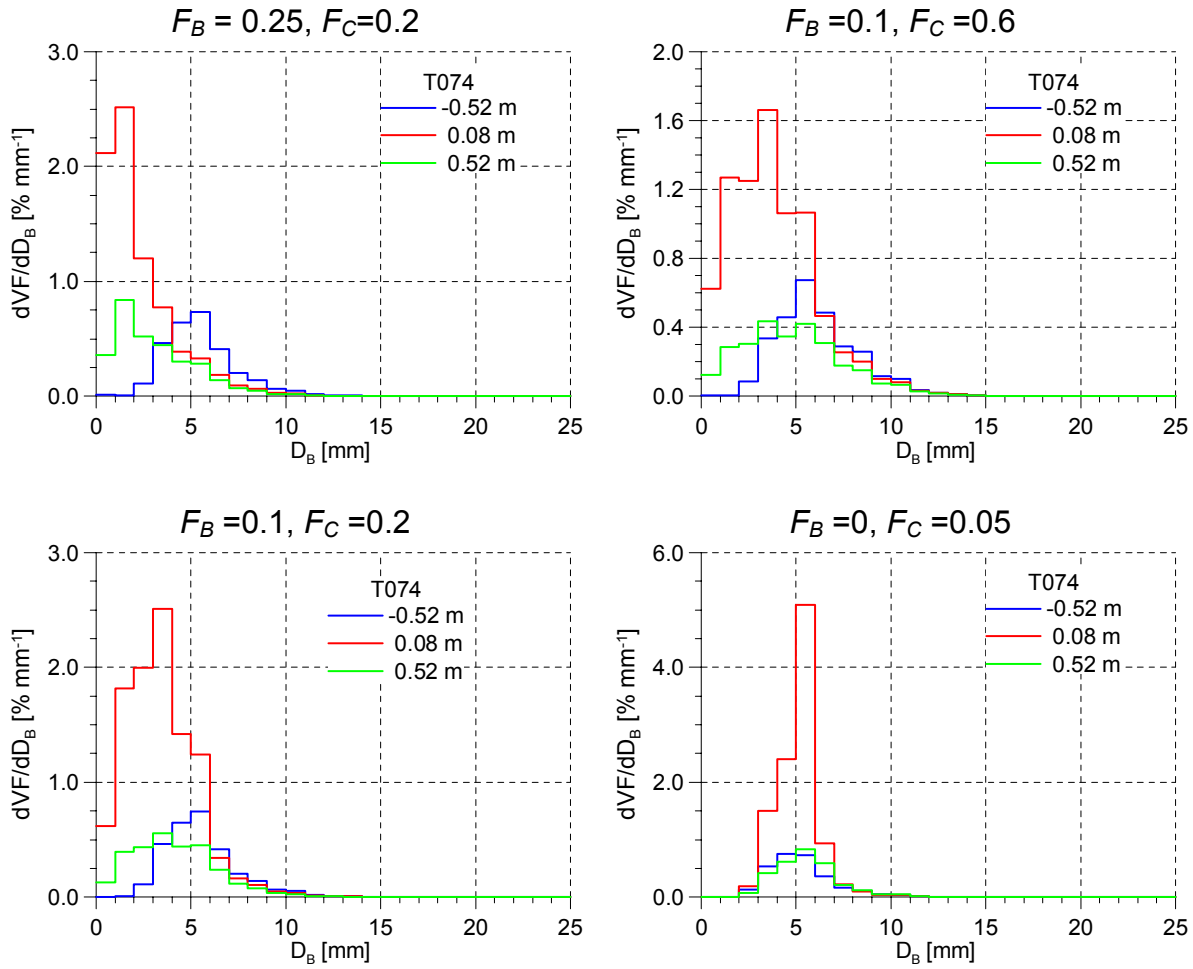

Fig. 7.5 Calculated bubble size distributions for different breakup and coalescence coefficients for the run 074

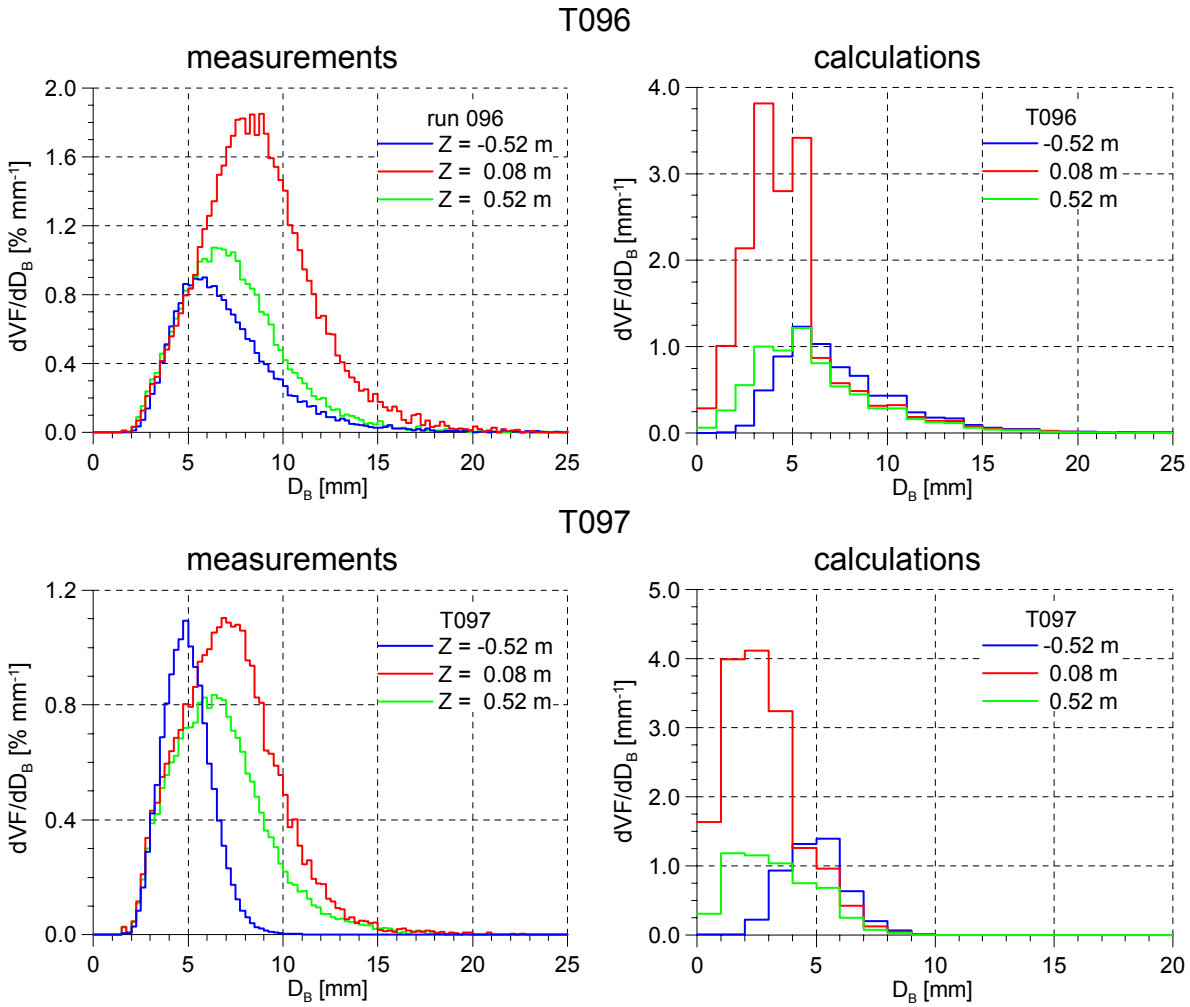

Fig. 7.6 Comparison of measured and calculated bubble size distributions for the tests T096 (J_L = 1.017 m/s) and T097 (J_L = 1.611 m/s, for both tests J_G =0.0898 m/s) (F_B=0.05, F_C=0.05)

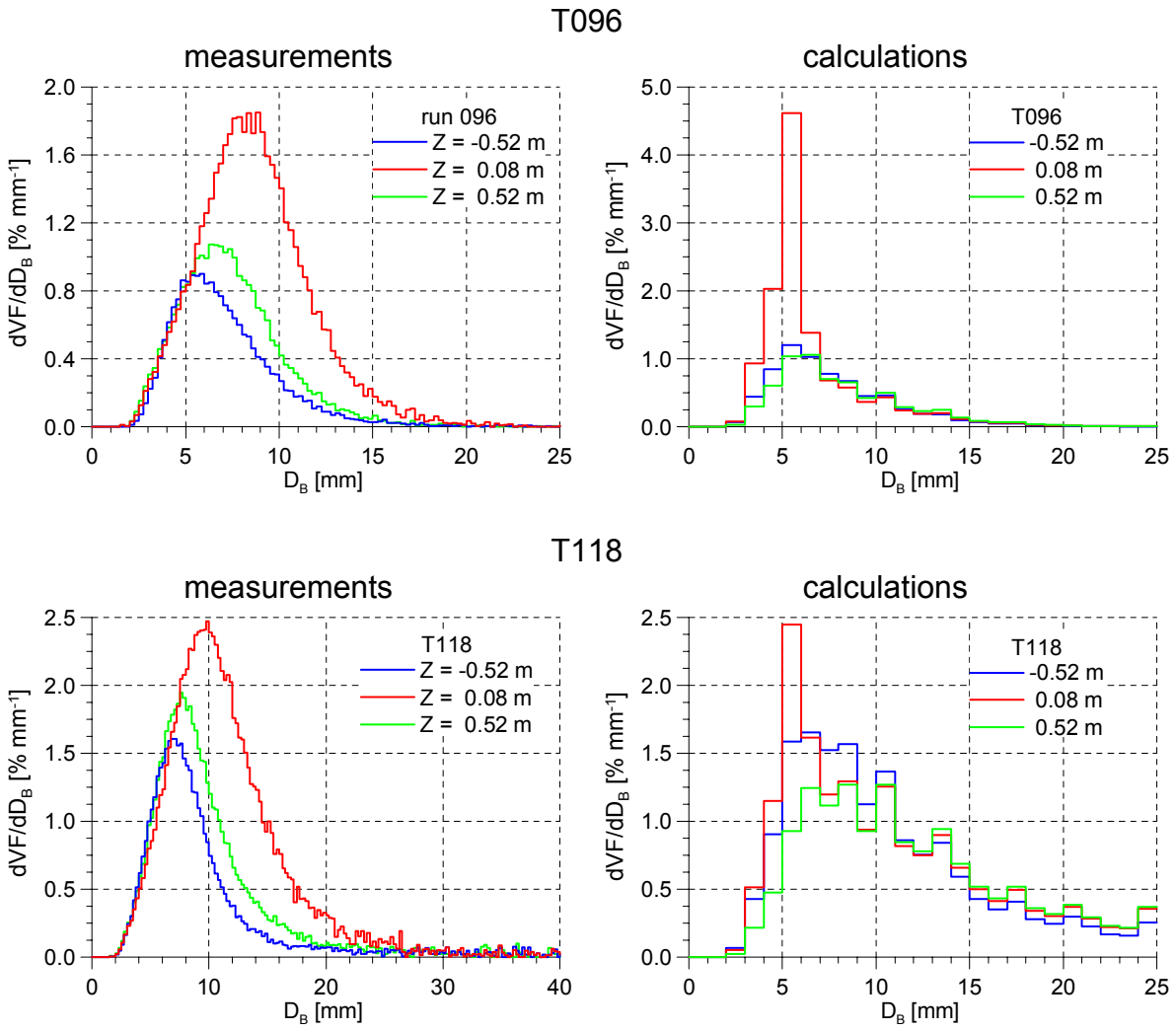

Fig. 7.7 Comparison of measured and calculated bubble size distributions for the tests T096 (J_G =0.0898 m/s) and T118 (J_G =0.219 m/s), (F_B=0, F_C=0.05)

7.3 Simulation applying the inhomogeneous MUSIG approach

Fig. 7.8 presents measured gas distributions resolved according to four bubble size regions. Fig. 7.9 shows the corresponding calculated values for the considered two size classes. In Fig. 7.10 streamlines for the two bubble size classes were calculated by the postprocessor. To analyse the influence of the lift force Fig. 7.11 shows for each bubble size class the force against water.

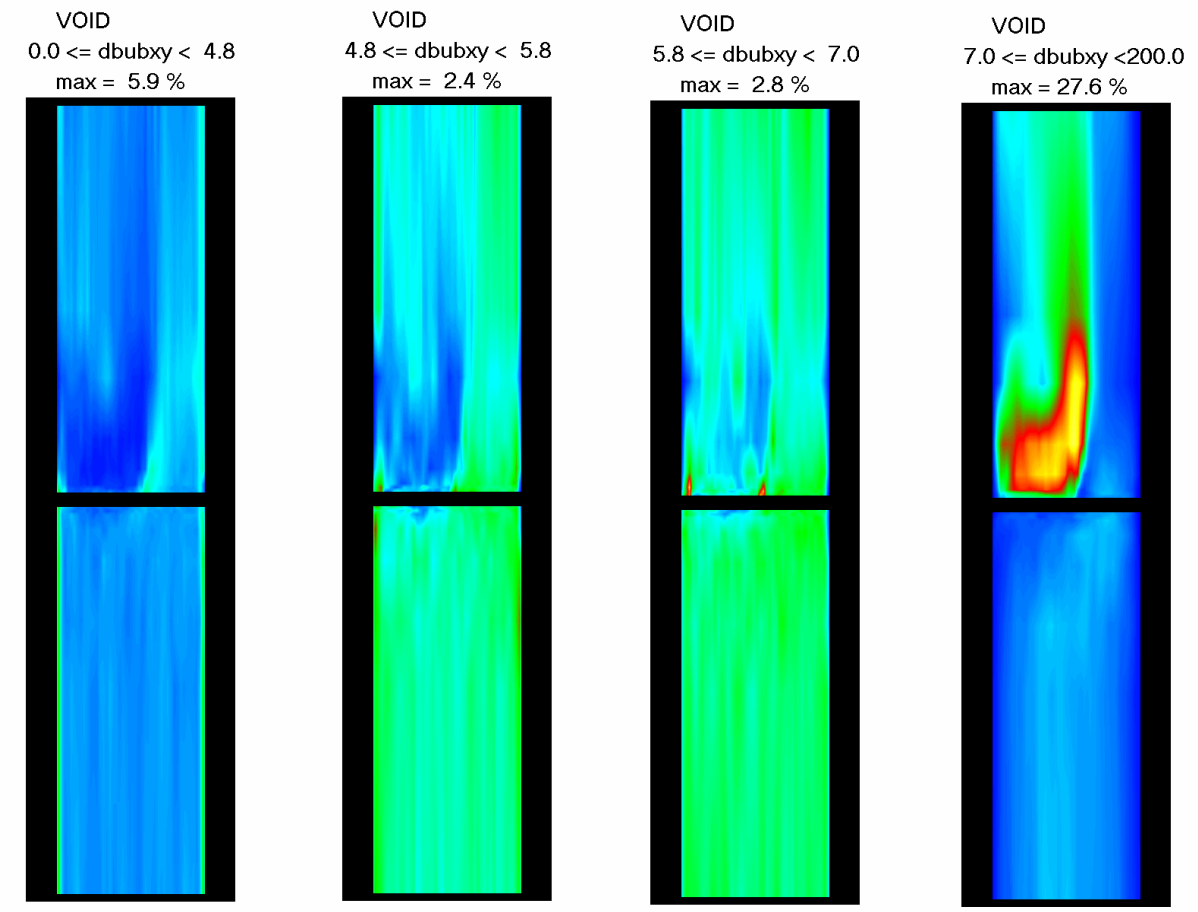

Fig. 7.8 Measured gas distributions resolved to bubble size regions (run 096 J_L = 1.017 m/s, J_G = 0.0898 m/s)

The liquid velocity flow field generates a lift force field which transports the small bubbles in the region behind the obstacle (see Fig. 7.10 for the streamlines of small bubbles and Fig. 7.11 for the lift force arrows). The air accumulation in this region leads to bubble coalescence and the generation of large bubbles. This phenomenon is clearly underestimated in the calculations. The measured bubble size distributions 0.08 m downstream the obstacle and the measured gas distributions presented in Fig. 7.8 shows preferably large bubbles behind the obstacle. Fig. 7.10 shows very well that small bubbles are transported behind the obstacle. In the experiments in this region larger bubbles are created by coalescence. In the calculations however in this region bubble coalescence is exceeded by bubble fragmentation. In most calculated cases the cross sectional averaged bubble size distribution short downstream the obstacle is shifted towards smaller values. Caused by the lift force large bubbles are

redirected into the downstream jet (see Fig. 7.10). The streamline representation shows this phenomenon clear for large bubbles present already in the upstream flow. They do not reach the region behind the obstacle.

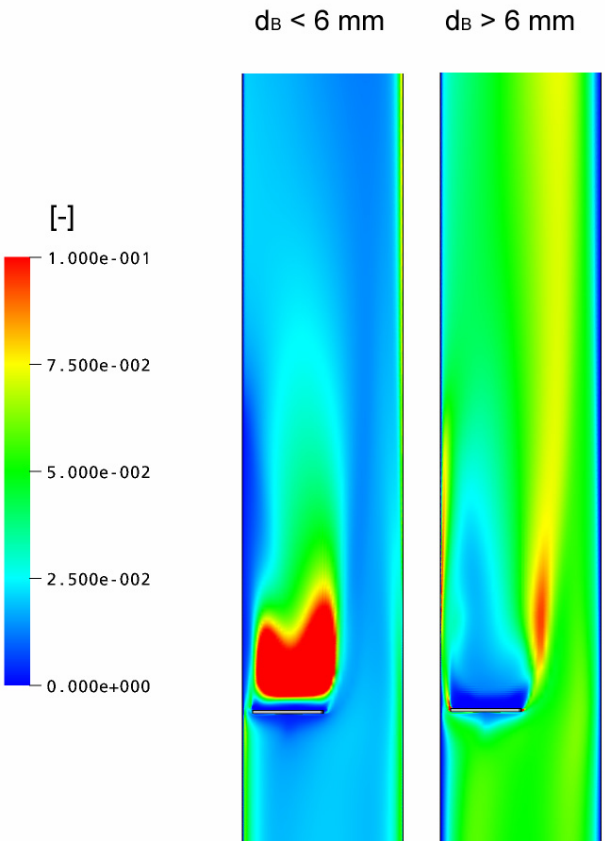

Fig. 7.9 Calculated gas fraction distribution for the different size groups (run 096, J_G =0.0898 m/s)

The analyses of the lift force in the flow solution (Fig. 7.11) shows the separation mechanism, which leads to the different behaviour of the different bubble size classes.

A closer look to the void fraction distribution downstream of the diaphragm shows, that there is a clearly separated stable region of very low gas fractions in the jet that is coming from the non-obstructed part of the cross-section. This effect is presented very pronounced in Fig. 7.12 but was observed in air-water tests at ambient pressure and at superficial water velocities above 0.4 m/s. Bubbles are obviously hindered fro entering the jet by the lift force. They crowd up at the boundary of the jet, where a local gas fraction maximum is found. In the calculations this phenomenon can also be found for small bubbles (see Fig. 7.13). For the total values the phenomenon is partially compensated by the contributions of large bubbles (see Fig. 7.14). The calculated bubble size distribution has a strong influence on the integral gas distribution.

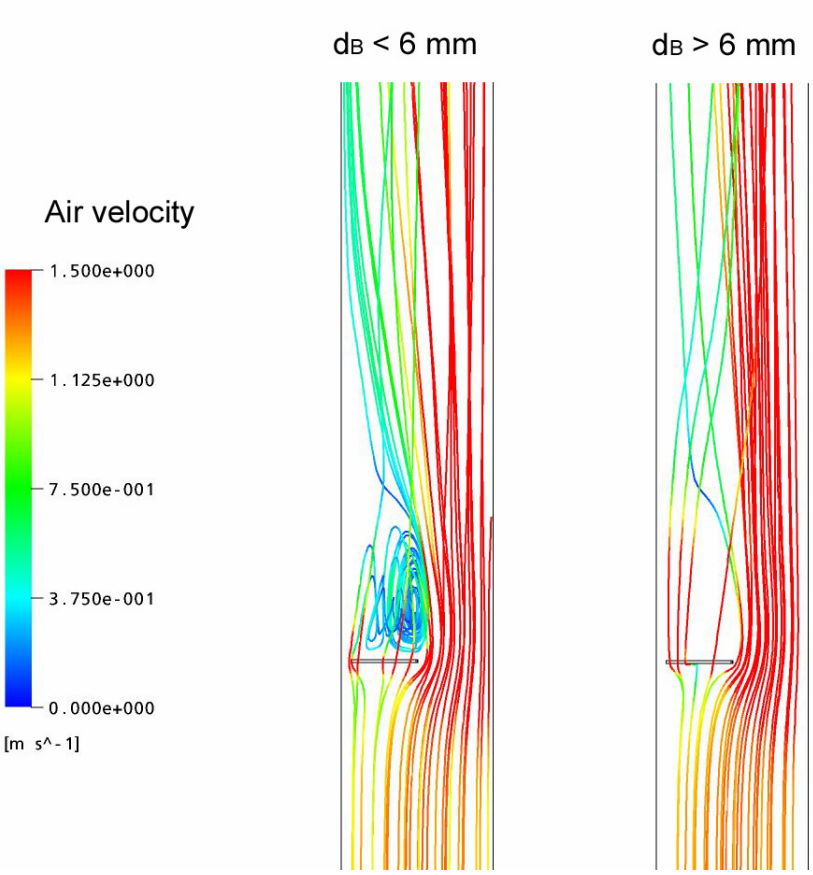

Fig. 7.10 Streamlines for small (left) and large (right) bubbles (run 096, J_G = 0.0898 m/s)

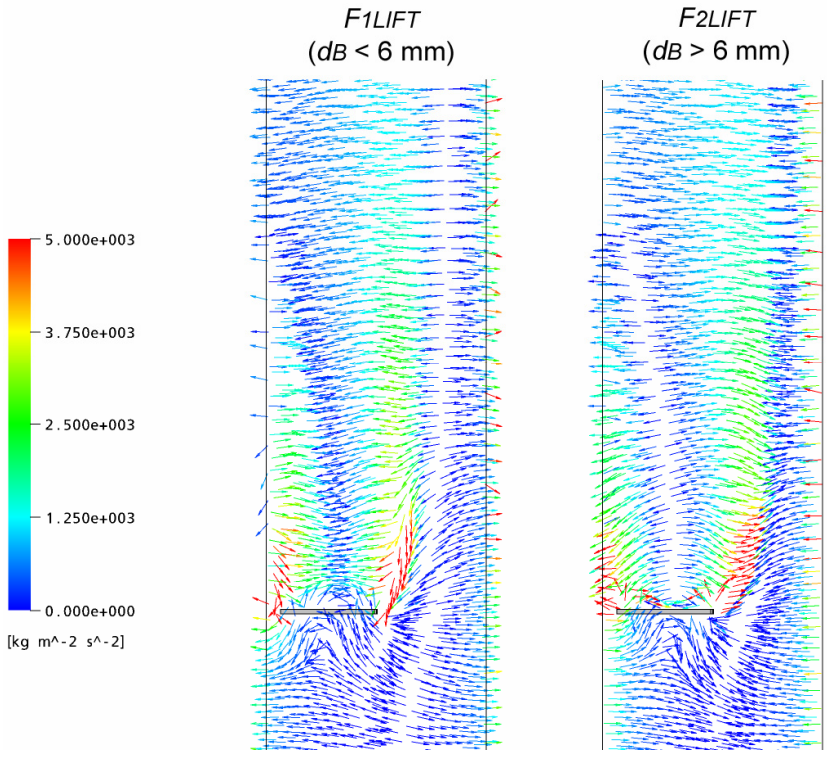

Fig. 7.11 Bubble lift force vectors for the different gas velocity groups against water

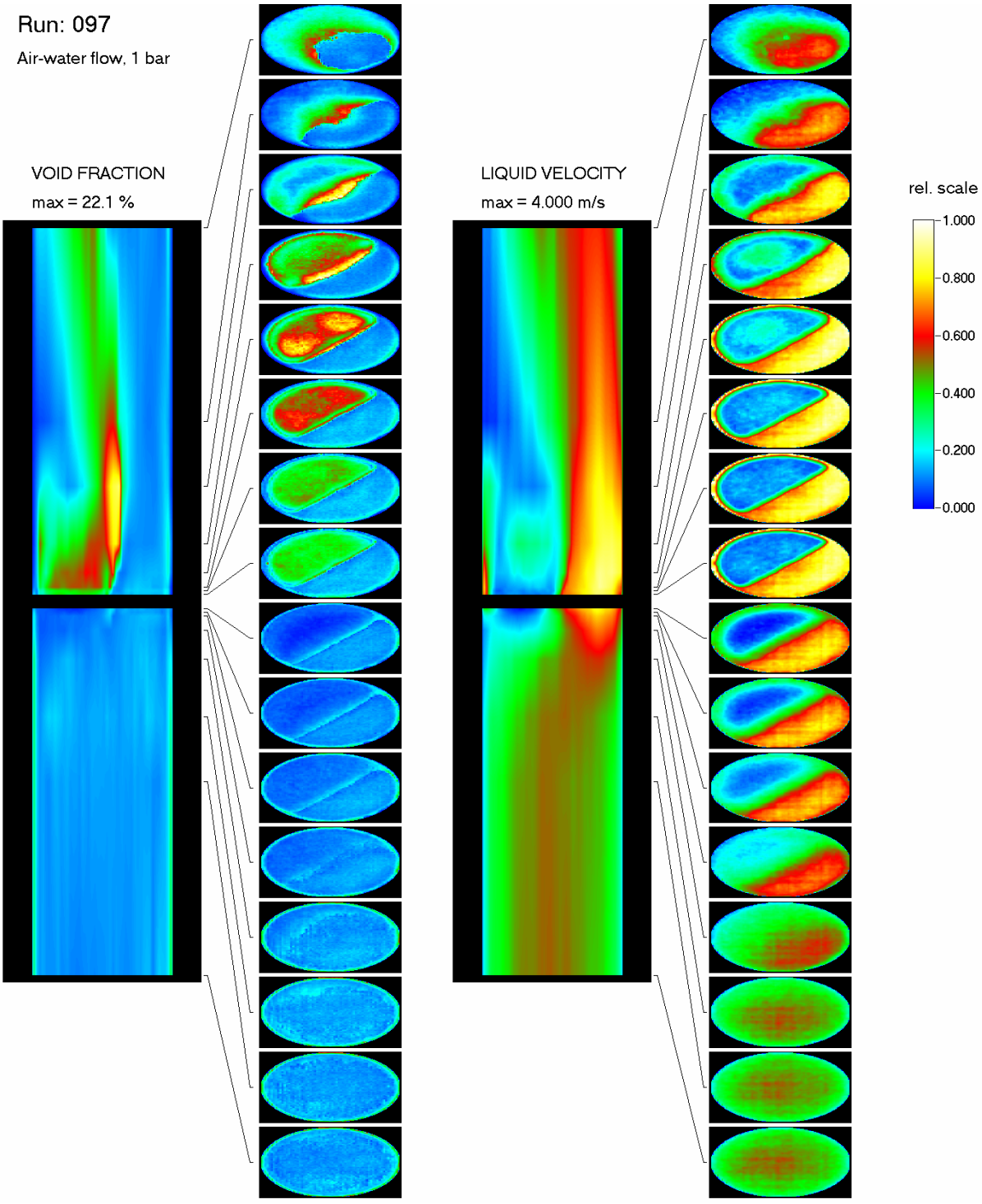

Fig. 7.12 Axial and cross sectional distribution of the total gas volume fraction and of the liquid velocity

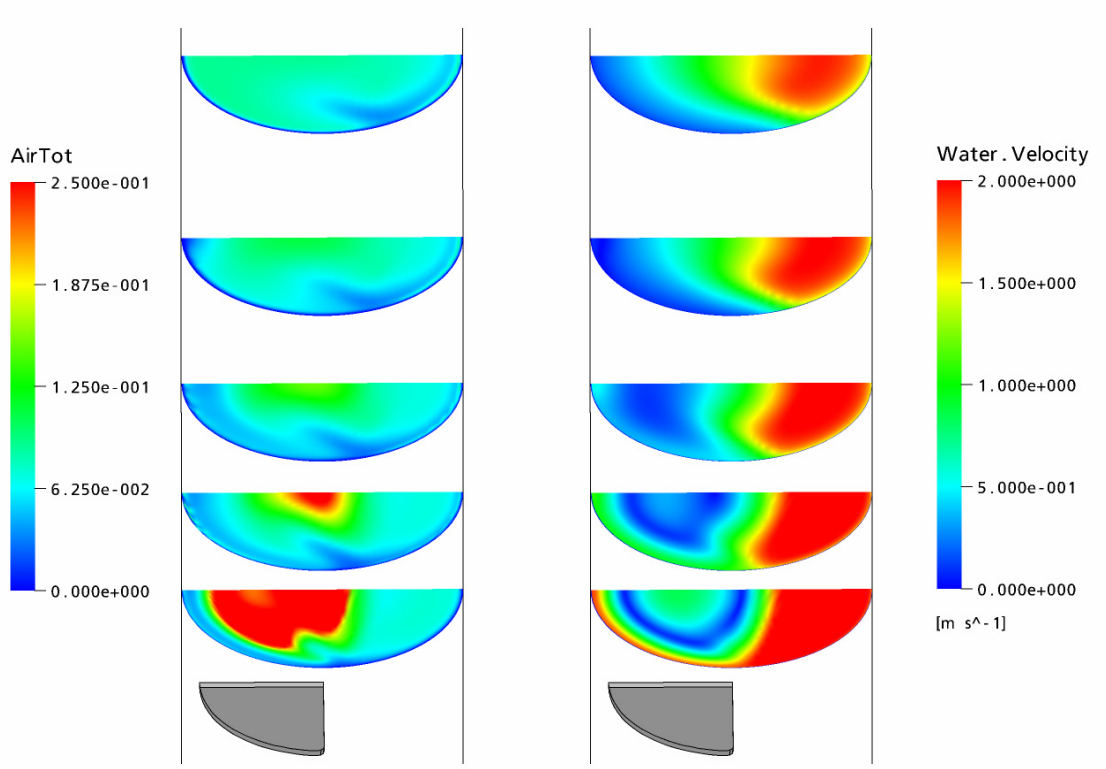

Fig. 7.13 Calculated integral gas volume fraction and water velocity distribution 0.08m, 0.16m, 0.25m, 0,37m and 0,52m downstream the obstacle (run 096)

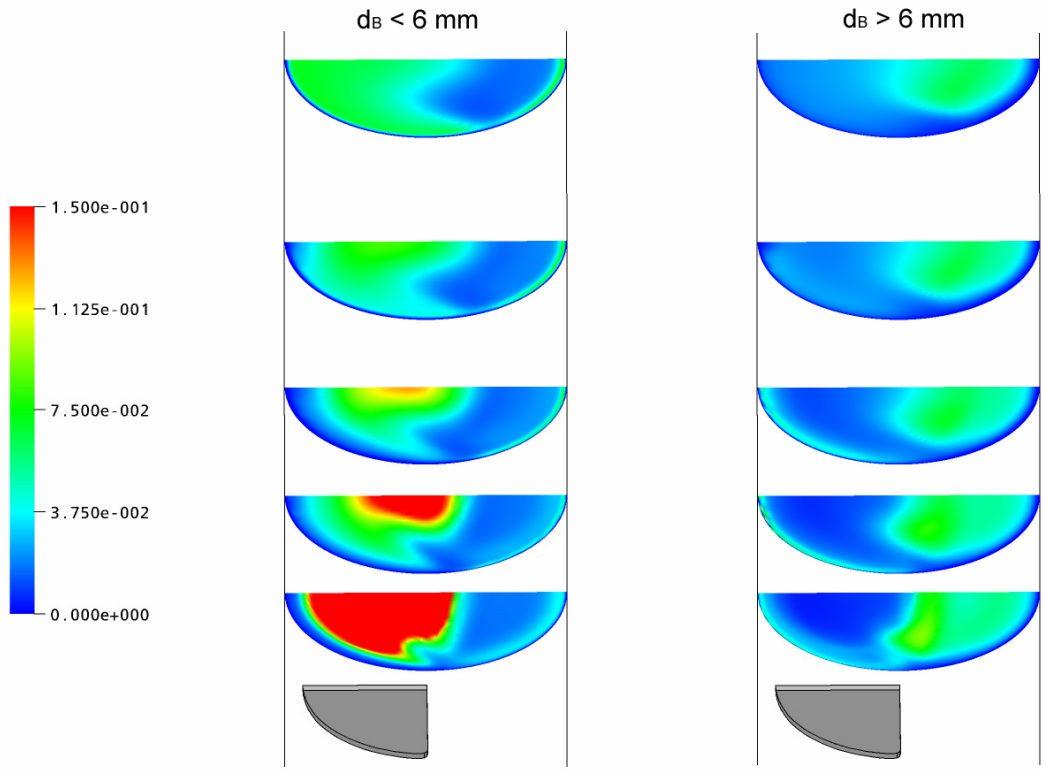

Fig. 7.14 Calculated gas volume fraction distributions for small and large bubbles (run 096)

The following interacting phenomena can be observed:

- transport of small bubbles in the wake behind the obstacle by the lift force
- bubble coalescence in the wake behind the obstacle caused by bubble accumulation in this region
- redirection of the created large bubbles into the jet downstream the obstacle
- bubble breakup downstream the obstacle caused by increased turbulent dissipation
- a separated stable region of very low gas fractions in the jet coming from the non-obstructed part of the cross-section.

Further work on this topic is under way.

8. Overview of the performed CFX validation calculations for the inhomogeneous MUSIG model

The following table summarizes the simulations done with CFX for validation of MUSIG model. The results of the simulations, which are not discussed in this report nor the Technical Report "Validation of the Multiple Velocity Multiple Size Group (CFX10.0 N x M MUSIG) Model for Poly-dispersed Multiphase Flows" showed the same tendencies as the represented ones.

Test	N	M	d_{bmax}	F_B	F_C	Remarks
MTLoop –tests Air/Water						
107	2	-		0	0	Test on number of required velocity goups – no bubble coalescence and breakup considered *
	4					
118	2					
	3					
	4					
107	2	34	17.0	1	0.05	
	2	24	12.0	1	0.1	
				0.25	0.5	
				0.25	0.05	
	3	24	12.0	0.25	0.05	
	4	24	12.0	1	0.1	
				0.25	0.05	
118	2	34	17.0	1	0.05	*
				1	0.5	*
				0.05	0.5	*
				0.25	0.5	
				0.25	0.05	Reference test
	3	34	17.0	1	0.05	
				0.25	0.05	*
	4	34	17.0	1	0.05	
				0.25	0.05	*
TOPFLOW-tests Air/Water						
074	2	21	13.0	0.5	0.01	** further investigation of different drag models and dispersion coefficients
107	2	21	44.0	1.0	0.01	**
107	2	21	44.0	0.05	0.01	**
107	2	21	44.0	0.25	0.01	**
118	2	20	60.0	0.25	0.05	*
Steam/Water at 6.5 MPa						
107	2	25	25.0	0.25	0.05	only 1000 iterations
107	2	17	25.5	0.25	0.05	*
107	2	25	25.0	0.025	0.05	*
118	2	25	37.5	0.025	0.05	*

Test	N	M	d_{bmax}	F_B	F_C	Remarks
Flow around obstacle						
074	2	25	25.0	0.25	0.2	*
074				0.25	1.0	
074				0.25	0.6	only 2000 iterations
074				0.1	0.6	*
074				0.1	0.2	*
074				0.0	0.05	*
074	3	20	20.0	0.0	0.05	
096	2	25	25.0	0.0	0.05	*
096	2	25		0.1	0.2	
096	2	25		0.05	0.05	*
097	2	20		0.05	0.05	*
118	2	25	25.0	0.0	0.05	
118	2	20	40.0	0.0	0.05	*
118	2	20	40.0	0.1	0.05	

* The results are presented in the actual report.
** These simulations are presented in the Technical Report “Validation of the Multiple Velocity Multiple Size Group (CFX10.0 N x M MUSIG) Model for Poly-dispersed Multiphase Flows”.

9. Summary and conclusions

For the simulation of a two phase gas liquid flow situation with higher gas content the bubble size distribution has to be modeled since the gas liquid momentum exchange is influenced by the bubble size. The importance of the lateral separation of small and large bubbles for the correct description of the flow pattern could be shown in chapter 2.3 for a developing flow in a vertical tube. Population balance models for the simulation of bubble fragmentation respective bubble coalescence require decades of bubble size classes. The separation of small and large bubbles is caused by a changing sign of the lift force in a quite narrow bubble size region.

To find a compromise between numerical stability and adequate model description the inhomogenous multiple size group approach was developed (see chapter 4) and implemented in the CFD code CFX. The decades of bubble size classes necessary for the adequate simulation of breakup and coalescence are considered only in the momentum equation as fractions of the dispersed gaseous phase. These gas fractions are assigned to only few velocity groups considered in the momentum equation.

This concept has to be proven very powerful describing flow situations with higher gas content. Validation calculations for air water flow are presented in chapter 6.2. In chapter 6.3 the case of steam water flow at saturation conditions is investigated. In chapter 7 the application of the model to a real 3D flow situation – the flow around a half moon shaped obstacle – is presented.

All investigation reveals the models for breakup and coalescence as the weakest point of the model framework. Adjusting these models to the measured values the qualitative flow behaviour can be described very well. So the core peak of the cross sectional gas volume fraction distribution is clear seen for vertical upward two phase flow with higher gas content. In the case of the obstacle the accumulation of small bubbles downstream the diaphragm is simulated very well. Unfortunately no unique set of model constants for the breakup and coalescence models could be found valid for all presented application cases. Never the less the adjusted model constants were valid for the whole flow situation. So all air/water tests both at MTLoop and at TOPFLOW could be simulated with the same constants. These constants overestimate bubble fragmentation at steam water flow. Also in the complex flow situation bubble fragmentation was overestimated applying this parameter set.

For the further model development the activities should be directed on the improvement of the models for bubble breakup and bubble coalescence. These models usually depend on the turbulence parameters of the flow. Therefore also the correct simulation of these parameters and their influence by bubbly flow should be critical reviewed.

10. References

Antal, S.P., Lahey, R.T., Flaherty, J.E. (1991). Analysis of phase distribution in fully developed laminar bubbly two-phase flow, Int. J. Multiphase Flow, Vol. 17, pp. 635-652.

Bhaga, D., Weber, M.E. (1981). Bubbles in viscous liquids: shapes, wakes and velocities, J. of Fluid Mechanics, vol. 105, pp. 61-85.

Burns, A.D., Frank, T., Hamill, I., Shi, J.-M. (2004). The favre averaged drag model for turbulence dispersion in Eulerian multi-phase flows, 5th Int. Conf. on Multiphase Flow, ICMF'2004, Yokohama, Japan.

Carrica, P.M., Drew, D.A., Lahey, R.T. (1999). A polydisperse model for bubbly two-phase flow around a surface ship, Int.l J. of Multiphase Flow, vol. 25, pp. 257-305.

Drew, D.A. (2001). A turbulent dispersion model for particles or bubbles, J. of Engineering Mathematics, vol. 41, pp. 259-274.

Ervin, E.A., Tryggvason, G. (1997). The rise of bubbles in a vertical shear flow, J.l of Fluids Engineering, vol. 119, pp. 443-449.

Frank, T., Zwart, P.J., Shi, J.-M., Krepper, E., Rohde, U. (2005). Inhomogeneous MUSIG Model – a Population Balance Approach for Polydispersed Bubbly Flows, International Conference “Nuclear Energy for New Europe 2005”, Bled, Slovenia, September 5-8, 2005.

Frank, Th., Zwart, P.J., Krepper, E., Prasser, H.-M., Lucas, D., (2006). Validation of CFD models for mono- and polydisperse air-water two-phase flows in pipes, OECD/NEA International Workshop on The Benchmarking of CFD Codes for Application to Nuclear Reactor Safety (CFD4NRS), 05.-09.09.2006, Garching, Deutschland, OECD/NEA, 05.-09.09.2006, Garching, Germany.

Frank, Th., (2006). Entwicklung von CFD Software zur Simulation mehrdimensionaler Strömungen im Reaktorkühlsystem, Abschlußbericht zum Vorhaben 150 1271, ANSYS/TR-06-01, 29.01.2006.

Gosman, A.D., Lekakou, C. Politis, S.R. Issa, I. Looney, M.K. (1992). Multi-dimensional modeling of turbulent two-phase flow in stirred vessels, AIChE Journal, vol. 38, pp. 1946-1956.

Grace, J.R., Wairegi, T. and Niguyen, T.H. (1976). Shapes and velocities of simple drops and bubbles moving freely through immiscible liquids, Trans. Inst. Chem. Eng., vol. 54, pp. 167.

Hosokawa, S., Tomiyama, A., Misaki, S., Hamada, T. (2002). Lateral migration of single bubbles due to the presence of wall, Proceedings of ASME Fluids Engineering Division Summer Meeting, Montreal, Ouebec, Canada.

Hughmark, G.A. (1967). Mass and heat transfer from a rigid sphere. AIChE Journal, vol. 13, pp. 1219-1221.

Krepper, E.; Lucas, D.; Prasser, H.-M. (2005). On the modelling of bubbly flow in vertical pipes, Nuclear Engineering and Design, vol. 235, pp. 597-611.

Lahey, R.T., Lopez de Bertodano, M. Jones, O.C. (1993). Phase distribution in complex geometry conduits, Nuclear Engineering and Design, vol. 141, pp. 177-201.

Lo S. (1996). Application of the MUSIG model to bubbly flows, AEAT-1096, AEA Technology, June 1996.

Lo, S. (2000a). Application of population balance to CFD modelling of gas-liquid reactors, Proceedings of the conference on "Trends in numerical and physical modelling of Industrial Flows", Corse, September 27-29.

Lo, S. (2000b). Recent Advances In CFD For Industrial Multiphase Flows, Invited lecture, NAFEMS Awareness Seminar, "Industrial CFD and the Move Towards Multiphase Flow Simulations", 8. Nov 2000, University of Warwick, UK.

Lopez de Bertodano, M. (1998). Two fluid model for two-phase turbulent jets, Nuclear Engineering and Design, vol. 179, pp. 65-74.

Lucas, D., Krepper, E., Prasser, H.-M. (2001a). Prediction of radial gas profiles in vertical pipe flow on basis of the bubble size distribution, International J. of Thermal Sciences, vol. 40, pp. 217-225.

Lucas, D., Krepper, E. and Prasser, H.-M. (2001b). Development of bubble size distributions in vertical pipe flow by consideration of radial gas fraction profiles. 4th International Conference on Multiphase Flow, New Orleans, Paper 378.

Lucas, D., Prasser, H.-M. (2004). Scaling Effects in Vertical Bubbly Pipe Flow. 5th Int. Conf. on Multiphase Flow, ICMF'2004, Yokohama, Japan.

Lucas, D., Shi, J.-M., Krepper, E. and Prasser, H.-M. (2004). Models for the forces acting on bubbles in comparison with experimental data for vertical pipe flow. 3rd International Symposium on Two-Phase Flow Modelling and Experimentation, Pisa, Italy, Paper ha04.

Lucas , D. Krepper, E., Prasser, H.-M., (2005a). Development of co-current air–water flow in a vertical pipe, International Journal of Multiphase Flow, vol. 31 pp. 1304–1328

Lucas, D., Krepper, E., Prasser, H.-M., (2005b). Modelling of the evolution of bubbly flow along a large vertical pipe, The 11th International Topical Meeting on Nuclear Reactor Thermal-Hydraulics (NURETH-11) Avignon, France, October 2-6, 2005, Paper: 051

Lucas, D., Prasser, H.-M., Manera, A. (2005c). Influence of the lift force on the stability of a bubble column, Chemical Engineering Science, vol. 60, pp. 3609-3619.

Lucas, D., Krepper, E., Prasser, H.-M. Manera, A. (2006). Investigations on the stability of the flow characteristics in a bubble column, Chemical Engineering Technology, vol. 29, pp. 1066-1072.

Lucas, D., Prasser, H.-M., (2007a). Steam bubble condensation in sub-cooled water in case of co-current vertical pipe flow, Nuclear Engineering and Design, vol. 237, pp. 497-508.

Lucas, D., Krepper, E., Prasser, H.-M., (2007b). Modelling of the evolution of bubbly flow along a large vertical pipe, Nuclear Technology (May 2007)

Luo, H. and Svendsen, H.F. (1996). Theoretical model for drop and bubble breakup in turbulent flows, AIChEJ, vol. 42, pp. 1225-1233.

Menter F. (1994). Two-equation eddy-viscosity turbulence models for engineering applications, AIAA-Journal, vol. 32, 8.

Menter, F. (2002). CFD Best Practice Guidelines for CFD Code Validation for Reactor Safety Applications. ECORA FIKS-CT-2001-00154.

Moraga, F.J., Larreteguy, A.E., Drew, D.A., Lahey, R.T. (2003). Assessment of turbulent dispersion models for bubbly flows in the low Stokes number limit, Int. J. of Multiphase Flow, vol. 29, pp. 655-673.

Ohnuki, A. and Akimoto, H. (2000). Experimental study on transition of flow pattern and phase distribution in upward air-water two-phase flow along a large vertical pipe, Int. J. of Multiphase Flow, vol. 26, pp. 367-386.

Prasser, H.-M., Böttger, A., Zschau, J. (1998). A new electrode-mesh tomograph for gas-liquid flows, Flow Measurement and Instrumentation, vol. 9, pp. 111-119.

Prasser, H.-M., Scholz, D., Zippe, C. (2001). Bubble size measurement using wire-mesh sensors, Flow Measurement and Instrumentation, vol. 12 pp. 299-312.

Prasser, H.-M., Krepper, E., Lucas, D., (2002). Evolution of the two-phase flow in a vertical tube - de-composition of gas fraction profiles according to bubble size classes using wire-mesh sensors, International Journal of Thermal Sciences, vol. 41, pp. 17-28.

Prasser, H.-M., Lucas, D., Krepper, E., Baldauf, D., Böttger, A., Rohde, U., Schütz, P., Weiss, F.-P., Zippe, C., Zippe, W. Zschau, J. (2003a). Strömungskarten und Modelle für transiente Zweiphasenströmungen, Abschlussbericht zum BMWA-Projekt 150 1215, FZR-379.

Prasser, H.-M.; Beyer, M.; Böttger, A.; Carl, H.; Lucas, D.; Schaffrath, A.; Schütz, P.; Weiß, F.-P.; Zschau, J. (2003b). Influence of the pipe diameter on the structure of the gas-liquid interface in a vertical two-phase pipe flow, The 10th International Topical Meeting on Nuclear Reactor Thermal Hydraulics (NURETH-10), Seoul, Korea, October 5-9, Paper: A00308.

Prasser, H.-M., Th. Frank, M. Beyer, H. Carl, S. Al-Issa, H. Pietruske, and P. Schütz, (2005). Gas-liquid flow around an obstacle in a vertical pipe -experiment and computational fluid dynamics simulation, Forschungszentrum Rossendorf Institute of Safety Research, Annual Report 2005.

Prince, M.J. and Blanch, H.W., (1990). Bubble coalescence and break-up in air-sparged bubble columns, AIChEJ, vol. 36, pp. 1485-1499.

Sato, Y. and Sekoguchi, K. (1975). Liquid velocity distribution in two phase bubble flow. Int. J. Multiphase Flow, vol. 2, pp. 79-95.

Sato, Y., Sadatomi, M., Sekoguchi, K. (1981). Momentum and heat transfer in two-phase bubble flow-I, Int. J. of Multiphase Flow, vol. 7, pp. 167-177.

Schiller, L. and Nauman, A., (1933). VDI Zeitschrift, vol. 77 p 318.

Shi, J.-M., Frank, T., Krepper, E., Lucas, D., Rohde, U., Prasser, H.-M., (2004a). Implementation and validation of non-drag interfacial forces in CFX-5.6. 5th Int. Conf. on Multiphase Flow, ICMF'2004, Yokohama, Japan, Paper No. 400.

Shi, J.-M., Krepper, E., Lucas, D., Rohde, U. (2003). Some concepts for improving the MUSIG model, FZ-Rossendorf, internal note.

Shi, J.-M., Frank, T., Prasser, H.-M. and Rohde, U. (2004). N * 1 MUSIG model – implementation and application to gas-liquid flows in a vertical pipe. In ANSYS CFX &ICEM CFD Conference 2004, Dresden, 10.-12. November.

Shi, J.-M., Zwart, P.-J., Frank, T., Rohde U. and Prasser, H.-M. (2004). Development of a multiple velocity multiple size group model for poly-dispersed multiphase flows. In Annual Report of Institute of Safety Research. Forschungszentrum Rossendorf, Germany, 2004.

Shi, J.-M., Rohde, U., Prasser, H.-M. (2005). The Multiple Velocity Multiple Size Group (CFX10.0 N *M MUSIG) Model for Poly-dispersed Multiphase Flows, - Validation report, FZ-Rossendorf internal note.

Tomiyama, A. Sou, I. Zun, I. Kanami, N. Sakaguchi, T. (1995). Effects of Eötvös number and dimensionless liquid volumetric flux on lateral motion of a bubble in a laminar duct flow, Advances in Multiphase Flow, pp. 3-15.

Tomiyama, A. (1998). Struggle with computational bubble dynamics, in: Proceedings of Third International Conference on Multiphase Flow, ICMF 98, Lyon, France, June 8-12, 1998.

Wellek, R.M., Agrawal, A.K., Skelland, A.H.P., (1966). Shapes of liquid drops moving in liquid media, AIChE Journal, vol. 12, pp. 854-860.

Zun, I. (1980). The transverse migration of bubbles influenced by walls in vertical bubbly flow, Int. J. Multiphase Flow, vol. 6, pp. 583-588.

Zwart, P., A. Burns, A. and Montavon C.. (2003). Multiple size group models. Technical report, AEA Technology plc, Novermber, 2003. CFX-5.7.

11. Indexes

11.1 Nomenclature and abbreviations

Notation	Unit	Denomination
C_D	-	Drag coefficient
C_L	-	Lift coefficient
c_p	J K^{-1} kg^{-3}	Specific heat capacity for constant pressure
C_{TD}	-	Turbulent dispersion coefficient
C_{VM}	-	Virtual mass coefficient
C_W	-	Wall force coefficient
d_b	m	Volume equivalent bubble diameter
d_h	m	Horizontal bubble diameter
D	m	Pipe diameter
Eo	-	Eötvös Number
F_B	-	Breakup coefficient
F_C	-	Coalescence coefficient
F_D	N m^{-3}	Drag force
F_{deform}	N m^{-3}	Bubble deformation force
F_L	N m^{-3}	Lift force
F_{TD}	N m^{-3}	Turbulent dispersion force
F_{VM}	N m^{-3}	Virtual mass force
F_W	N m^{-3}	Wall force
g	m s^{-2}	Acceleration due to gravity
h	J kg^{-3}	Specific Enthalpy
J	m s^{-1}	Superficial velocity
k	m^2 s^{-2}	Turbulent kinetic energy
Mo	-	Morton Number
n	m^{-3}	Bubble number density
p	Pa	Pressure
Pr	-	Prandtl number
q	W m^{-2}	Wall heat flux
q^{phases}	W m^{-3}	Volume related heat flux to the interface
r	m	Radial coordinate
R	m	Pipe radius
Re	-	Bubble Reynolds number
Re_l	-	Reynolds number for liquid pipe flow
St	-	Stokes number
t	s	Time
T	K	Temperature

u	m/s	Radial bubble velocity
V	m^3	Volume
V_{term}	$m\ s^{-1}$	Terminal velocity
w	$m\ s^{-1}$	Velocity
y	m	Distance to the wall
Γ	$kg\ m^{-3}\ s^{-1}$	Mass transfer rate
$\Gamma_{i,j}$	$m^{-3}\ s^{-1}$	Coalescence rate
Ω	s^{-1}	Breakup frequency
α	-	Volume fraction
ε	$m^2\ s^{-3}$	Dissipation rate of the turbulent energy
μ	$kg\ m^{-1}\ s^{-1}$	Dynamic viscosity
ν	m^2/s	Kinematic viscosity
ρ	$kg\ m^{-3}$	Density
σ	$N\ m^{-1}$	Surface tension

Index	**Denomination**
av	average
b	bubble
G	gas
i, j	group index
k	radial node
L	liquid
rel	relative
s	saturation
t	turbulent

Notation	**Denomination**
CFD	Computational Fluid Dynamics
CFX	CFD software
DN	nominal diameter
FAD	Favre averaged drag
FZD	Forschungszentrum Dresden-Rossendorf
L/D	Length to diameter
LES	Large Eddy Simulation
MTLoop	Measurement Techniques Loop
MUSIG	Multiple Bubble Size Group Model (CFX)
RPV	Reactor Pressure Vessel
SST	Shear Stress Transport
TOPFLOW	Transient Two Phase Flow Test Facility

11.2 Figures

11.3 Tables